POLITECNICO DI MILANO

SCUOLA DI INGEGNERIA INDUSTRIALE E DELL'INFORMAZIONE

Corso di Laurea Specialistica in
Ingegneria Spaziale

Drag Augmentation Sails for Space Vehicle De-Orbit

Relatore: Prof. Michèle LAVAGNA

Tesi di Laurea di:
Alice BONFANTI 754770

Anno Accademico 2012 - 2013

Alle mie radici,
i miei nonni Ines e Pasquino.

Acknowledgements

This work represents the end of a long walk, not only academic but also of life. Many were the difficulties to face, but many more were the satisfactions that in these years I had the luck to live. I could find new extraordinary people with whom to share the journey, but also rediscover the importance of who, in turn, have been always by my side. To all of them I owe a huge thank you.

Firstly, I would like to thank Professor Lavagna for allowing me to develop this project and for guiding me during its realization.

This thesis was developed in collaboration with ESA TEC-ECN section. For giving me this unique opportunity and for his enthusiastic suggestions, I would like to thank Guillermo Ortega. A particular thank you goes to Antonio Rinalducci for always being able to give me all the necessary support, despite his busy schedule; always available and patient, I could not have asked for more. In addition, a thank you is owed also to the entire TEC-ECN section, especially Sven Erb for his help and stimulating discussions.

Un enorme grazie va alla mia famiglia, nessuno escluso, che mi ha sostenuto in tutte le mie scelte. In particolar modo ringrazio mia mamma e mio fratello, per aver sopportato i miei musi lunghi, per aver sdrammatizzato quando era necessario, e per avermi insegnato a non arrendermi mai. Senza di voi non avrei potuto raggiungere questo traguardo.

Devo inoltre ringraziare mio papà, che non mi ha mai abbandonata, dandomi la forza di andare avanti e superare ogni ostacolo. Sei stato e sarai sempre il mio punto di riferimento, un appoggio silenzioso su cui poter contare e un esempio da seguire.

Un ringraziamento va a tutti gli amici e compagni di università, da quelli incontrati il primo giorno a quelli con cui ho condiviso le fatiche degli ultimi esami. Avete reso indimenticabile questo viaggio.

Um enorme obrigado para a Ana, o Joaquim, o Pedro, o Rúben e o Valerio, com quem partilhei inesquecíveis momentos durante estes dois anos. Vocês ensinaram-me que a verdadeira amizade não conhece distância.

E por último mas não menos importante, quero agradecer ao Guilherme. Com a tua paciência e generosidade fizeste tudo isto possível. Obrigada por nunca parares de acreditar em mim e por nunca me deixares só nos momentos de dificuldade. Não bastaria uma página inteira para te mostrar quanto te estou grata. Só quero que saibas que estás em cada sorriso meu.

Contents

List of Figures

List of Tables

List of Acronyms

ADR	Active Debris Removal
AoA	Angle of Attack
AU	Astronomical Unit
AVUM	Attitude Vernier Upper Module
BoL	Begin of Life
CDR	Critical Design Review
CFRP	Carbon Fibre Reinforced Polymer
CoM	Centre of Mass
DoF	Degrees of Freedom
ECI	Earth Centred Inertial
ECSS	European Cooperation for Space Standardization
EoL	End of Life
ESA	European Space Agency
ESCM	Earth Shadow Conical Model
GBE	Generalized Beam Elements
IADC	Inter Agency Space Debris Coordination Committee
JAXA	Japanese Space Agency
LEO	Low Earth Orbit
MMOD	Micrometeorite and Orbital Debris
NGDC	National Geophysical Data Center
NOAA	National Oceanic and Atmospheric Administration
ODE	Ordinary Differential Equation
RAAN	Right Ascension of the Ascending Node
RMS	Root Mean Square
RTN	Radial Tangential Normal
SAL	Solar Activity Level
SFU	Solar Flux Unit
SRP	Solar Radiation Pressure
SSC	Surrey Space Centre
SSO	Sun Synchronous Orbit
UT	Universal Time
VERTA	Vega Research and Technology Accompaniment
VESPA	Vega Secondary Payload Adapter

Sommario

La crescita incontrollata del numero di debris presenti attorno alla Terra comporta numerosi rischi e necessita quindi di appropriate misure di contenimento. Una delle soluzioni più accreditate per prevenire un ulteriore aumento di debris in LEO è il deorbiting di satelliti a fine vita. Tra tutti i mezzi idonei a eseguire questa manovra, il decadimento assistito tramite vela, noto anche come drag-sail deorbiting, è uno dei più studiati. In questa tesi il potenziale delle drag-sails è ampiamente esaminato. Un modello di propagazione orbitale basato su atmosfera NRLMSISE-00 e campo di gravità non uniforme è usato per analizzare l'influenza dell'orbita iniziale sul processo di deorbiting. Questo fornisce, inoltre, informazioni riguardanti le variazioni della densità atmosferica dovute all'attività solare. Aumentando il livello di fedeltà delle analisi è stato implementato un modello a 6 gradi di libertà con superfici ad elementi discreti. Ciò permette di includere l'effetto di self-shielding e interbody-shielding tra satellite e vela, sia per simulazioni aerodinamiche che della pressione solare. Questi algoritmi, integrati nel propagatore orbitale, sono sfruttati per lo studio della stabilità passiva di diverse geometrie di vela. Parametri come la forma, dimensioni della vela e distanza dal satellite, sono testati individualmente per un miglior apprendimento della loro influenza sulle performance di deorbit. In seguito, le caratteristiche ottiche della vela sono esaminate a causa del loro forte impatto sul contributo solare durante la discesa. La correlazione tra la forza impressa dalla radiazione solare e la stabilità passiva del sistema di deorbiting è in seguito dimostrata. Come ulteriore prova del possibile sviluppo di tale sistema, il design di due casi reali è realizzato e supportato dal corrispondente mass budget. I risultati di questa tesi dimostrano le grandi potenzialità delle drag-sails, fornendo, inoltre, una panoramica dei principali aspetti critici correlati. Questo sistema rappresenta quindi un' ottima possibile soluzione al problema dei debris, assicurando un recupero considerevole di massa utile e un deorbiting passivo.

Abstract

The uncontrolled growth of orbital pollution and the threat that it poses to space operations, demand for appropriate mitigation measures. End-of-life deorbiting is the most considered solution to prevent additional debris generation in LEO. Among the several means of performing this manoeuvre, drag-sail assisted decay is one of the most studied. The low mass of deorbit sail systems makes them an extremely attractive technology. In this thesis the capabilities and properties of drag-sails are extensively investigated. An orbital propagation model using a NRLMSISE-00 atmosphere, zonal harmonics gravity and solar radiation pressure description, is developed; this is used to analyze the influence of initial orbit and solar cycle dependent atmosphere on the deorbiting process. Increasing the fidelity of the analysis, a 6 degrees-of-freedom discrete surface elements model of sail and spacecraft is built, including self-shielding and interbody-shielding effects for both aerodynamic and solar radiation pressure simulation. These algorithms, integrated in the orbital propagator, are employed to study the passive attitude stability properties of several sail geometries. Parameters such as sail shape, size and distance to the spacecraft (mast length) are individually tested to better understand its influence on the deorbit performance. Additionally, the sail optical characteristics are examined due to their strong impact on the solar force contribution. Furthermore, the correlation between the solar radiation pressure force and the passive stability of the deorbiting system is demonstrated. As further evidence of the drag-sail feasibility, two realistic test case solutions are designed and supported by the correspondent mass budget. The outcome of this thesis extensively demonstrates the capabilities of the designed deorbiting system, while providing a preliminary overview of the main critical aspects. Within this work drag-sail are shown to be a high potential solution for the space debris problem, allowing considerable mass saving and passive deorbiting.

1 Introduction

This chapter introduces the problems and risks related to space pollution. An overview of the current space debris population, future predictions and mitigation measures are provided. Finally, a trade-off between the most studied deorbiting techniques is performed.

1.1 The debris problem

Space debris is defined as "all man-made objects, including fragments and elements thereof, in Earth orbit or re-entering the atmosphere, that are non-functional" [**1**]. This description includes a wide range of orbital objects from spent rocket stages, old satellites, fragments from disintegration, erosion, and collisions, generated ever since the first days of spaceflight. It has been estimated by [**2**] that up to 60% of the debris currently in LEO consists in fragments from upper stages and spent boosters explosions occurred in the 1950s and 1960s. However, the list of debris includes also 60,000 droplets of leaked sodium coolant [**3**], the detachment of solar cells from the panels of spacecraft due to thermal stresses [**4**],rocket exhaust particulates [**5**],and accidentally lost objects such as the errant spacesuit glove [**6**].

The total amount of non-operational objects larger than 1 cm amounts to 95,000 debris objects and about 1010 object larger than 0.1 mm [**7**].

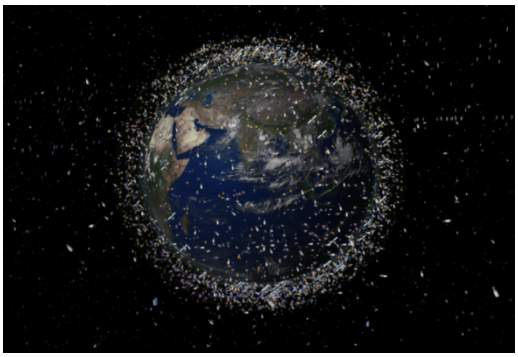

Figure 1.1: LEO debris representation

This number will unequivocally grow as more and more nations gain the technology to launch satellites into Earth orbit. However, recent studies suggest that the number of objects in orbit might grow, even when no further objects are added to space, due to collisions caused by fragments generated by other collisions [**8**].This collisional cascading may potentially lead to a chain reaction situation, with no further possibility of human intervention and with a substantial increase of the hazard level for space operations (Kessler syndrome).

Figure 1.2 [**8**] shows the catalogued population of man-made objects in space in the last 54 years. It can be noticed the high presence of fragmentation debris, compared to the number of spacecraft or rocket bodies.

Space debris' main dangerous effect is the possibility of violent collision with active spacecraft in LEO. Indeed, the energy content of a debris objects can have destructive consequences on the impacted satellite. In addition, there is also the risk of damage on the ground, if debris survives Earth's atmospheric re-entry.

In this catastrophic scenario, it is clear that mitigation measures are fundamental to control the debris growth, while active removal strategies are a necessary way to reduce the number of non-operational objects, preserving the outer space environment for future generations.

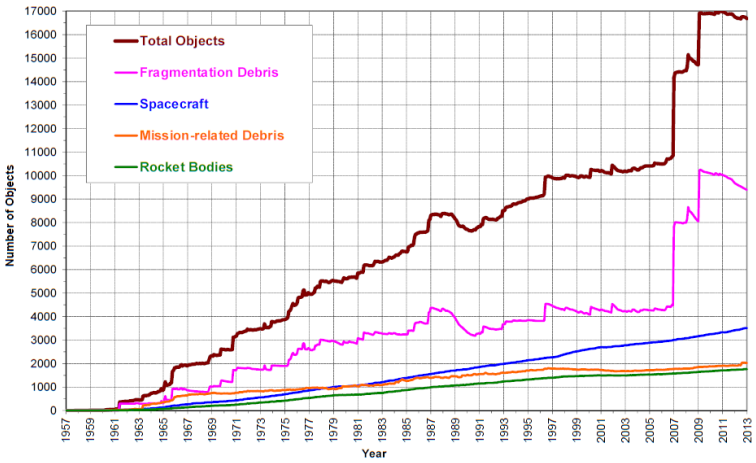

Figure 1.2: Catalogued manmade objects in space over the last 54 years [8]

1.2 Mitigation measures

A set of mitigation guidelines has been created by the Inter Agency Space Debris Coordination Committee (IADC), reflecting the fundamental mitigation elements of a series of existing practices, standards, codes and handbooks developed by a number of national and international organizations [**1**]. The guidelines relevant to LEO spacecraft and, therefore, to this study, are summarized in:

- Limit debris release during normal operations;
- Minimise the potential for break-ups during operational phases;
- Minimise potential for post-mission break-ups resulting from stored energy;
- Limit the long-term presence of spacecraft and launch vehicle orbital stages in the LEO region after the end of their mission: 25 years have been found to be a reasonable limit in which the object disposal has to be performed.

1.3 Active Debris Removal

Active Debris Removal (ADR) indicates the identification and removal of existing non-operative space objects by moving them into a disposal orbit. In general, the ADR possibilities consist in:

- Direct retrieval and deorbit;
- Manoeuvre to an orbit for which atmospheric drag will remove the structure within 25 years;
- Manoeuvre to one of a set of disposal regions in which the structures will not interfere with future space operations. Storage orbits (also known as "graveyard orbits") in these disposal regions maybe used to dispose of space systems at end of mission.

The choice from these options is highly related to the spacecraft orbit at EoL.

1.4 LEO disposal methods

This study is focus on a specific set of mitigation methods meant to prevent the debris increment in LEO by including onboard of spacecraft means of self-deorbit.

The most discussed strategies for EoL spacecraft disposal in LEO can be divided in three technologies: namely, tethers, thrusters, solar sails and drag enhancement. Table 1.1 presents the major requirements for these strategies.

Deorbit Approach	Active/ Passive	Requirements
Propulsion	Active	• Requires high total impulse (challenging for small satellites) • Requires active pointing/steering • Requires long-term propellant storage
Solar sail	Active	• Requires active pointing/steering • Susceptible to jamming • Susceptible to MMOD degradation
Electrodynamic or drag tether	Passive	• Large characteristic dimension • Deployment complexity • Susceptible to jamming/tangling • Inclination-limited (electrodynamic tethers)
Inflatable drag device	Passive	• Requires long term, leak-free storage of compressed gas • Altitude-limited • Susceptible to jamming • Susceptible to MMOD degradation/puncture
Mechanically-Deployed drag device	Passive	• Requires storage of mechanical energy • Altitude-limited • Susceptible to jamming • Susceptible to MMOD degradation

Table 1.1: Summary of deorbiting techniques for LEO satellites [9]

Mechanically-deployed drag sails (Figure 1.3) offer the benefits of small characteristic dimension, no attitude control requirements, and no pressurized gasses, instead using only their own stored mechanical energy for deployment. Moreover, these devices are considered the most mass-efficient method for the 25-year deorbit of a dense spacecraft orbiting at altitude below 900 km [**10**]. This strategy is based on the deployment from the satellite of a structure (inflatable balloon, sail, etc.) capable to increase the drag effect, causing a velocity and loss and a consequent deorbit. In particular, this research studies the capabilities and the design aspects of a drag sail deorbiting system.

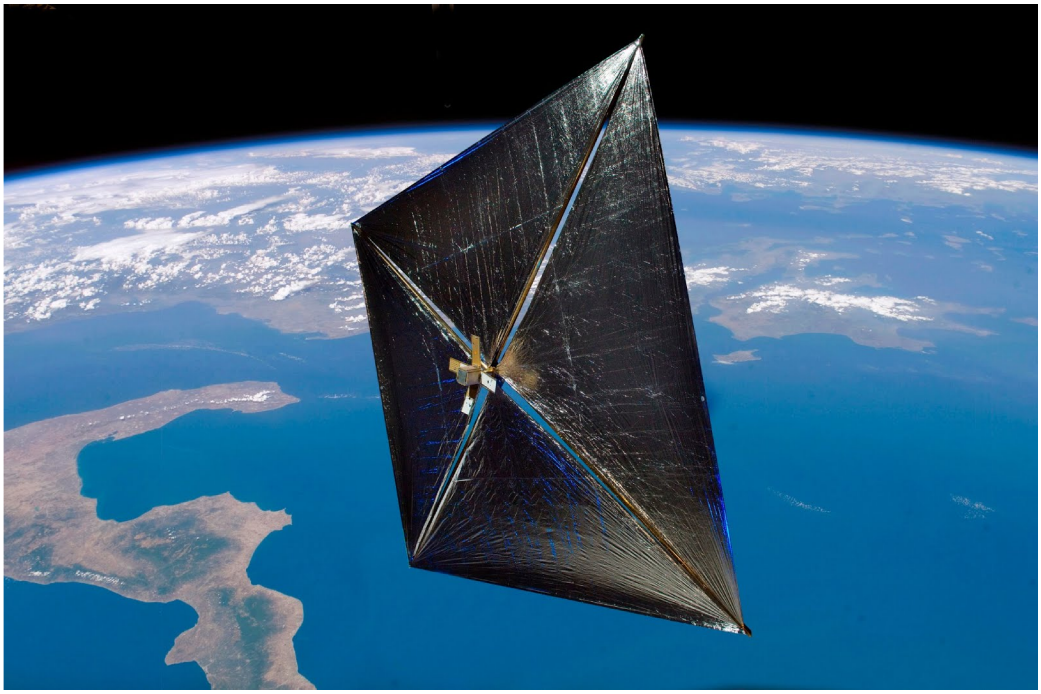

Figure 1.3: Deployed drag-enhancement device during deorbit phase [11**]**

2 Background

The drag sail deorbiting device has been studied for its promising characteristics in debris removal field. Due to the evident similarities with solar sails, the knowledge gained on this topic with years of researches has been exploited during the drag enhancement strategies study and design.

2.1 History

The very first concept of solar sail was developed in 1973 by Jet Propulsion Laboratory (JPL) and it was followed by several other mission proposals that, however, were never actuated or failed (i.e. Cosmos-1, NanoSail-D1). Finally, in 2010, the Japanese Space Agency (JAXA) launched the first solar sail mission, IKAROS, to Venus, demonstrating the power of the Sun for in-space propulsion. The December of the same year NanoSail-D2,a 3x3 m four quadrant sail, proving the deployment of the device which used Sun and drag effect to deorbit. LighSail-1 was designed as a modified version of NanoSail-D2 and it has successfully passed its CDR [**12**]. Surrey Space Center is currently working on three projects meant to demonstrate the feasibility of drag augmentation devices: Cubesail, DeorbitSail, Inflatesail. In addition, funded by ESA, a commercial device version for spacecraft as a "bolt on" system [**13**] called Gossamer Deorbited, is being developed. The aforementioned missions and several other studies provide a solid background for the subject of this thesis. The collected design information is hereafter exposed to clarify the standard components of a drag deorbiting device.

2.2 Drag augmentation device

A drag enhancement device is conceived to be deployed from the host satellite at its EoL. The main constituent of this strategy comprise:

- Drag sail
- Booms
- Mast

2.2.1 Drag sail

The drag sail is the main body of the deorbiting device and it is the means which increase the aerodynamic surface of the carrying satellite. A typical drag sail for satellite deorbit is a thin membrane which can be deployed in several configurations such as pyramid, cone, flat square, flat circular surface, etc. Its material has to provide a considerable increment of area but keeping the mass growth as low as possible, therefore superlight material such as Kapton of Mylar [**14**] are typically used. Moreover, the selected material needs to shows high physical properties over a wide temperature range to be able to survive in a harsh environment. For particular scenarios discussed later in this document, the drag sail may need to be transparent and in these cases a CP-1 polymide film could be preferred. In case of solar sail, the membrane is usually coated with a higly reflective layer to take advantage of the solar radiation pressure. The presence of micrometeorites and

small debris particles in LEO may lead to the selection of a thicker sail membrane and its structure can be reinforced with a net pattern so as to minimize tear.

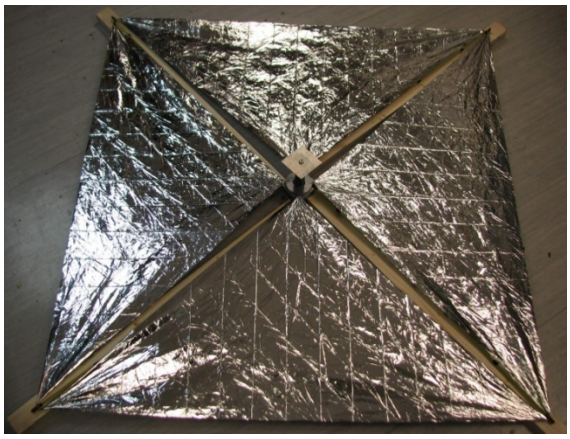

Figure 2.1: CubeSail deployed [13**]**

The density of both Kapton and Mylar is around 1400 kg/m^3 and both have a yeld stress of 1.7x10^8 Pa, although Mylar is slightly stiffer with a Young's modulus of 3.8 GPa against 3 GPa of Kapton [**15**]. CP-1 provides a lower elastic modulus of 2 GPa for a density of 1530 kg/m3. However, it is capable of transparency proprieties superior to the Kapton and Mylar one [**16**].

2.2.2 Booms

The drag sail must be deployed from its storage volume using an underlying deployable structure, and maintained in a semi-rigid and aerodynamically stable shape until the beginning of final re-entry. The simplest structure which can achieve this aim is a series of evenlyspaced booms radiating outward from the deorbit device hub, which assures the drag sail adopts an aerostable shuttlecock-like shape [**15**]. The optimum number of booms is discussed in Section 5.2.3 but the most common configuration is with four of them.

The radial booms must deploy reliably after a long hibernation period endured during the active life of the satellite host. The standard mechanisms by which this deployment may be performed are:

- **Deployment by gas inflation**: the booms could be deployed by gas inflation, the gas being released from a tank or generated as required from a chemical reaction or subliming powder. The use of this technique for the deorbit device structure is very problematic because of the high probability of puncture by micrometeorites or debris particles. Moreover, the means to achieve the inflation needs to be carried in the deorbiting device, decreasing the lightweight peculiarity of the strategy.
- **Deployment by transverse deflection:** the deployment of the sail from a stowed state could be performed using the stored strain energy of the transversely deflected radial booms, eliminating the issue regarding the

extra on-board energy source. As the drag sail is fixed to the stowed booms, the booms and sail membrane must be folded away by means of a common pattern which, however, results hard to design.

- **Deployment by telescopic extension:** telescopic extension means that the booms extend along their longitudinal axis when deployed. This method has been found to ensure reliable deployment without fouling or stalling. Furthermore, this system does not require careful management in order to avoid excessively violent.

The telescopic extension strategy has been considered the most adapt solution and some existing designs are here outlined:

- Tensegrity structures and collapsible trusses;
- STEMs and their derivatives (Bi-STEMs, CTMs etc.);
- Telescopic Masts;
- Coilable Masts;
- Open-section CFRP bistable booms.

The booms must be capable of highly compact stowage, while being able to carry the expected operational loads (sail deployment, sail tensioning and aerodynamic drag) despite their extreme slenderness. In order to meet these demanding and conflicting requirements, the open-section CFRP bistable booms solution has been selected for the design of this thesis. This concept has been extensively studied and developed by Surrey Space Center within the Gossamer [**14**] and CubeSail [**13**] projects.

Figure 2.2: Open-section CFRP bistable boom [13] and co-attachment to spindle [14]

The manufactured CFRP booms are composed by dry carbon fibers in a biaxial braid sleeve and unidirectional form, impregnated with a space qualified epoxy resin film. Each boom has a nominal thickness of 0.24 mm and a mass per unit length of 15g/m [**14**].

The selection of the deployment mechanism is driven by the assumed booms design. Relying once again on the Surrey Space Centre work, in the adopted deployment mechanism the booms are co-coiled around a central hub for storage, and during the deployment they are guided through two exit rollers. The deployment is

controlled by a motor placed inside the sail spindle which pushes the booms out from the deployer.

Figure 2.3: The CFRP boom deployment mechanism (left) and a detail of the coiled booms [14]

2.2.3 Telescopic mast

As it will be extensively discussed later in this document, a shuttlecock-like configuration of the deorbit device is of fundamental importance for the passive stability of the system. To enhance this characteristic the presence a mast between the host satellite and the sail can increase the stability margin, assuring a center of pressure of the deorbit system placed behind the center of mass. In addition, a spacer helps to avoid sail damages during its deployment due to accidental collision with satellite's instruments and appendixes. However, this could leads to flexibility problems of the mast which have to be taken in consideration when selecting the structure geometry and its material. Furthermore, the sail deployment mechanism will then results in a distant position respect to the satellite and this would requires an additional accurate analysis which is not performed within this thesis. Not many examples of this application have been found in literature but SSC included in the Gossamer project an extendable mast. It consists in a series of telescopic boxes, with the sail deployment system stored in the inner box. Compression springs are used as actuators, and rails permit low-friction linear sliding between the telescopic boxes (Figure 2.4).

The Gossamer Deorbiter uses a three-box solution, obtaining a mast length of 0.6 m. This value can be increased adding more telescopic stages, but the resulting structure will have a higher failure probability and possible flexibility issues.

However, the design of such a structure would require strict constraints, available only in later stages of a project. Indeed, the modification of the sail size, which will be a degree of freedom in this study, should be followed by the complete sizing of the telescopic mast, but due to the high concept level of this thesis, it has been decided to assume generic and fixed telescopic mast section dimensions, while having the possibility to tune its length.

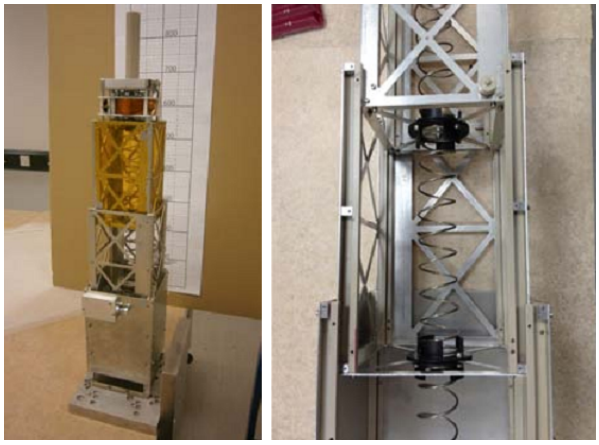

Figure 2.4: The telescopic deployment system designed by SSC and a detail of the compression springs used as actuators [14]

2.3 Study baseline

The aforementioned drag augmentation device components serve as baseline for the analysis work performed throughout this thesis. This baseline is here described.

2.3.1 Device

The chosen sail material is CP-1 because of its superior transparence proprieties. In this way, with the usage of coatings, it is possible to analyze the behavior of the system with very different optical characteristics. The booms instead are derived from the Surrey Space Centre concept, using open-section CFRP bistable booms coiled around a deployment mechanism. For what concerned the telescopic mast, as already anticipated, it has been assumed a design similar to the SSC one, but with slightly adapted dimensions which have been considered a feasible initial design set. Due to lack of information about the material used to manufacture the main structure for the mast, it is here assumed of aluminum since this is one of the most commonly used structure materials in space applications.

Moreover, within this design no attitude actuator has been considered. This choice is justified by the post end-of-life usage of the drag augmentation devices. After completion of its mission, it cannot be here assumed that most spacecraft will present sufficient level of reliability to perform a fully controlled deorbit manoeuvre for up to an additional 25 years.

2.3.2 Altitude

Due to the need of atmosphere to have acceptable performances with a drag device, the altitudes where the air density is too low cannot be taken in consideration. This limit corresponds to approximately 900 km [**10**]. For these reasons, orbit above 900 km have not been included in this study.

2.4 Reference frames

Due to the complexity of the system, several reference frames have been used.

Earth Centred Inertial – ECI

In the ECI coordinate system the Z axis runs along the Earth's rotational axis pointing North, the X axis points in the direction of the vernal equinox, and the Y axis completes the right-handed orthogonal system. The vernal equinox is an imaginary point in space which lies along the line representing the intersection of the Earth's equatorial plane and the plane of the Earth's orbit around the Sun or the ecliptic. The X axis, therefore, lies in both the equatorial plane and the ecliptic. These three axes defining the Earth-Centred Inertial coordinate system are 'fixed' in space and do not rotate with the Earth. Since in this frame of reference there are no fictitious forces the angular quantities and accelerations measured with respect to it are called absolute quantities. This frame served as inertial reference system.

Radial Tangential Normal – RTN

The Radial Tangential Normal reference frame is centred in the centre of mass of the orbiting system and its axis are defined as follow: the first axis points to the centre of the Earth, the second is tangential to the orbit and the third one is normal to the orbital place, forming a right-handed frame. This reference frame is used to allow an easier understanding of the attitude of the system respect to its position on the orbit.

Body Frames

The body frame is centred to the centre of mass of the object it refers to and it is fixed to it. Its axes are oriented along the directions of symmetry axes and eventually of also principal axes of inertia. The body frame is used for the definition of the geometrical and inertial proprieties of the body itself and to the express attitude of the system and the relative orientation between system components.

To simplify the characterization of the single object configuration, three different body frames were defined:

System Body Frame – B

Refers to the overall deorbit system.

Satellite Body Frame – B1

Refers to the host satellite body (Figure 2.5).

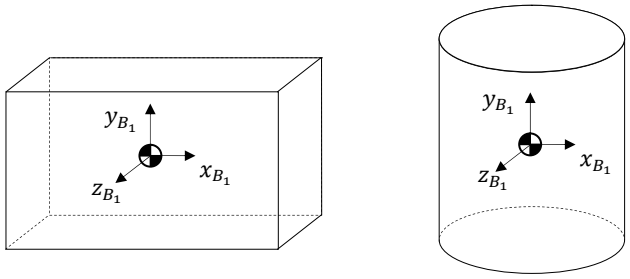

Figure 2.5: Satellite body frame B1

Sail Body Frame – B2

Refers to the drag sail body (Figure 2.6).

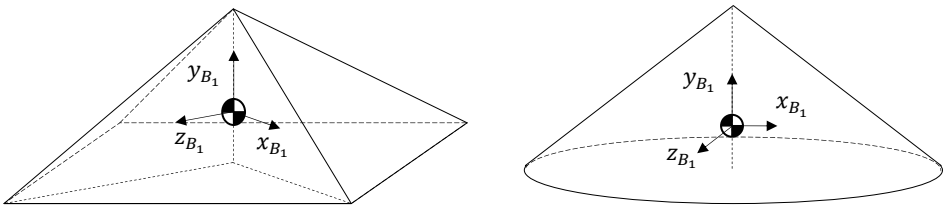

Figure 2.6: Sail body frame B2

2.5 Orbital elements

This section presents a brief outline of the Keplerian parameters used to describe a generic orbit [**17**].

- a is the *semimajor axis*, defined as half of the major axis of the conic.

$$a = \frac{r_a + r_p}{2} \tag{2.1}$$

- where r_a and r_p are the apoapsis and periapsis radius respectively.
- e is the *eccentricity* and it indicates the orbit's shape. It's defined as the ratio of the half the distance between the foci and the semimajor axis. It can also be easily expressed in function of the apoapsis and periapsis radius.

$$e = \frac{r_a - r_p}{r_a + r_p} \tag{2.2}$$

- i is the *inclination* of the orbit plane measured from the unit vector $\hat{\underline{Z}}$ to the angular momentum $\hat{\underline{h}}$.

$$\cos(i) = \frac{\hat{\underline{Z}} \cdot \hat{\underline{h}}}{\left|\hat{\underline{Z}}\right| \cdot \left|\hat{\underline{h}}\right|} \tag{2.3}$$

- Ω is the *right ascension of the ascending node (RAAN)* and is defined as the angle in the equatorial plane measured positively from the $\hat{\underline{I}}$ unit vector to the location of the ascending node.

$$\cos(\Omega) = \frac{\hat{\underline{X}} \cdot \hat{\underline{n}}}{\left|\hat{\underline{X}}\right| \cdot \left|\hat{\underline{n}}\right|} \tag{2.4}$$

where $\hat{\underline{n}}$ is the unit vector associated with the ascending node.

- ω is the *argument of perigee* which is the angle measured from the ascending node to the periapsis.

$$\cos(\omega) = \frac{\hat{\underline{n}} \cdot \hat{\underline{e}}}{\left|\hat{\underline{n}}\right| \cdot \left|\hat{\underline{e}}\right|} \tag{2.5}$$

where $\hat{\underline{e}}$ is the eccentricity unit vector.

- ν is the *true anomaly* which is the angular displacement measured from periapsis to the position vector $\underline{r}$ along the direction of motion.

$$\cos(\nu) = \frac{\hat{\underline{e}} \cdot \hat{\underline{r}}}{\left|\hat{\underline{e}}\right| \cdot \left|\hat{\underline{r}}\right|} \tag{2.6}$$

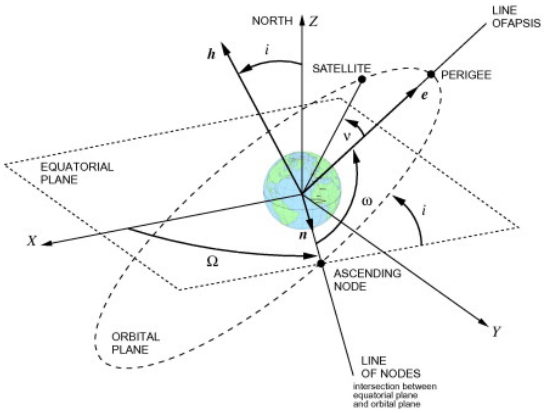

Figure 2.7: Classical orbital elements [18**]**

3 LEO Environment

This chapter describes the disturbances that most influence objects orbiting in LEO. The respective models are here reported and the effect of each perturbation is explained. This section contains the fundamentals that have been used for the computation of external forces acting on a LEO system.

3.1 Overview

On LEO orbits the most significant perturbations are:

- Earth gravity;
- Gravity zonal harmonics;
- Lunar gravity;
- Solar gravity;
- Solar radiation pressure;
- Aerodynamic drag.

The magnitude of these effects is shown against the altitude in Figure 3.1.

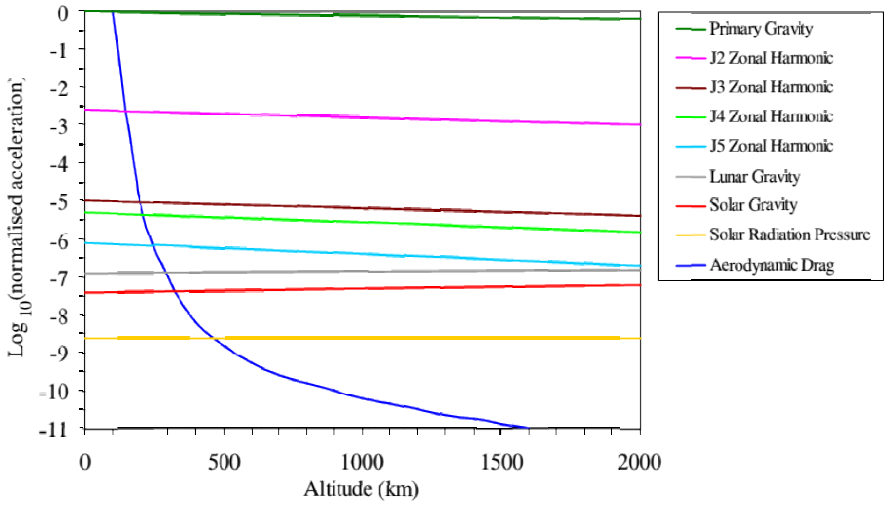

Figure 3.1: LEO perturbations comparison

From those reported on Figure 3.1, Solar and Lunar gravity were not treated in the research here presented because, although their magnitude is considerable the effect is, in fact, neglectable for lifetime analysis in LEO [**19**]. Indeed, also ISO 27852:2010(E) [**20**] does not consider the effects of these perturbations for orbital propagations below 2000 km altitude.

3.2 Gravity

3.2.1 Earth gravity model

Because the force exerted by the Earth on an object outside its sphere is conservative, it can be derived from a gradient of a scalar potential function $U(r)$ [**21**].

$$U(r) = -\frac{\mu}{r} \tag{3.1}$$

However, this is not entirely true since the Earth is an oblate body with non-homogeneous mass distribution., therefore its potential needs to include some correction factors.

For convenience, the Earth potential is expressed in the following form:

$$U(r,\Phi,\lambda) = -\frac{\mu}{r} + B(r,\Phi,\lambda) \tag{3.2}$$

Where $B(r,\Phi,\lambda)$ is the spherical harmonic expansion for the correction of Earth gravitational potential. The coordinates used are represented in Figure 3.2, where $\mathrm{R_e}$ is the Earth radius.

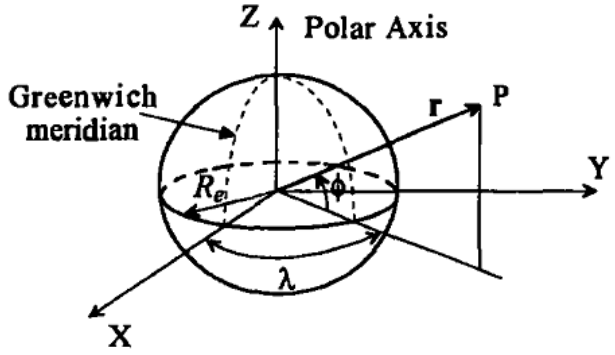

Figure 3.2: Coordinates for the derivation of the oblate Earth gravitational potential [21]

Equation (3.3) represents the infinite series of the geopotential function at any point $P(r,\Phi,\lambda)$ outside the Earth's sphere.

$$B(r,\Phi,\lambda) = \frac{\mu}{r}\left\{\sum_{n=2}^{\infty}\left[\left(\frac{R_e}{r}\right)^n J_n P_n \sin(\Phi) + \sum_{m=1}^{n}\left(\frac{R_e}{r}\right)^n \left(C_{nm}\cos(m\lambda) + S_{nm}\sin(m\lambda)\right) P_{nm}\sin(\Phi)\right]\right\} \tag{3.3}$$

where

- r is the geocentric distance of point P;
- Φ is the geocentric latitude;

- λ is the geographical longitude;
- $\cos(\lambda m)$ and $\sin(\lambda m)$ are harmonic coefficients;
- J_{nm} are zonal harmonic coefficients;
- J_n are zonal harmonic coefficients of order 0;
- P_{nm} is the associated Legendre polynomial of degree n and order m;
- P_n is the Legendre polynomial of degree n and order 0;
- C_{nm} are the tesseral harmonic coefficients for $n \neq m$;
- S_{nm} are the sectoral harmonic coefficients for $n = m$.

As it can be seen from Equation (1.3) the zonal harmonics depend only on the latitude. Figure 3.3 shows their disposition up to 6^{th} degree. J_2 accounts for most of Earth's gravitational departure from a perfect sphere. This band (and others) represents the Earth's oblateness. The shadings in Figure 3.3 indicate regions of additional mass; the numbers link regions between the views. The third harmonic appears similar to J_2 from the top but is reversed from the bottom view [**17**].

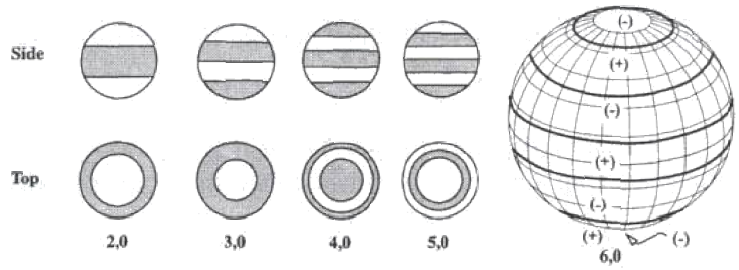

Figure 3.3: Zonal harmonics

Sectoral harmonics take into account the extra mass distribution in longitudinal regions and Figure 3.4 shows their disposition up to 5^{th} degree and order. These harmonics can be thought of as a special case of tesseral harmonics.

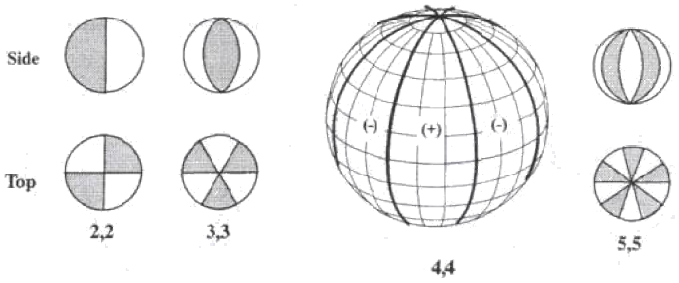

Figure 3.4: Sectoral harmonics

Tesseral harmonics depend both on longitude and latitude and they attempt to model specific regions on the Earth which depart from a perfect sphere. These harmonics are displayed in Figure 3.5.

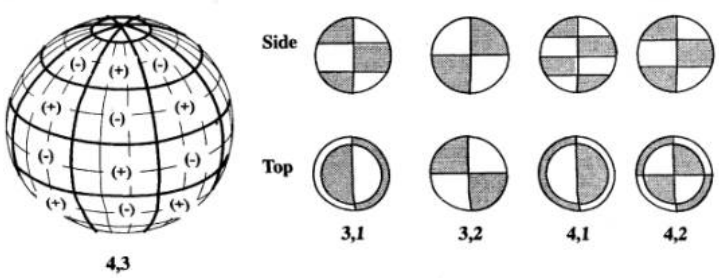

Figure 3.5: Tesseral harmonics

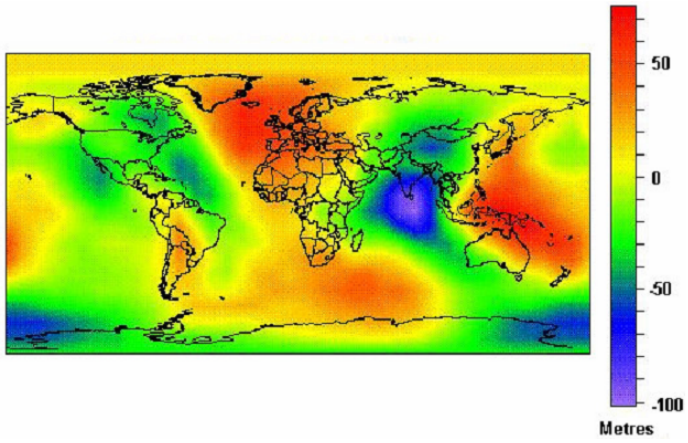

Figure 3.6: The geoid, adapted from fredonia.edu (2006)

3.2.2 Effect on the orbital parameters

Following is a brief summary of the major effects of the Earth's non-homogeneous mass distribution, for a more detailed description please refer to [**17**]:

- Even zonal harmonics induce secular[1] perturbations in Ω, ω and M, while e, a and i don't show any secular effects;
- At the critical inclination of $i = 63.43°$ or $i = 116.6°$, ω have no secular effects due to J_2;
- For polar orbit, all secular and periodic[2] terms in Ω and i are zero, therefore the orbital plane remains fixed;
- All the orbital parameters experience periodic variations induced by all harmonics;

[1] *Secular variations* represent linear variations in the element [**50**].

[2] *Periodic variation*s can be: *short-period variations* which are periodic in the element with a period less than or equal to the orbital period, or long-period variations which have a period greater than the orbital period.

- The magnitude of this kind of perturbations decreases with the orbit's increasing semi-major axis and increases with the orbit's increasing eccentricity.

3.3 Atmosphere

The Earth atmosphere represents the environment where LEO satellites spend the greatest part of their lifetime therefore a deep knowledge on the phenomena that govern it is essential. An object moving through the atmosphere will experience an aerodynamic load proportional to the local density of the gas, therefore this atmosphere propriety of the highest interest for this study. Unfortunately density is extremely difficult to predict due to its dependence on many other quantities and events. In the following paragraphs a brief explanation of the main influencing factor is given [**15**].

3.3.1 Factors affecting the atmospheric density

Altitude

Altitude is the main influence factor for atmospheric density. Density, indeed, decreases from an almost constant value of 1.225 kg/m^3 at the sea level to $1g/km^3$ between 400 km and 600 km.

At low altitudes the atmosphere composition is homogeneous due to the mixing effect of the turbulence, but at 90 km to 100 km the turbulence begins to weaken up to completely fading at the *turbopause* altitude. Above this level the gases tend to separate into fractions according to their molecular weights.

This stratified structure makes it impossible to model the density by following a unique exponential function. Indeed its behaviours is more realistically approximated by a series of different exponential decay zones, each fading into the next. The denser species such as nitrogen and atomic oxygen predominate at lower altitudes, with helium and hydrogen becoming increasingly important at higher altitudes.

Solar activity

It is well known that the Sun activity follows an eleven-year cycle which is characterised by approximately four years of fast increase in the solar activity, followed by a more gradual diminution. As it will be discussed more in detail later, the solar activity is usually defined through the $F_{10.7}$ flux index which, in one cycle, can pass from 80 SFU to 250 SFU and back to the original level.

The solar activity is capable of strongly influencing the atmosphere density. A high solar activity means a great production of high-energy photons which heat the atmosphere, causing the lower strata to expand upwards and, therefore, increase the density in LEO. This effect is so powerful that during high solar activity periods, the atmosphere density can increase 3, 8 and 20 times the original value at 250 km, 400 km and 600 km respectively.

Time of the year

Typically, a density maximum is recorded in April and late October and a minimum in January and October. The second peak events are usually stronger than the first one and the strength of this maximum and minimum is inversely proportional to the solar activity level.

Time of the day

As the sun rises it starts heat the gases in the lower Earth atmosphere, causing their thermal expansion. The phenomena has the same consequence of a solar high activity level, hence the density at high altitude over the illuminated zones increases.

Above 200 km this peak occurs around 14:00 h (diurnal bulge), and a minimum is registered around 04:00 h.

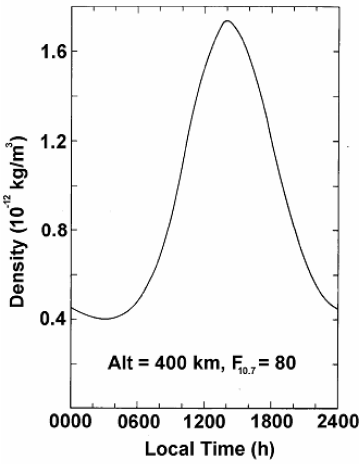

Figure 3.7: Diurnal bulge

Latitude

It has been previously stated that the atmosphere experience a density increment at altitude due to the thermal expansion of the gases at lower levels, therefore it's easy to understand why this effect is more evident during the summer months rather than during the winter. This means that in the same moment, the atmosphere will be more rarefied on the winter hemisphere and denser over the summer one, giving an evidence of the influence of the latitude on the prediction of the density values.

Geomagnetic planetary index

The geomagnetic planetary index A_P is a measure of the general level of geomagnetic activity over the globe for a given (UT) day **[22]**. The A_P average values is weakly related to the eleven year cycle of the solar flux index, indeed its variations between one hour and the other can show fluctuations 10 time stronger than the cyclical ones.

The density is affected by the electrical currents induced by the Earth's magnetic field in the atmosphere. These cause the temperature in the low atmosphere layers to increase, expand, and thicken the gas molecules in at high altitudes. The magnitude of these events can lead to an increment of the density by a factor of 8 at 600 km, but this effect persists only for a small transitory of a few hours and, probably, does not occur again for several weeks or months.

3.3.2 Atmosphere Models

It's now clear the Earth's atmosphere suffers the influence of many factors, some very difficult to accurately predict or model. As shown in Figure 3.8, many different atmosphere models have been created, each correlating differently density and temperature with the various contributing factors. In the first layers of the atmosphere, the density can be represented by an exponential function of the altitude, but this model is valid only up to 500km because then the mean free path molecules become greater than the scale height. In this research such model is too reductive because the test cases under study orbit at a higher altitude; hence a preliminary selection of the atmosphere model has been performed. The ECSS refers to two of these methods: the NRLMSISE-00 and JB-2006, and a comparison between the two is presented in the following paragraphs [**23**].

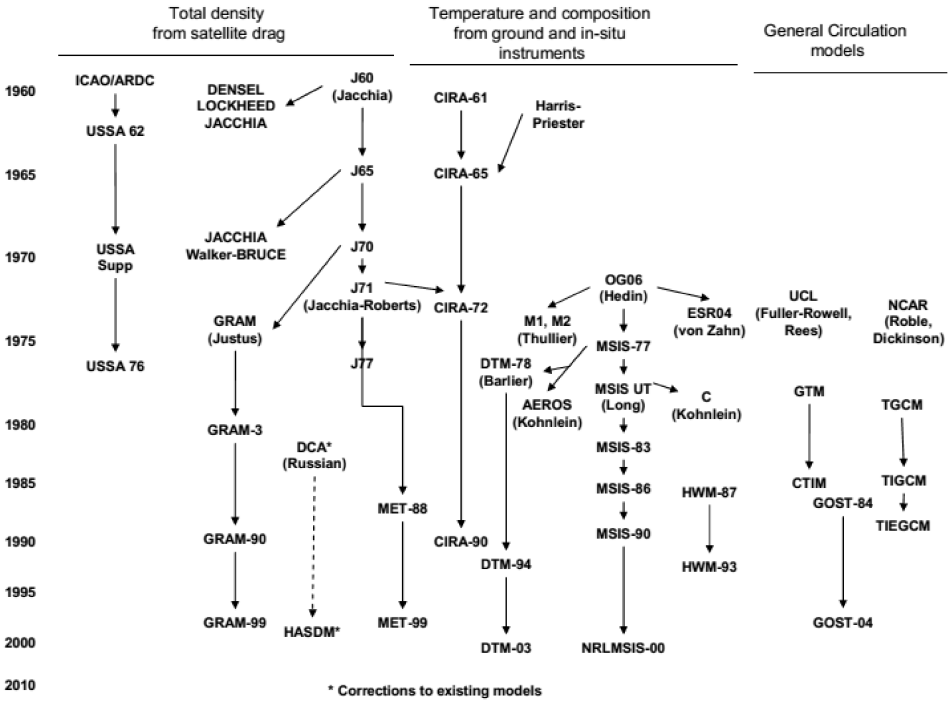

Figure 3.8: Atmosphere models timeline

3.3.2.1 NRLMSISE-00

The NRL Mass Spectrometer, Incoherent Scatter Radar Extended Model (NRLMSISE-00) estimates the temperature and the various air components

densities in Earth's atmosphere **[24]**. It is based on a wide set of data provided by satellites, rockets and radars with extensive temporal and spatial distribution. This empirical model has been validated through several detailed scientific tests against experimental data, therefore is considered very reliable. The NRLMSISE-00 provides a good approximation of the atmosphere characteristics from the ground level to exobase ($<$ 1400 km) and it's dependant on two indices:

- The F10.7 that represents the solar radio flux per unit frequency at a wavelength of 10.7 cm near the peak of the observed solar radio emission. It is a very good indicator of overall solar activity levels and correlates well with solar UV emissions;
- The geomagnetic index A_P, which is a measure of the disturbance in the Earth's magnetic field caused by transient events such as solar flares and coronal mass ejections.

3.3.2.2 JB-2006

The Jacchia-Bowman semi-empirical model (JB-2006) was developed using the CIRA72 model as the basis for the diffusion equations **[25]**. New solar indices based on orbit-based sensor data are used for the solar irradiances in the extreme and far ultraviolet wavelengths. The JB-2006 is validated through comparisons of accurate daily density drag data previously computed for numerous satellites. JB-2006's solar indices involve three components: traditional index $F_{10.7}$, S_{10} based on the data from SOHO EUV sensors, and Mg_{10} based on FUV MgII sensors. JB-2006 is the first significant attempt of using multi-solar-indices to construct a model.

- S_{10} is the 26−34-nm solar EUV radiation flux. The NASA/ESA Solar and Heliospheric Observatory (SOHO) research satellite operates in a halo orbit at the Lagrange Point 1 (L1) on the Earth-Sun line. The data have been normalized and converted to SFU unit through linear regression with $F_{10.7}$, producing the new index S_{10};
- Mg_{10} is translated from MgII index, which was supplied by the NOAA series of operational satellites. Solar MUV radiation near 280 nm was measured by Solar Backscatter Ultraviolet (SBUV) spectrometer fixed in the satellites and calculated to derive MgII.

3.3.2.3 Comparison between NRLMSISE-00 and JB-2006

In this section, the accuracy of the NRLMSISE-00 and the JB-2006 models will be analyzed and compared under different conditions **[25]**.

Response of models to the Sun burst event in October, 2003.

In October 2003 a strong solar burst lasting for 25 days took place and generated a growth of the $F_{10.7}$ and fluctuations of the other indices. Compared with CHAMP (a gravitational science satellite) observation, JB-2006 is the closest to the real values but by analyzing the small-scale variation signal in CHAMP measurement we notice that both models underestimated the maximum densities. This implies that

the models have difficulty in depicting the small-scale variation of local atmosphere, because they are restricted by the model mechanism and its sample distribution.

Model accuracy in solar long-term variation

The accuracy of the models during solar long-term variation is studied analyzing their relative error and standard deviation compare to CHAMP density measurements from 2001 to 2005. The results shows that in the quiet and moderate solar activity JB-2006 is close to NRLMSISE-00, but under a high active condition JB-2006 is obviously better, implying that the multi-solar-indices S_{10} and Mg_{10} can effectively improve the model accuracy. However, the JB-2006 requires also more complex and time-demanding manipulations of data. The NRLMSISE-00, on the other hand, is capable of producing a considerable level of accuracy without compromising simulation performances. Hence, the NRLMSISE-00 has been chosen for this study.

3.3.2.4 Solar indices

The NRLMSISE-00 is based on the solar flux index $F_{10.7}$ and the magnetic index $A_{P.}$ These values are widely available and constantly updated with the real measurements. For this study such indexes were taken from the archives of **[26]** which are based on data from the National Geophysical Data Center (NGDC) in the National Oceanic and Atmospheric Administration (NOAA). This source provides the daily space weather data from 1957 to the current date; it also includes predicted parameters but they will not be used for reasons explained in section 3.3.2.5. However, only some of the parameters provided are needed in the model here described. Following is a brief description of the effectively necessary parameters.

Columns	Description
001-004	Year
006-007	Month (01-12)
009-010	Day
048-050	Planetary Equivalent Amplitude (A_P) for 0000-0300 UT.
052-054	Planetary Equivalent Amplitude (A_P) for 0300-0600 UT.
056-058	Planetary Equivalent Amplitude (A_P) for 0600-0900 UT.
060-062	Planetary Equivalent Amplitude (A_P) for 0900-1200 UT.
064-066	Planetary Equivalent Amplitude (A_P) for 1200-1500 UT.
068-070	Planetary Equivalent Amplitude (A_P) for 1500-1800 UT.
072-074	Planetary Equivalent Amplitude (A_P) for 1800-2100 UT.
076-078	Planetary Equivalent Amplitude (A_P) for 2100-0000 UT.
080-082	Arithmetic average of the 8 A_P indices for the day.
094-098	10.7-cm Solar Radio Flux (F10.7) Adjusted to 1 AU. Measured at Ottawa at 1700 UT daily from 1947 Feb 14 until 1991 May 31 and measured at Penticton at 2000 UT from 1991 Jun 01 on. Expressed in units of 10-22 W/m2/Hz.
102-106	Centered 81-day arithmetic average of F10.7 (adjusted).
108-112	Last 81-day arithmetic average of F10.7 (adjusted).
114-118	Observed (unadjusted) value of F10.7.
120-124	Centered 81-day arithmetic average of F10.7 (observed).
126-130	Last 81-day arithmetic average of F10.7 (observed).

Table 3.1: NRLMSISE-00

The difference between the observed and adjusted values is that the first ones are measured at the true Sun-Earth distance, while the second ones are at the constant distance of 1 AU.

The NRLMSISE-00 model requires:

- 81-day average of $F_{10.7}$ flux, cantered on day of year;
- Daily $F_{10.7}$ flux for previous day;
- Daily magnetic index A_P;
- hour A_P for current time;
- hour A_P for 3 hours before current time;
- 3 hour A_P for 6 hours before current time;
- 3 hour A_P for 9 hours before current time;
- Average of eight 3 hour A_P indices from 12 to 33 hours before current time;
- Average of eight 3 hour A_P indices from 36 to 57 hours before current time;

However, solar and magnetic parameters are time dependant and therefore this data collection has to be performed for each time step, appreciably slowing down the simulation. Hence a simpler table has been created without relevant accuracy loss. The reduced table contains the date information and monthly average of the space weather parameters. This allows for lighter atmosphere update and computation routine, saving simulation time and effort.

Figure 3.9 and Figure 3.10 show, respectively, the $F_{10.7}$ and A_P trends obtained from the date stored in the reduced solar indexes table. These results have been compared to the original daily ones and no relevant differences were observed. From these graphs is also possible to notice the 11-years cyclicality of the parameters due to the solar activity periodicity.

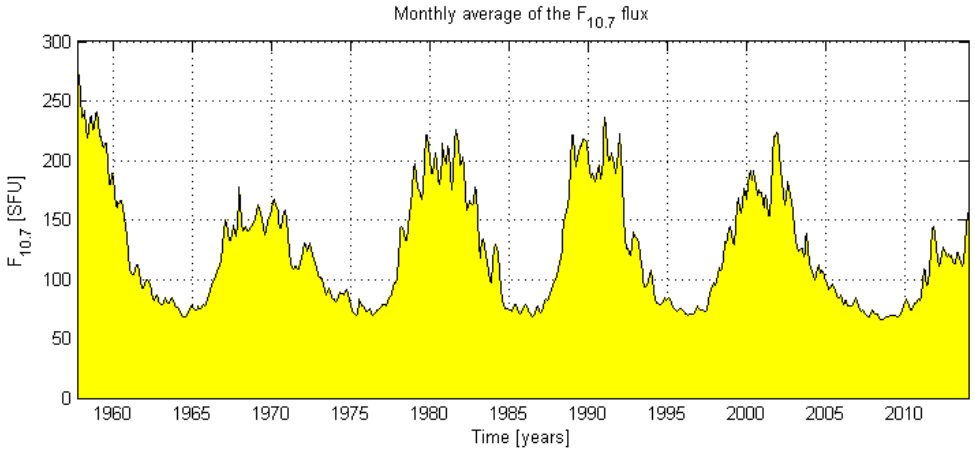

Figure 3.9: Monthly average of F10.7 from 1957 to 2014

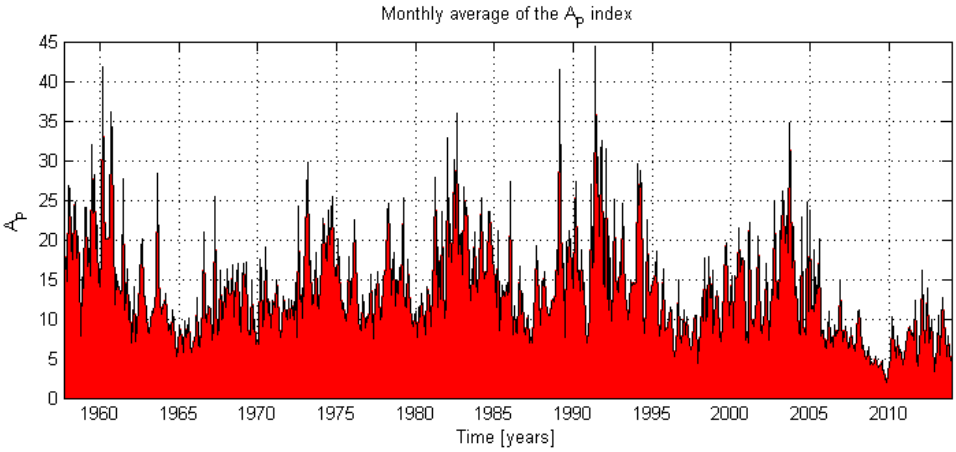

Figure 3.10: Monthly average of A_p from 1957 to 2014

3.3.2.5 Prediction of future data

As anticipated, the use of prediction methods for future solar and magnetic indexes has been analyzed. However, implementing the code for such prediction methods would have required a great time expense and, since this was not the main topic of the present research, it has been decided to cope with this problem using a set of predicted data already available. This information has been retrieved from the Schatten files **[27]**.These files generally span about one or two solar cycles and are periodically re-issued (about 3 to 4 times per year) to provide improved accuracy to the observed progress of each solar cycle. This is sufficient for many planning operations.

Figure 3.11 shows two different predictions of the $F_{10.7}$ from Schatten compared to the real available data.

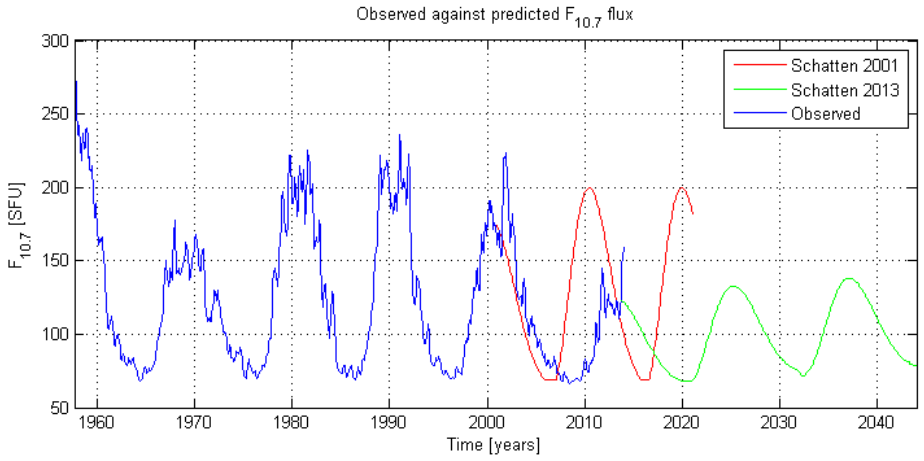

Figure 3.11: Comparison between measured and predicted F10.7 flux values

It's easy to see the mismatch in phase and magnitude of the different predictions. Given the variability of the accuracy of predicted data, and since within this

research large time-span of future data would have been necessary, it was decided not to use predicted space weather data. Instead, for simulation of future epochs, a simple shift to an equivalent moment in a past solar cycle shall be performed. The magnitude of this shift was selected manually case by case, in order to identify the most similar situation in the available past data.

3.3.2.6 NRLMSISE-00 validation

In order to validate the implemented NRLMSISE-00 model, a comparison between the density profile obtained with the monthly averaged solar indexes and the daily-data-based one provided by the NASA Coomunity Coordinated Modelling Center[**28**] is performed. The position and epochs at which the evaluation has been performed are

Position	
Altitude	500 km
Latitude	0°
Longitude	0°

Epoch	
Initial date	01/01/1961
Final date	01/01/2012

Table 3.2: Density comparison against time initial conditions

As Figure 3.12 shows, no considerable mismatching between the two profiles can be noticed. The more definite discrepancies between the curves are caused by the difference between the monthly averaged solar index and the observed one on the first day of the relative month: the greater this discrepancy is, the more distant the two density profiles are. However, the overall matching with the approximated model is satisfactory, hence, the implemented NRLMSISE-00 atmosphere model can be considered validated.

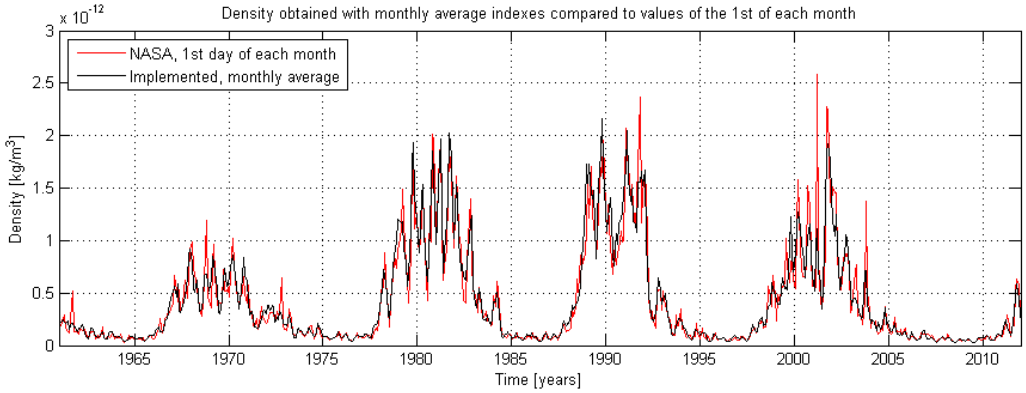

Figure 3.12: Density comparison between NASA NRLMSISE-00 daily-indexes and averaged-indexes implemented model for different dates

A further proof of the validity of the averaged NRLMSISE-00 model is given in Figure 3.13 where a comparison of the density against altitude is performed. This evaluation has been made for dates from the 1st of January 2009 to the 1st of January 2012, but the results of the year 2010, being too close to 2011 ones, have not been plotted for quality reasons.

Position	
Altitude	100-1000 km
Latitude	0°
Longitude	0°

Epoch	
1st date	01/01/2009
2nd date	01/01/2011
3rd date	01/01/2012

Table 3.3: Density comparison against altitude initial conditions

As expected, the implemented model results are perfectly superimposable with the NASA density profiles, confirming the accuracy of the average-indexes model.

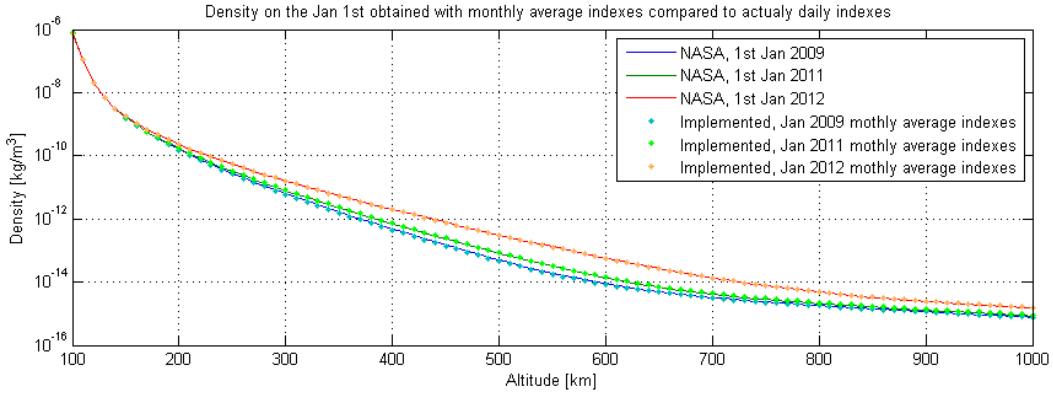

Figure 3.13: Density comparison between NASA NRLMSISE-00 daily-indexes and averaged-indexes implemented model on the first of January, for different altitude

3.3.3 Atmospheric drag

The interaction of the gas molecules in the atmosphere with the orbiting bodies causes a drag force [**29**]. In LEO this effect is especially strong due to the (still) considerable atmospheric density. The aerodynamic force acting on the orbiting object depends on many factors; the most relevant are the air density, the velocity with respect to the gas and the cross-sectional area of the object. The aerodynamic force on a flat surface can be described by

$$F_{aero} = -\varrho \,|\, \underline{v}_{rel} \,|^2 \; A \cos\vartheta \left[\sigma_t \hat{\underline{v}}_{rel} + \left(\sigma_n \left(\frac{v_b}{|\, \underline{v}_\infty \,|} \right) + \left(2 - \sigma_n - \sigma_t \right) \cos\vartheta \right) \underline{n} \right] \qquad (3.4)$$

where

- ϱ is the local atmospheric density;
- A is the surface area;
- $\underline{v}_{rel}$ is the velocity of the object with respect to the atmosphere[3];
- $\hat{\underline{v}}_{rel}$ is the versor of $\underline{v}_{rel}$;
- ϑ is the angle between $\underline{v}_{rel}$ and the normal to the surface;

[3] It is assumed that $\underline{v}_{rel}$ is dominated by the orbital velocity and rotation of the atmosphere while the random thermal motion of the individual gas molecules is ignored.

- σ_t and σ_n are, respectively, the tangential and the normal accommodation coefficients;
- $\frac{v_b}{|\underline{v}_\infty|}$ is the ratio between the molecular exit velocity and the velocity of the incoming molecules. Therefore, $\underline{v}_\infty = -\underline{v}_{rel}$.

The velocity of the object relative to the atmosphere is

$$\underline{v}_{rel} = \underline{v} - \underline{\omega}_E \times \underline{r} \tag{3.5}$$

where $\underline{v}$ is the inertial velocity of the object, $\underline{r}$ is its position relative to the Earth and $\underline{\omega}_E$ is the Earth angular velocity vector.

For orbits above 200km the atmosphere is so rarefied that the linear dimension of the body D is smaller than the mean free path λ_0 in the flow. This type of stream is called free-molecule flow and is valid when:

$$\frac{\lambda_0}{L} >> \frac{|\underline{v}_\infty|}{v_b} \tag{3.6}$$

According to the kinetic theory of gases, v_b depends on the type of gas understudy and it is related to the surface temperature T_s as follows:

$$v_b = \left(\frac{\Re T_s \pi}{2m}\right)^{1/2} \tag{3.7}$$

where

- $\Re = 8.314$ J / kmol K is the universal gas constant;
- m the gas molecular weight.

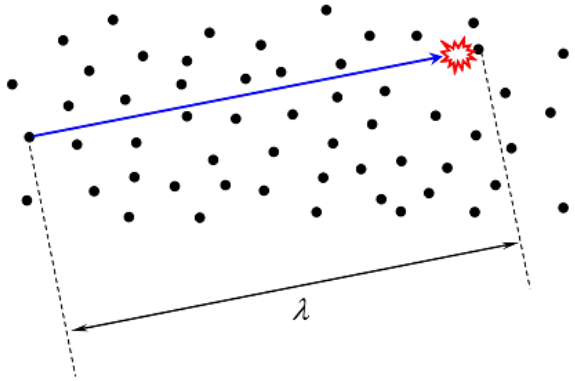

Figure 3.14: Molecular mean free path

The total momentum of the satellite is influenced by the energy transferred by the impacting gas molecules on the surface and by the surface accommodation coefficient α [**30**]. This latter parameter indicates how closely the kinetic energy of the incoming molecule has adjusted to the thermal energy of the surface. The surface accommodation coefficient is expressed by

$$a = \frac{E_{ki} - E_{kr}}{E_{ki} - E_{kw}} \tag{3.8}$$

where

- E_{ki} is the kinetic energy of the incident molecule;
- E_{kr} is the kinetic energy of the reemitted molecule;
- E_{kw} is the kinetic energy that the incident molecule would have if it left the surface at the at the surface temperature.

A surface with complete accommodation is indicated by $a = 1$ and is often called diffuse scattering, while no accommodation is mentioned as specular scattering and means $a = 0$. In Figure 3.15 these two types of reflection can be observed.

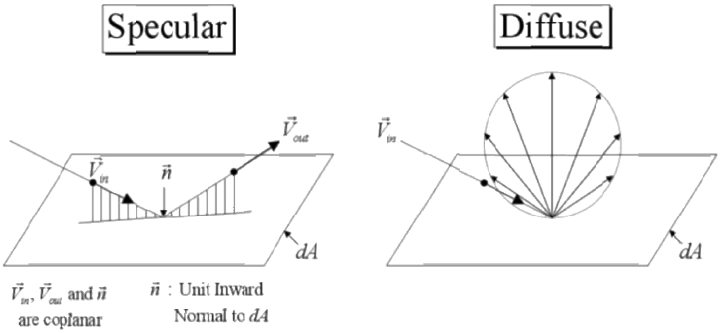

Figure 3.15 Specular and Diffuse Molecular Reflection

The surface accommodation coefficient is a propriety that highly depends on the amount of adsorbed molecules on the surface; the lower this adsorbtion is, the less energy is lost in the reflection of the molecule, but when the surface is contaminated the scattering is more diffuse and leads to a higher accommodation. Unfortunately this contamination process take place at low altitude orbits and, therefore, the drag and lift coefficients cannot be considered constant during the deorbiting path.

The surface accommodation coefficient can be divided in normal and tangential components, respectively σ_n and σ_t, which are usually calculated empirically for different gas species present in LEO. For this thesis the surface accommodation coefficients and the ratio $\frac{v_b}{|\underline{v}_\infty|}$ are considered constant and with values depending on the studied case. Table 3.4 shows two common selections of these proprieties for a sail.

	Case	
Constant	**Normal accommodation**	**Typical Solar Sail**
σ_n	1	0.8
σ_t	0	0.8
$\frac{v_b}{\lvert \underline{v}_\infty \rvert}$	0	0.05

Table 3.4: Aerodynamic surface momentum transfer constants

3.4 Solar Radiation Pressure Force

A LEO satellite is subjected also to the influence of the solar radiation pressure due to the impact of solar photons which cause a variation in the orbiting object momentum.

In general, when a flux of photons collides with a surface, a part of those is reflected (specularly and diffusely) and the rest is either absorbed or transmitted. Defining τ as the transmitted fraction of the total light stream and β as the fraction of the total incoming photon flow that interacts with the surface, we can state **[31]**:

$$\tau + \beta = 1 \tag{3.9}$$

Furthermore, the summation of the fractions of β of photons that are absorbed and reflected by the surface must be equal to 1. This conservation can be expressed as follows:

$$\varrho_a + \varrho_s + \varrho_d = 1 \tag{3.10}$$

where

- ϱ_a is the fraction of β that is absorbed by the surface;
- ϱ_s is the fraction of β that is specularly reflected by the surface;
- ϱ_d is the fraction of β that is diffusely reflected by the surface.

In Equation (3.10), obviously, the transmitted photons don't play any role since, for definition, they don't interact with the surface.

The equation (3.9) can hence be written as:

$$\tau + \beta\varrho_a + \beta\varrho_s + \beta\varrho_d = 1 \tag{3.11}$$

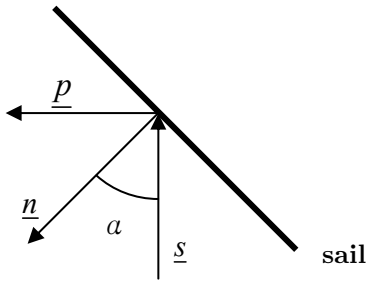

Figure 3.16 : Non-perfect flat solar sail.

Assuming all photons interacting with the surface are firstly absorbed, the force acting on such surface is given by

$$\underline{F}_{\varrho a} = (1-\tau)PA\cos(a)\,\underline{s} \tag{3.12}$$

Where $A\cos(a)$ is the projected surface area in the direction $\underline{s}$, the unit vector from the Sun to the surface, and $P = 4.563 \text{ x } 10^{-6}$ N/m^2 is the nominal solar radiation pressure constant at 1 AU from the Sun.

Using equation (3.9) and expressing the reflection contribution of the force $\underline{F}_{\varrho_s}$ and $\underline{F}_{\varrho_d}$, we obtain:

$$\begin{aligned}\underline{F}_{\varrho_a} &= (1-\tau)PA\cos(a)\underline{s} \\ \underline{F}_{\varrho_s} &= -(1-\tau)\varrho_s PA\cos(a)\underline{p} = -(1-\tau)\varrho_s PA\cos(a)\left(\underline{s}+2\cos(a)\underline{n}\right) \\ \underline{F}_{\varrho_d} &= -(1-\tau)B_f\varrho_d PA\cos(a)\underline{n}\end{aligned} \tag{3.13}$$

The specularly reflected photons create an outgoing angle of reflection equals to the angle of incidence a (mirror-like reflection), while in the diffusely case, the incident photons are reflected in many directions. The coefficient B_f indicates that the surface is non-Lambertian. A Lambertian surface appears equally bright from all directions, hence, B_f describes the deviation from this condition. Assuming an ideal sail $B_f = 2/3$.

The summation of the three force components reported in equations (3.13) defines the total solar radiation pressure $\underline{F}_{SRP}$ on a non-Lambertian flat surface.

$$\underline{F}_{SRP} = (1-\tau)PA\left(-\underline{s}\cdot\underline{n}\right)\left[(1-\varrho_s)\underline{s}-\left(2\varrho_s\left(-\underline{s}\cdot\underline{n}\right)+\frac{2}{3}\varrho_d\right)\underline{n}\right] \tag{3.14}$$

It can be seen from the (3.14), the solar radiation pressure force can be divided in two components: one normal to the surface and the other in the opposite direction of the Sun light. An ideal solar sail provides only specular reflection because the resulting force is twice as large as in the case of full absorption. This explains why solar sails are typically covered with a high reflectance coating.

The optical proprieties of a plane depend on its material. Table 3.5 shows some possible cases, including also a typical solar sail surface.

	Case			
Constant	**Black Surface**	**Transparent Surface**	**Mirror Surface**	**Typical Solar Sail**
τ	0.00	1.00	0.00	0.00
ϱ_a	1.00	0.00	0.00	0.17
ϱ_s	0.00	0.00	1.00	0.83
ϱ_d	0.00	0.00	0.00	0.00

Table 3.5: Sail optical proprieties

3.4.1 Eclipse

A spacecraft orbiting the Earth experiences, in most of the cases, partial or full eclipse when it passes through the night-side of the Earth. These partial or total eclipse conditions correspond to the regions known as penumbra and umbra (Figure 3.17). The umbra region receives no direct light from the Sun, hence, there is no solar radiation pressure while the penumbra region receives partial light and is quite small, therefore in this conditions the SRP can be neglected [**32**]. The ESCM models both the umbra and penumbra areas, evaluating the respective cones.

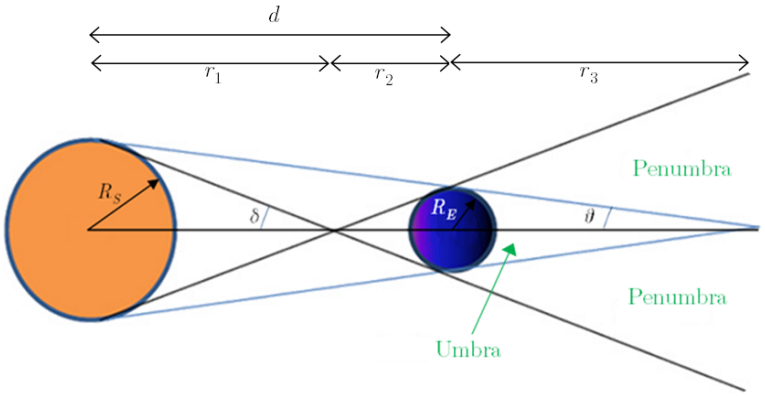

Figure 3.17: Eclipse geometry [32]

With simple trigonometry it is possible to identify the thresholds of umbra and penumbra regions. The angles δ and ϑ represented in Figure 3.17 are computed as

$$\sin(\delta) = \frac{R_S}{r_1} = \frac{R_E}{r_2} \quad , \qquad \sin(\vartheta) = \frac{R_S}{d + r_3} = \frac{R_E}{r_3} \tag{3.15}$$

Knowing that

$$r_1 + r_2 = d \tag{3.16}$$

from the equations (3.15) and (3.16) results

$$r_2 = \frac{R_E}{R_S}(d - r_2) = \frac{d}{1 + \frac{R_S}{R_E}} \tag{3.17}$$

$$r_3 = \frac{R_E}{R_S}(d + r_3) = \frac{d}{\frac{R_S}{R_E} - 1} \tag{3.18}$$

Obtaining the values of the three vectors $\underline{r}_1, \underline{r}_2$ and $\underline{r}_3$ as function only of the distance between the Sun and the Earth.

Defining $\hat{\underline{s}}$ as the unit vector directed from the Sun to Earth and $\underline{r}$ as the position vector of the spacecraft with respect to the Earth, if

$$\left|\underline{r} - (\underline{r} \cdot \hat{\underline{s}})\hat{\underline{s}}\right| < \left|\frac{R_E}{\cos(\delta)}\left(1 + \frac{\underline{r} \cdot \hat{\underline{s}}}{r_2}\right)\right| \quad \text{with} \quad \underline{r} \cdot \hat{\underline{s}} > 0 \tag{3.19}$$

is true the spacecraft is in either penumbra or umbra. And if the condition

$$\left|\underline{r} - (\underline{r} \cdot \hat{\underline{s}})\hat{\underline{s}}\right| < \left|\frac{R_E}{\cos(\vartheta)}\left(1 - \frac{\underline{r} \cdot \hat{\underline{s}}}{r_3}\right)\right| \tag{3.20}$$

is met the spacecraft is passing through an umbra region.

4 System Modelling

In this chapter three orbital simulators with different fidelity levels are described and validated. Starting with a three degrees of freedom model and increasing the accuracy to a six degrees of freedom one and ending the chapter with the introduction of flexible structures and a comparison between the simulators. For each of them, the implemented dynamics, perturbations and integration approach are here expounded.

4.1 3 DoF simulator

4.1.1 Simulator description and diagram

The three degrees of freedom orbital simulator uses a low fidelity model assuming the whole deorbiting system as a point mass with constant ballistic coefficient B_c, which is defined as

$$B_c = \frac{m}{A C_D} \tag{4.1}$$

where

- m is the mass of the system;
- A is the projected area of the system;
- C_D is the drag coefficient of the system.

The conceptual design of the 3 DoF simulator is shown in Figure 4.1, in which $\underline{x}$ represents the state vector containing velocity and position of the deorbiting system.

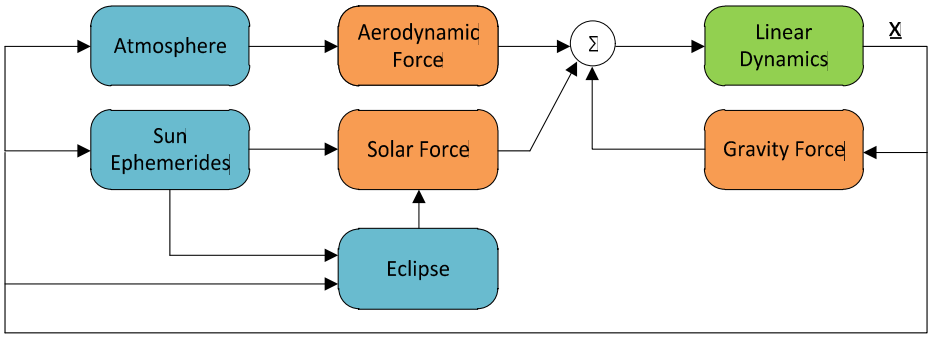

Figure 4.1: 3 DoF simulator diagram

The 3 DoF simulator receives as input the initial orbital parameters and epoch, needed to establish the spacecraft initial condition and Sun ephemerides. It also has as input the solar activity index table from that initial epoch onwards. A detailed list of all input variables is presented in Appendix A.1.2. In the same Appendix is also reported the validation testing for this simulator.

4.1.2 Equations of motion

Since the system is assumed to be a point mass, only its linear dynamics is propagated.

The integration method used is ode45, which is based on an explicit Runge-Kutta (4,5) formula, the Dormand-Prince pair, available in Simulink.

4.1.3 Linear dynamics

In a rigid-body, the sum of all applied forces $\underline{F}$ equals the time derivative of the linear momentum about the centre of mass with respect to the inertial reference frame I [**33**].

$$\frac{{}^{I}d}{dt}\underline{p} = \underline{F} \tag{4.2}$$

where the total linear momentum $\underline{p}$ of the centre of mass of the rigid-body is given by

$$\underline{p} = m\underline{v} \tag{4.3}$$

The linear kinematics is

$$\frac{d\underline{r}}{dt} = \underline{v} \tag{4.4}$$

The total force applied $\underline{F}$ is the summation of the aerodynamic $\underline{F}_{aero}$, solar $\underline{F}_{SRP}$ and gravity $\underline{F}_{G}$ contributions.

$$\underline{F} = \underline{F}_{aero} + \underline{F}_{SRP} + \underline{F}_{G} \tag{4.5}$$

Integrating the equation (4.2) the velocity of the rigid body is obtained, and with a further integration also the position can be computed. The state vector $\underline{x}$ is therefore composed.

4.1.4 Perturbations

4.1.4.1 Gravity model

For the purpose of this research, an Earth potential model (Section 3.2.1) with zonal harmonic coefficients can be used. This is given by

$$U \approx -\frac{\mu}{r}\left[1 - \sum_{n=2}^{\infty}\left(\frac{R_e}{r}\right)^n J_n P_n \sin(\Phi)\right] \tag{4.6}$$

Legendre polynomials up to 4$^{\text{th}}$ degree have been considered:

$$
\begin{aligned}
P_0 &= 1 \\
P_2 &= \frac{1}{2}\left(3\sin^2(\Phi)-1\right) \\
P_3 &= \frac{1}{2}\left(5\sin^3(\Phi)-3\sin(\Phi)\right) \\
P_4 &= \frac{1}{8}\left(35\sin^4(\Phi)-30\sin^2(\Phi)+3\right)
\end{aligned}
\tag{4.7}
$$

The correspondent zonal harmonics coefficients J_n are:

$$
\begin{aligned}
J_2 &= -1.082626\times10^{-3} \\
J_3 &= 2.532656\times10^{-6} \\
J_4 &= 1.619621\times10^{-6}
\end{aligned}
\tag{4.8}
$$

The local acceleration of gravity is the gradient vector of the potential function along the directions of the local axis system [**34**]:

$$
\underline{G} = \nabla U = \begin{bmatrix} \dfrac{\partial U}{\partial R} \\ \dfrac{1}{R\cos(\delta)}\left(\dfrac{\partial U}{\partial \lambda}\right) \\ \dfrac{1}{R}\left(\dfrac{\partial U}{\partial \delta}\right) \end{bmatrix}
\tag{4.9}
$$

$$
\underline{G} = \frac{-\mu}{R^2}\begin{bmatrix} 1+\frac{3}{2}J_2\left(\frac{R_E}{R}\right)^2\left(1-3\sin^2(\delta)\right)+2J_3\left(\frac{R_E}{R}\right)^3\left(3-5\sin^2(\delta)\right)\sin(\delta)-\frac{5}{8}J_4\left(\frac{R_E}{R}\right)^4\left(3-30\sin^2(\delta)+35\sin^4(\delta)\right) \\ 0 \\ 3J_2\left(\frac{R_E}{R}\right)^2\sin(\delta)\cos(\delta)+\frac{3}{2}J_3\left(\frac{R_E}{R}\right)^3\left(5\sin^2(\delta)-1\right)\cos(\delta)-\frac{1}{2}J_4\left(\frac{R_E}{R}\right)^4\left(15\sin(\delta)-35\sin^3(\delta)\right)\cos(\delta) \end{bmatrix}
\tag{4.10}
$$

Therefore the gravitational force acting on a body of mass m is:

$$
\underline{F}_G = m\underline{G}
\tag{4.11}
$$

4.1.4.2 Aerodynamic model

The aerodynamic force acting on a mass point can be approximated with the component along the velocity direction. The representative expression is given by Equation (4.12).

$$
\underline{F}_{aero} = \varrho\left|\underline{v}_\infty\right|^2 B_c\,\hat{\underline{v}}_\infty
\tag{4.12}
$$

where

- ϱ is the local atmosphere density (Section 3.3.2.1);
- $\underline{v}_\infty$ is the velocity of the flow respect to the object.
- B_c is the ballistic coefficient.

4.1.4.3 SRP model

Dealing with a low fidelity simulator, a simplified SRP model has been adopted. The $\underline{F}_{SRP}$ is defined as follows [**17**]:

$$\underline{F}_{SRP} = PAC_R\hat{\underline{s}} \tag{4.13}$$

where

- $P = 4.563 \times 10^{-6} N / m^2$ is the nominal solar radiation pressure constant at 1 AU from the Sun;
- A is the cross sectional area;
- C_R is the coefficient of reflectivity, a material propriety with ranges from 0.0 to 2.0. A coefficient of reflectivity of 0.0 indicates that the body is translucent to incoming radiation. A value of 1.0 means that all the radiation is absorbed and all the force is transmitted (i.e. black body). Finally, 2.0 represents a perfectly reflective body and in this case twice the force is transmitted (i.e. a flat mirror-like surface perpendicular to the radiation source).

The eclipse phenomenon is taken into account in this simulator.

4.2 6 DoF Simulator

4.2.1 Simulator description and diagram

In the 6 DoF simulation tool the deorbiting system is modelled as a tridimensional rigid body, formed by the spacecraft, the drag sail and a connection mast as described in Section 2.2

This simulator is of higher fidelity with respect to the 3 DoF one because it takes into account also the attitude of the system and the implemented models are more accurate.

The conceptual design of the 6 DoF simulator is shown in Figure 4.2, in which $\underline{x}$ represents the state vector containing velocity and position of the deorbiting system, and also its angular velocity and rotations.

The 6 DoF simulator receives as input the initial orbital parameters and epoch, needed to establish the spacecraft initial condition and Sun ephemerides, and the solar activity index table from that epoch onwards. Furthermore, also the geometrical and inertial proprieties of each deorbiting system components must be provided to the simulator. A detailed list of all input parameters of this simulator is shown in Appendix A.2.2. In this same Appendix is also presented the validation test report for this tool.

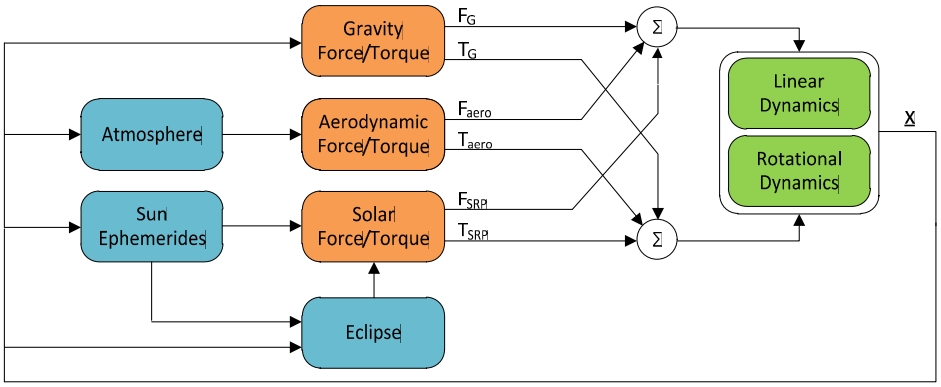

Figure 4.2: 6 DoF simulator diagram

4.2.2 Geometry definition

There are no standard dimensions and geometry able to include all the LEO debris since those depends on many factor such as the mission objective, the allocated space on the launcher, the type of payload, etc. To be able to model most of those objects a parametric tool has been developed. Through the interface, the user can specify several geometrical and physical proprieties which allow the creation of a simplified model of the host. Moreover, the deorbiting system design process is based on the possibility to tune the sail and mast characteristics in order to obtain the desired performances. Hence, also the proprieties of these objects are totally dependent on the user input.

Despite the infinite numbers of possible configuration of the system, the simulator allows the implementation only of a limited number of geometrical shapes. In the next paragraph these possibilities are described.

All the following definitions are expressed in the respective body reference frame.

Host spacecraft

The first main option is related to the shape of the spacecraft model, which can be

- Cuboid;
- Cylinder.

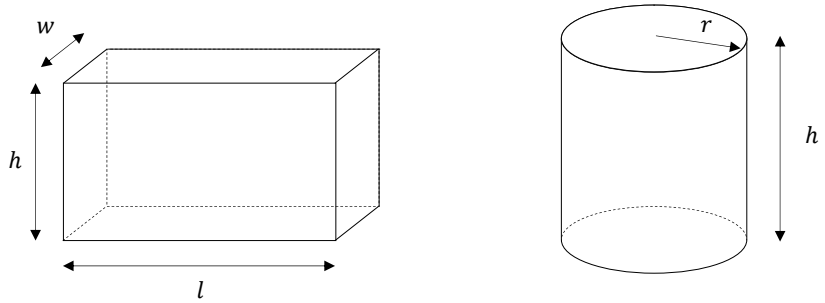

Figure 4.3: Optional spacecraft shapes and their defining dimensions.

For a cuboid length, height and width must be specified, while for a cylinder, the height and radius are necessary. Due to, later on described, surface discretization, the cylindrical shape is here modelled as a n-gonal prism where n should have a high value (>20).

The calculation of the inertia matrix of the host is then the following for a cuboid:

$$\underline{\underline{J}}_{cuboid} = \frac{1}{12} m_{sat} \begin{bmatrix} w^2 + h^2 & 0 & 0 \\ 0 & l^2 + w^2 & 0 \\ 0 & 0 & l^2 + h^2 \end{bmatrix} \tag{4.14}$$

where l is the length (along x), w is the width (along y) and h is the height (along z). And for a cylinder:

$$\underline{\underline{J}}_{cylinder} = \frac{1}{2} m_{sat} \begin{bmatrix} \frac{1}{2}r^2 + \frac{1}{6}h^2 & 0 & 0 \\ 0 & r^2 & 0 \\ 0 & 0 & \frac{1}{2}r^2 + \frac{1}{6}h^2 \end{bmatrix} \tag{4.15}$$

where r is the cylinder radius and h is the height.

The mass of the satellite m_{sat} has been assumed to be constantly distributed but in case the realistic inertial proprieties of the object are known, it's possible to input those manually.

Drag Sail

A parametrical approach has been adopted also for the modelling of the sail as well; indeed this object has to be tuned to permit the deorbiting of the host in the selected range of time.

The shape of the sail can assume two different configurations:

- Pyramid shell;
- Cone shell.

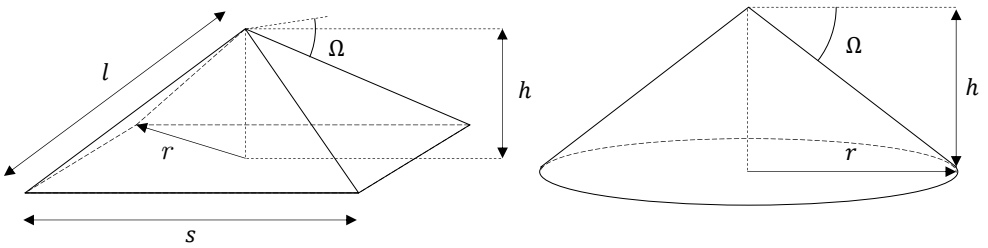

Figure 4.4: Optional sail shapes and their defining dimensions

In real sails, these shapes are implemented as n isosceles triangular faces where the lateral sides are supported by booms. The cone is then a pyramid whose number of triangles approaches infinity.

For both shapes the geometrical information need is: the radius r of the base (which in the square pyramid is the radius of the circle that circumscribe the square base) and the angle Ω which represents the inclination of the booms respect to the x-z plane. For the cone also the number of faces must be set (usually large, >20).

The relationship between these parameters and the remaining characteristics of the pyramid/cone are:

$$l = \frac{r}{\cos(\Omega)} \ , \quad h = r\tan(\Omega) \ , \quad s = 2r\sin\left(\tfrac{\pi}{n}\right) \tag{4.16}$$

where l is the length of each boom, h is the height of the pyramid/cone, s is the side of polygonal base and n is its number of sides.

The calculation of the inertia matrix of the sail follows the relations below

$$\underline{\underline{J}}_{pyramid} = \frac{1}{3} m_{sail} \begin{bmatrix} r^2 & 0 & 0 \\ 0 & \frac{l^2}{2} - \frac{h^2}{3} & 0 \\ 0 & 0 & \frac{l^2}{2} - \frac{h^2}{3} \end{bmatrix} \tag{4.17}$$

$$\underline{\underline{J}}_{cone} = \frac{1}{2} m_{sail} \begin{bmatrix} \frac{1}{2}r^2 + \frac{1}{9}h^2 & 0 & 0 \\ 0 & r^2 & 0 \\ 0 & 0 & \frac{1}{2}r^2 + \frac{1}{9}h^2 \end{bmatrix} \tag{4.18}$$

The mass of the sail m_{sail} has been assumed to be constantly distributed but in case the realistic inertial proprieties of the sail are known, it's possible to override these calculations with manual inputs.

Mast

This structural piece is another design variable that should be possible to define as desired. The mast is assumed as a square section beam structure and the tuning parameters are the length L and the section values of height h and width w; furthermore, since it's an hollow object, also the thickness t must be defined.

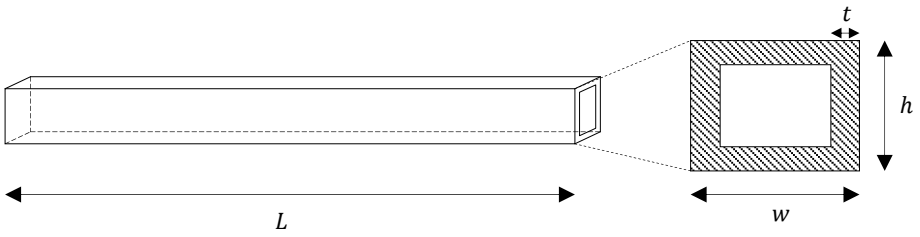

Figure 4.5: Mast shape and defining dimensions

The calculation of the inertia matrix of the uses the following expression:

$$\underline{\underline{J}}_{mast} = \frac{m_{mast}}{24}\frac{wh}{t(w+h-2t)}\begin{bmatrix} w^2+L^2 & 0 & 0 \\ 0 & h^2+w^2 & 0 \\ 0 & 0 & L^2+h^2 \end{bmatrix} - \frac{m_{mast}}{12}\left(\frac{wh}{t(w+h-2t)}-1\right)\begin{bmatrix} (w-2t)^2+L^2 & 0 & 0 \\ 0 & (w-2t)^2+(h-2t)^2 & 0 \\ 0 & 0 & L^2+(h-2t)^2 \end{bmatrix} \tag{4.19}$$

The m_{mast} has been assumed to be constantly distributed but in case the realistic inertial proprieties of the sail are known, it's possible to input those manually.

However, it has been assumed that the mast in the 6 DoF has negligible surface, therefore it contributes only to the total system mass and inertia, but not to the calculation of the aerodynamic and solar force.

Total configuration

Once the geometry of each component is defined, they are assembled to form the deorbiting system. This assembly is performed through the definition of the attachment point of the mast on the satellite while for the sail this connection it's assumed to be done always at the vertex of the pyramid/cone. Moreover, the relative attitude of each body has to be defined. The total inertia of the system is then evaluated by rotating and translating (parallel axis theorem) each inertia constituent into the total body frame B centred in the total CoM of the system. The transformation of an inertia matrix $\underline{\underline{J}}$ of a body, expressed in a generic reference frame A into another frame B is performed as follows:

$$\underline{\underline{J}}^B = \underline{\underline{C}}_A^B \underline{\underline{J}}^A \left(\underline{\underline{C}}_A^B\right)^T - m\left(\underline{\underline{S}}_r^B\right)^2 = \underline{\underline{C}}_A^B\left(\underline{\underline{J}}^A - m\left(\underline{\underline{S}}_r^A\right)^2\right)\left(\underline{\underline{C}}_A^B\right)^T \tag{4.20}$$

where

- $\underline{\underline{C}}_A^B$ is the rotation matrix from reference frame A to B;
- $\underline{\underline{S}}_r^A$ is the skew symmetric matrix of the vector from the origin of reference frame A to the one of B written in coordinates of A; $\underline{\underline{S}}_r^B$ is the same matrix but written in coordinates of B;
- m is the mass of the piece.

4.2.3 Multiple-element surface approach

To achieve a high precision in the computation of the external forces acting on the deorbiting system, a numerical approach has been adopted. The satellite and the sail surfaces were divided into smaller elements and the force on each segment was calculated. Knowing the position of each element respect to the centre of mass of

the corresponding object, also the torque contribution of those have been evaluated. Those single contributions were then summed to obtain the total force and torque acting on the system.

Each object has been, therefore, divided in small segments identified by the coordinates of 4 vertexes and a center respect to origin of the body frame. In this way it has been possible to define also the normal to each single element, positive outward, and the respective area.

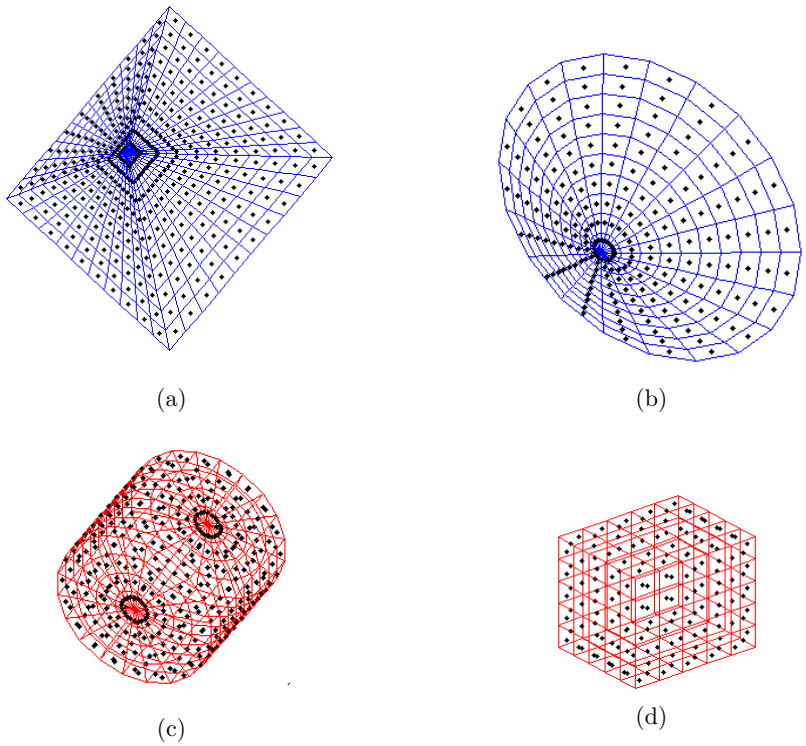

(a) (b) (c) (d)

Table 4.1: Multi-element surface models – (a) Pyramidal sail, (b) Conic sail, (c) Cylinderical satellite, (d) Cuboid-shaped satellite

A tighter mesh results in a more precise results but it also slows down the computation.

A multiple-elements approach allows also the study of shielded areas; these are the parts of the satellite or the sail which are not exposed to the incoming air flow or photon stream, situation which can occur due to *self-shielding* or *inter-shielding*. The occluded elements experience zero aerodynamic or solar force, hence they do not contribute to the calculation of the total external disturbance.

4.2.3.1 Self-shielding

This phenomenon occurs when, due to the object attitude, a portion of its surface is shielded from the light/air flow by the remaining of the body.

For sake of simplicity, in this description, the elements occluded from direct air flow/ light stream will be referred to both as 'shielded' and 'shaded' because, even if the nature of the incoming particles is completely different, the analytical process to identify the occluded parts is the same.

In the satellite case, no matter the shape, the identification of the shielded elements is performed simply comparing the normal vector of each segment with the vector of the incoming particles: if the component of the surface element normal along the incoming light/flow vector is greater than or equal to zero, than the segment is shielded, otherwise is expose to the light/flow.

For the sail, instead, other two possible situations need to be taken in account. Indeed, as Figure 4.6 shows, depending on the angle of attack/to the Sun, the sail could experience:

- The entire external surface of the sail is exposed to the light/flow. This condition exists whilst the angle of attack/to the Sun is less than $\frac{\pi}{2} - \Omega$;
- Part of the external surface of the cone is exposed to the light/flow. This condition exists whilst the angle of attack/to the Sun is greater than $\frac{\pi}{2} - \Omega$ but less than $\frac{\pi}{2}$;
- The light/flow impinges on both the internal and external surfaces of the cone, for angle of attack/to the Sun greater than $\frac{\pi}{2}$ and lower than $\frac{\pi}{2} + \Omega$;
- Complete internal impingement, for angle of attack/to the Sun greater than $\frac{\pi}{2} + \Omega$.

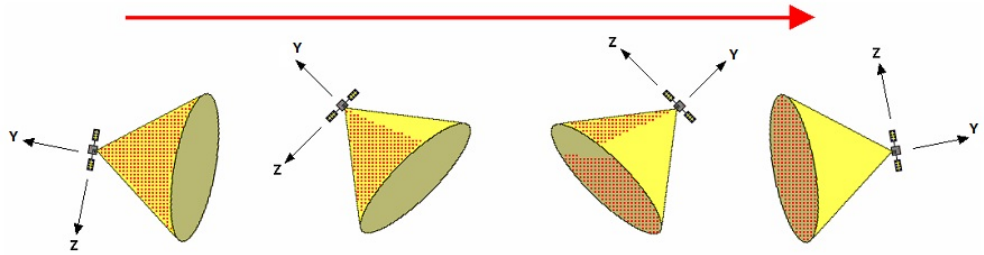

Figure 4.6: Migration of the impingement zones with changing angle of attack [15]

The identification of the segments in light or shade on the external surface is immediate and equal to the process adopted for the satellite. Afterwards, studying exclusively the segments which are externally occluded, the recognition of the internal impingement zones is obtained with the following procedure:

A vector parallel to the flow anti-direction is extended from the center of each segment to the sail base plane. The projection is done

$$P\{c_i\} = \mathrm{c}_i - \underline{\hat{v}}_\infty k \ , \qquad \mathrm{k} \geq 0 \tag{4.21}$$

Where k is easily computed knowing the distance of c_i to the base plane.

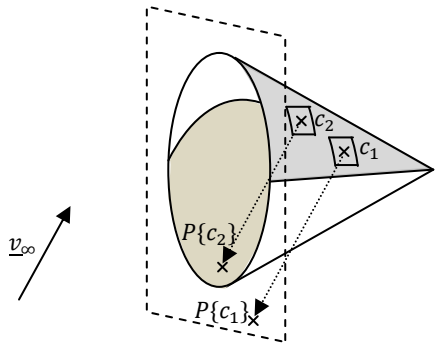

Figure 4.7: Determination of shade on the inner side. Projection of segment centers in the sail base plane

If $P\{c_i\}$ lies inside the sail base polygon/circle then the surface element of c_i is lid (or exposed to the flow) from the inside of the sail. In such case, the surface normal unit vector used for the computation of the force assumes the opposite sign.

This analytical procedure is repeated both for the wind flow and for the solar light for the computation of aerodynamic and solar forces/torques.

4.2.3.2 Inter-shielding

Having a satellite-sail configuration, it is natural that one body partially or totally occludes the other one. This phenomenon changes the aerodynamic/solar force acting on the shielded body and thus should be considered.

The algorithm used to compute the inter-shielding performs the following tasks:

- Computes the self-shielding for each of the two bodies as described in the previous section;
- Isolates the coordinates of the edges of the illuminated (or exposed to the flow) faces of the satellite;
- Projects those edges in the sail base plane in the direction of the flow/light (Figure 4.8); if the projection constants k_i are positive, the sail is potentially shielded by the satellite, if they are negative, then the satellite is potentially shielded by the sail; if the flow/light direction is parallel to the sail base plane, no inter-shielding occurs;
- In order to obtain the sail projection on its own base plane (along the flow/light direction), it checks for two distinct cases:
- the outer surface of the sail is completely lid (or in flow) or completely self-shielded, in which case the sail projection is simply its base polygon/circle;
- the outer surface of the sail has both illuminated (or in flow) and self-shielded areas, which means that the sail projection in the base plane includes projected tip (Figure 4.9). To determine contour of such projection (sail base polygon + projected tip) a convex hull algorithm is used.

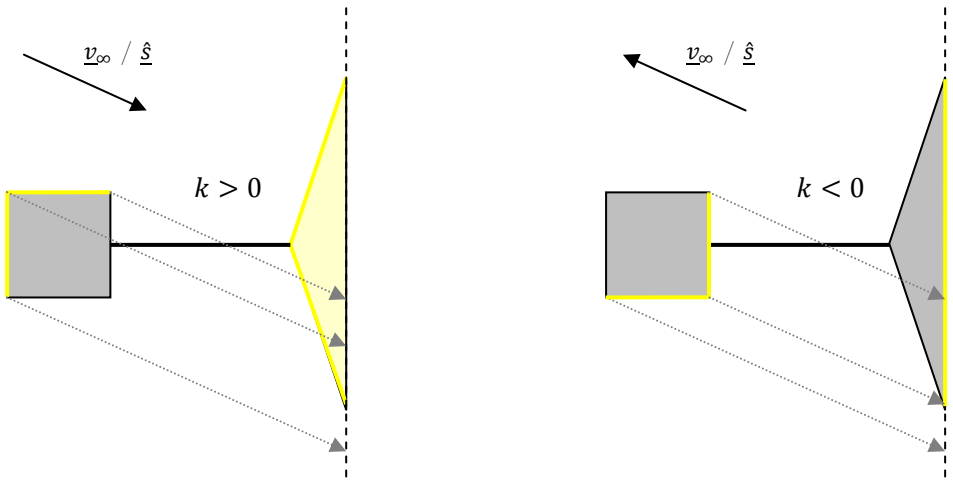

Figure 4.8: Projection of satellite illuminated edges onto sail base plane in case of: satellite ahead of sail (left) and the opposite (right)

- With the contour of the projections of both satellite and sail it checks for intersections of the two (no intersections means that none of the objects casts a shadow on the other).
- In case of intersection (Figure 4.10):
- if the satellite is ahead of the sail with respect to the flow/light direction ($k_i > 0$), the algorithm determines which sail surface element centroids lie inside the projected satellite contour. Those that do are effectively shielded by the satellite;
- if instead the sail is ahead of the satellite ($k_i < 0$), it determines which satellite surface element centroids (belonging to the illuminated faces) lie inside the sail projected contour. The ones that do are shielded by the sail.
- The initial self-shielding information is updated with the inter-shielding one.

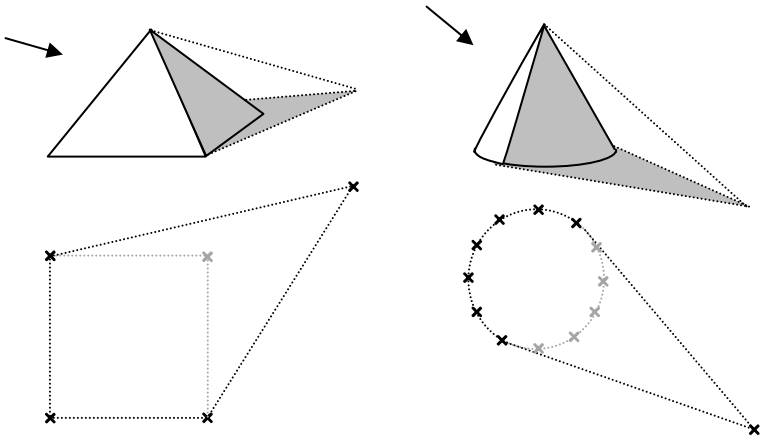

Figure 4.9: Sail projection onto its own base plane for outer surface simultaneously lid and shaded

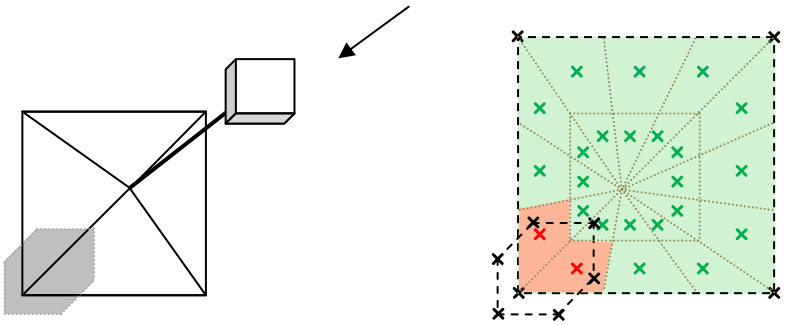

Figure 4.10: Contour intersection check and determination of circumscribed centroids of the shaded body

4.2.4 Equations of motion

The 6 DoF simulator considers also the attitude of the deorbiting system, hence both the linear and rotational dynamics are propagated.

The integration method used is ode45, which is based on an explicit Runge-Kutta (4,5) formula, the Dormand-Prince pair, available in Simulink.

4.2.4.1 Linear dynamics

The linear dynamics propagation is equal to what has been already described in Section 4.1.2.

4.2.4.2 Rotational dynamics

In a rigid-body, the sum of all applied moments $\underline{T}$ equals the time derivative of the angular momentum about the centre of mass with respect to the inertial reference frame I [**33**].

$$\frac{{}^{I}d}{d}\underline{H} = \underline{T} \tag{4.22}$$

where the total angular momentum $\underline{H}$ about the centre of mass of the rigid-body is given by

$$\underline{H} = \underline{\underline{J}}\,\underline{\omega}^{B} \tag{4.23}$$

To simplify the notation, from here on the angular velocity vector in body frame reference will be expressed simply with $\underline{\omega}$. The moment of inertia matrix $\underline{\underline{J}}$ is defined on the system reference frame B.

The time derivative of the total angular moment therefore can be given with respect to B as

$$\begin{aligned}\underline{T} = \frac{^{I}d}{dt}\underline{H} &= \frac{^{B}d}{dt}\underline{H} + \underline{\omega}\times\underline{H} \\ &= \frac{^{B}d}{dt}(\underline{\underline{J}}\,\underline{\omega}) + \underline{\omega}\times\underline{\underline{J}}\,\underline{\omega} \\ &= \underline{\underline{J}}\,\dot{\underline{\omega}} + \underline{\underline{S_{\omega}}}\,\underline{\underline{J}}\,\underline{\omega}\end{aligned} \tag{4.24}$$

where $\underline{\underline{S_{\omega}}}$ is a skew symmetric matrix of $\underline{\omega}$.

For this research the total moment applied $\underline{T}$ can be split into several torque components as

$$\underline{T} = \underline{T}_{aero} + \underline{T}_{SRP} + \underline{T}_{G} \tag{4.25}$$

where $\underline{T}_{aero}$ is the aerodynamic torque, $\underline{T}_{SRP}$ is the solar torque and $\underline{T}_{G}$ is the gravity gradient torque.

The angular velocity of the body is obtained by integrating once the equation (4.24) and it serves as input for the calculation of the attitude, explained in the following paragraph.

4.2.4.3 Rotational kinematics

The attitude of the deorbiting system represents the orientation of the B frame with respect to the inertial one. In this research the attitude is expressed through the quaternions to avoid singularities during its propagation but, for a more intuitive visualization, also the Euler's angles representation are often used.

The quaternion expresses the attitude of the body with respect to the inertial frame and it is defined as:

$$\underline{q} = \begin{bmatrix} q_1 & q_2 & q_3 & q_4 \end{bmatrix}^T \tag{4.26}$$

where

$$\begin{aligned} q_1 &= e_1 \sin(\vartheta/2) \\ q_2 &= e_2 \sin(\vartheta/2) \\ q_3 &= e_3 \sin(\vartheta/2) \\ q_4 &= \cos(\vartheta/2) \end{aligned} \tag{4.27}$$

e_j represents the unit vector components around which the rotation ϑ takes place. As shown in (4.27), the convention used defines q_1, q_2 and q_3 as the vectorial components of the quaternion, while q_4 represents its scalar part. The relative direction cosine matrix is obtained as follows:

$$\underline{\underline{C}}(q) = \begin{bmatrix} q_1^2 - q_2^2 - q_3^2 + q_4^2 & 2(q_1q_2 + q_3q_4) & 2(q_1q_3 - q_2q_4) \\ 2(q_1q_2 - q_3q_4) & -q_1^2 + q_2^2 - q_3^2 + q_4^2 & 2(q_2q_3 + q_1q_4) \\ 2(q_1q_3 + q_2q_4) & 2(q_2q_3 - q_1q_4) & -q_1^2 - q_2^2 + q_3^2 + q_4^2 \end{bmatrix} \tag{4.28}$$

The matrix $\underline{\underline{C}}(q)$ is used to perform rotations of a generic vector $\underline{r}$ from *Inertial* to *Body* frame and *vice versa*.

$$\begin{aligned} \underline{r}^B &= \underline{\underline{C}} r^I \\ \underline{r}^I &= \underline{\underline{C}}^{-1} \underline{r}^I \end{aligned} \tag{4.29}$$

The attitude propagation is performed through the integration of

$$\begin{bmatrix} \dot{q}_1 \\ \dot{q}_2 \\ \dot{q}_3 \\ \dot{q}_4 \end{bmatrix} = \frac{1}{2} \begin{bmatrix} 0 & \omega_z & -\omega_y & \omega_x \\ -\omega_z & 0 & \omega_x & \omega_y \\ \omega_y & -\omega_x & 0 & \omega_z \\ -\omega_x & -\omega_y & -\omega_z & 0 \end{bmatrix} \begin{bmatrix} q_1 \\ q_2 \\ q_3 \\ q_4 \end{bmatrix} \tag{4.30}$$

where $\underline{\omega}$ is the angular velocity of the body frame respect to the inertial one.

In order to avoid numerical errors, a normalization of the quaternion is performed at each time step.

4.2.5 Perturbations

4.2.5.1 Gravity model

The gravity model implemented in the 6 DoF is the same of the one used in the low fidelity simulator, previously described in Section 4.1.4.1.

Moreover, dealing with a large structure, also the effect on the attitude has to be introduced through the evaluation of the gravity gradient. If we select a mass point dm of the orbiting body, the torque caused by the gravity gradient is given by

$$\underline{T}_G = \int_B \underline{d} \times \underline{G} \; dm \tag{4.31}$$

where $\underline{d}$ is the position of the point dm with respect to the centre of mass of the object [**35**]. Integrating for the entire body, the resulting gravity gradient torque across the object is expressed by

$$\underline{T}_G = \frac{3\mu}{|\underline{R}|^5} \underline{R} \times \underline{\underline{J}}\,\underline{R} \tag{4.32}$$

with R being the vector between the Earth centre and the CoM of the body and $\underline{\underline{J}}$ is its inertia matrix.

4.2.5.2 Aerodynamics model

In a 6 DoF simulator, off-velocity-direction components (lift) are also considered in the implemented aerodynamic model. Furthermore, as previously described in Chapter 3.3.3, material surface proprieties influence in the transferred momentum are also here considered.

As anticipated in Section 4.2.3, a multiple-elements approach has been adopted for the evaluation of the external forces acting on the body. The aerodynamic force on each segment of area dA is given by

$$d\underline{F}_{aero} = -\varrho \mid \underline{v}_{element} \mid^2 dA \cos\vartheta \left[\sigma_t \hat{\underline{v}}_{element} + \left(\sigma_n \left(\frac{v_b}{\mid \underline{v}_\infty \mid} \right) + \left(2 - \sigma_n - \sigma_t\right) \cos\vartheta \right) \underline{n} \right] \tag{4.33}$$

where

- ϱ is the local atmospheric density;
- dA is the element area;
- $\underline{v}_{element}$ is the element relative velocity with respect to the atmosphere;
- $\hat{\underline{v}}_{element}$ is the versor of $\underline{v}_{element}$;
- ϑ is the angle between $\underline{v}_{element}$ and the surface normal of the element;
- σ_t and σ_n are respectively the tangential and the normal accommodation coefficients;
- $\frac{v_b}{|\underline{v}_\infty|}$ is the ratio between the molecular exit velocity and the velocity of the incoming molecules with $\underline{v}_\infty = -\underline{v}_{rel}$.

The relative velocity of each element is equal to

$$\underline{v}_{elelement} = \underline{v}_{rel} + \underline{\omega}^I \times \underline{d}_{element} \tag{4.34}$$

where v_{rel} is the relative velocity of the object with respect to the atmosphere, ω^I is the angular velocity of the segment respect to the CoM of the object and $d_{element}$ is the shortest distance between the element and the rotation axis.

The aerodynamic torque generated by the force on a single element is then

$$d\underline{T}_{aero} = d\underline{F}_{aero} \times \underline{r}_{element} \tag{4.35}$$

where $r_{element}$ indicates the vector from the segment to the CoM of the object.

To obtain the resulting total aerodynamic force and torque, the single elements contribution is integrated over the surface.

$$\begin{aligned} \underline{F}_{aero} &= \int_A d\underline{F}_{element} \\ \underline{T}_{aero} &= \int_A d\underline{T}_{element} \end{aligned} \tag{4.36}$$

As the (4.34) shows, the velocity of a segment with respect to the atmosphere is a function of the relative velocity of the object (also with respect to atmosphere) and the velocity of the surface segment with respect to the body CoM. These contributions generate two different kinds of torque: the restoring torque and the damping torque. The restoring torque will tend to rotate the object in order to make it align with the velocity vector and therefore this contribution is stronger at higher angles of attack. The damping torque can be observed when the object is

subjected to a pure rotational movement and it will generate a counteracting rotation that increases with the angular rate. The expressions of these two torque contributions per segment, deduced in Appendix B, are

$$\begin{aligned} d\underline{T}_{rest} \approx \; & r_{element} \times \Big[\varrho dA \sigma_t \left(\underline{v}_{rel} \cdot \underline{n} \right) \underline{v}_{rel} + \varrho dA \sigma_n v_{b\infty} \left| \underline{v}_{rel} \right| \left(\underline{v}_{rel} \cdot \underline{n} \right) \underline{n} \\ & + \varrho dA \left(2 - \sigma_t - \sigma_n \right) \left(\underline{v}_{rel} \cdot \underline{n} \right)^2 \underline{n} \Big] \end{aligned} \tag{4.37}$$

$$\begin{aligned} d\underline{T}_{damp} \approx \; & r_{element} \times \Big[\varrho dA \sigma_t \left[\left(\underline{v}_{\omega} \cdot \underline{n} \right) \underline{v}_{rel} + \left(\underline{v}_{rel} \cdot \underline{n} \right) \underline{v}_{\omega} \right] + \varrho dA \sigma_n v_{b\infty} \left| \underline{v}_{rel} \right| \left(\underline{v}_{\omega} \cdot \underline{n} \right) \underline{n} \\ & + \varrho dA \left(2 - \sigma_t - \sigma_n \right) 2 \left(\underline{v}_{rel} \cdot \underline{n} \right) \left(\underline{v}_{\omega} \cdot \underline{n} \right) \underline{n} \Big] \end{aligned} \tag{4.38}$$

The total restoring and damping torques are then

$$\underline{T}_{rest} = \int_A d\underline{T}_{rest} \tag{4.39}$$

$$\underline{T}_{damp} = \int_A d\underline{T}_{damp} \tag{4.40}$$

4.2.5.3 SRP model

The high fidelity SRP model implemented in the 6 DoF simulator allows a better definition of the contributions of the object's optical proprieties with respect to the 3 DoF one.

The solar force is calculated in a multi-surface-element in which the contribution of each segment is

$$dF_{solar} = (1 - \tau) P dA \left(-\underline{s} \cdot \underline{n} \right) \left\{ \left(1 - \varrho_s \right) \underline{s} - \left[2 \varrho_s \left(\underline{s} \cdot \underline{n} \right) + \frac{2}{3} \varrho_d \right] \underline{n} \right\} \tag{4.41}$$

where

- $P = 4.563 \; x \; 10^{-6} \; N / m^2$ is the nominal solar radiation pressure constant at 1 AU from the sun;
- dA is the area of the single segment subjected to the photons stream;
- $\underline{n}$ is the normal to the surface;
- $\underline{s}$ is the unit vector directed from the Sun to the surface.
- τ is the transmitted fraction of incoming photons, i.e. those that do not interact with the surface.

The solar torque on the segment is

$$d\underline{T}_{solar} = d\underline{F}_{solar} \times \underline{r}_{element} \tag{4.42}$$

where $r_{element}$ is the vector from the segment to the CoM of the object.

The total solar force and torque are the integration of the single elements contribution over the surface.

$$\begin{aligned} \underline{F}_{solar} &= \int_A d\underline{F}_{element} \\ \underline{T}_{solar} &= \int_A d\underline{T}_{element} \end{aligned} \tag{4.43}$$

The distinction between solar restoring and damping torque components is not carried out because appreciable damping torques cannot be created by the SRP. The small effect that is present is in any event generated by a totally different mechanism associated with changes in the wavelength of reflected photons [**15**]. For its magnitude it has been neglected.

The eclipse phenomenon is taken into account in this model.

4.2.6 Quotients

In order to ease the use of the solar and aerodynamic forces and torques in the dynamic simulations and validation, the components of these actions are divided by appropriate quantities creating the respective quotients.

Aerodynamic force quotient

The aerodynamic force quotient $\underline{Q}_{aF}$ is obtained by dividing the aerodynamic force by $\varrho\left|\underline{v}_\infty\right|^2$, therefore

$$\underline{F}_{aero} = \varrho\left|\underline{v}_\infty\right|^2 \underline{Q}_{aF} \tag{4.44}$$

Aerodynamic torque quotients

The aerodynamic torque quotients $\underline{Q}_{aTR}$ and $\underline{Q}_{aTD}$ are obtained by dividing the aerodynamic restoring torque and damping torque respectively by $\varrho\left|\underline{v}_\infty\right|^2$ and $\varrho\left|\underline{v}_\infty\right|\left|\underline{\omega}\right|$, therefore

$$\underline{T}_{aero} = \varrho\left|\underline{v}_\infty\right|^2 \underline{Q}_{aTR} + \varrho\left|\underline{v}_\infty\right|\left|\underline{\omega}\right| \underline{Q}_{aTD} \tag{4.45}$$

Solar force quotient

The solar force quotient $\underline{Q}_{sF}$ is obtained by dividing the solar force by P, therefore

$$\underline{F}_{SRP} = P\underline{Q}_{sF} \tag{4.46}$$

Solar torque quotient

The solar torque quotient $\underline{Q}_{sT}$ is obtained by dividing the solar force by P, therefore

$$\underline{T}_{SRP} = PQ_{sT} \tag{4.47}$$

All these quotients are vectorial entities

$$\underline{Q}_{aF} = \begin{bmatrix} Q_{aFx} \\ Q_{aFy} \\ Q_{aFz} \end{bmatrix}, \quad \underline{Q}_{aTR} = \begin{bmatrix} Q_{aTRx} \\ Q_{aTRy} \\ Q_{aTRz} \end{bmatrix}, \quad \underline{Q}_{aTD} = \begin{bmatrix} Q_{aTDx} \\ Q_{aTDy} \\ Q_{aTDz} \end{bmatrix}, \quad \underline{Q}_{sF} = \begin{bmatrix} Q_{sFx} \\ Q_{sFy} \\ Q_{sFz} \end{bmatrix}, \quad \underline{Q}_{sT} = \begin{bmatrix} Q_{sTx} \\ Q_{sTy} \\ Q_{sTz} \end{bmatrix}$$

(4.48)

4.2.6.1 Quotients computation validation

To validate the force and torque computation method, a confrontation with the aerodynamic quotients for a conic sail reported on [**15**] is performed. This study is based on a conical sail of 10 m^2 of base area and variable apex half-angles.

For validation purposes, the aerodynamic force is divided in two components: *Drag* and *Lift*. The definitions of these contributions in [**15**] is done differently from the most commonly adopted In particular, the drag force represents the aerodynamic force component along the y axis in the body frame, and the lift is the norm of the aerodynamic force component in the $x-z$ plane. The expression of these is:

$$F_{aDrag} = \underline{F}_{aero} \cdot \underline{\hat{y}} \tag{4.49}$$

$$F_{aLift} = \sqrt{\left(\underline{F}_{aero} \cdot \underline{\hat{x}}\right)^2 + \left(\underline{F}_{aero} \cdot \underline{\hat{z}}\right)^2} \tag{4.50}$$

Where $\underline{\hat{x}}, \underline{\hat{y}}, \underline{\hat{z}}$ are the unit vector aligned with the respective system Body frame axis.

The aerodynamic force and torque quotients computation is then consistent with what already mentioned in the previous paragraphs.

The results of the quotients comparisons are shown in Figure 4.11.

It can be noticed that the results match the reference case quite accurately. The main differences can be attributed to numerical errors, inevitable in a multi-finite-elements integration, but absent in the analytical solution chosen by [**15**]. Despite these minor differences, the overall behaviour indicates a correct force and torque evaluation, thus the implemented computation method can be considered validated.

4.2.6.2 Quotients mapping and lookup

The computation of the aerodynamic and solar forces and moments are done in a numeric integration fashion that covers all the surface elements defined for the sail/satellite. This process grows in required time and computational effort with the number of elements of the surface discretisation, quickly reaching impractical levels. A simple, yet powerful way of having an accurate discretisation of the surface and still be able to simulate the system orbital and attitude behaviour for reasonably long periods, is to is to rely on looked-up quotients for the computation of forces/torques during simulation. These quotients are mapped against azimuth and elevation angles to cover the entire sphere of possible incident wind/light directions.

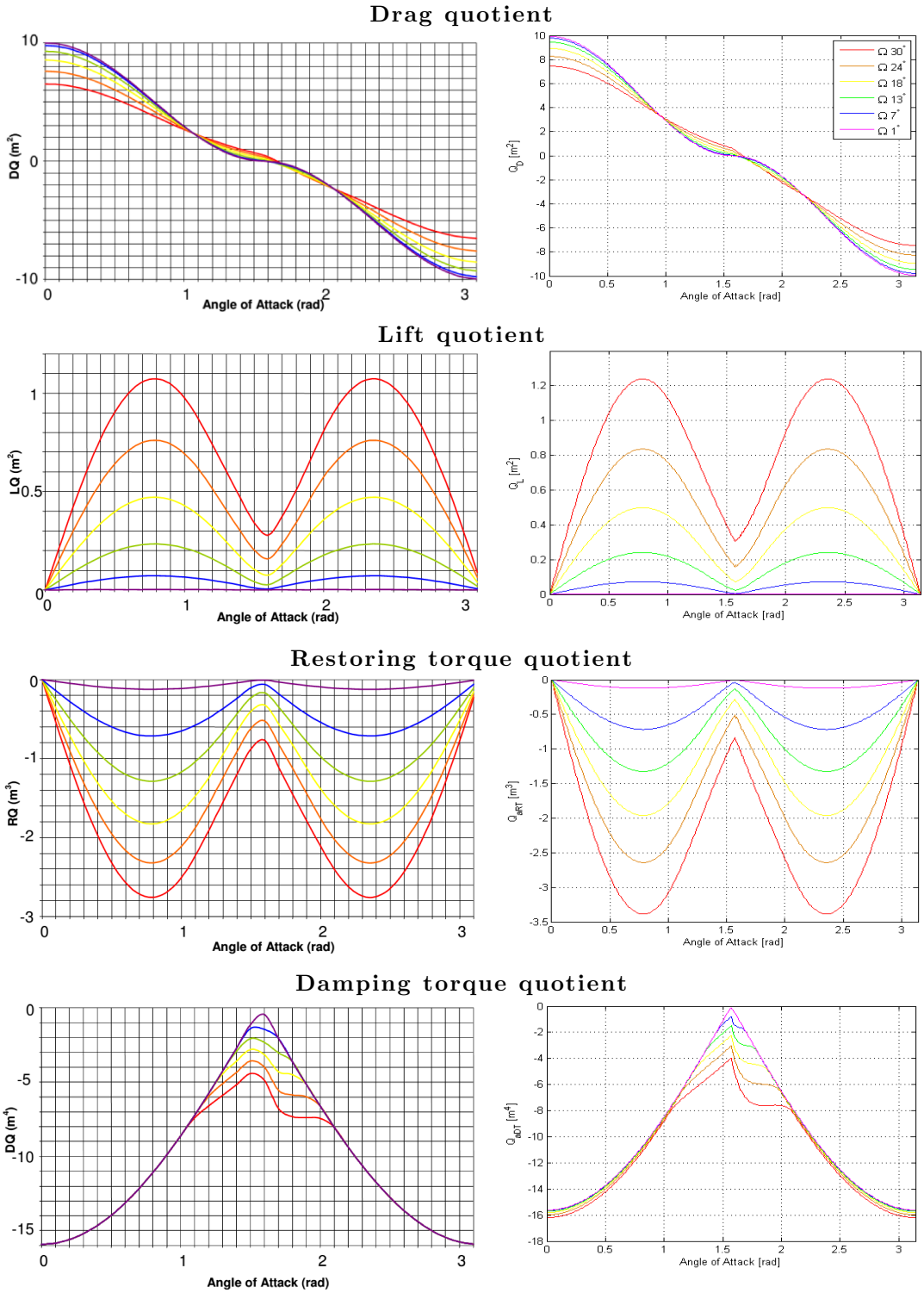

Figure 4.11: Aerodynamic quotients comparison

The aerodynamic damping quotient Q_{aTD} depends on the system angular velocity direction so, instead of three, it is split into nine scalar quotients

$$\underline{Q}_{aTD} = \frac{\partial \underline{Q}_{aTD}}{\partial \underline{\omega}} \frac{\underline{\omega}}{|\omega|} = \frac{1}{|\omega|} \begin{bmatrix} \frac{\partial Q_{Dx}}{\partial \omega_x} & \frac{\partial Q_{Dx}}{\partial \omega_y} & \frac{\partial Q_{Dx}}{\partial \omega_z} \\ \frac{\partial Q_{Dy}}{\partial \omega_x} & \frac{\partial Q_{Dy}}{\partial \omega_y} & \frac{\partial Q_{Dy}}{\partial \omega_z} \\ \frac{\partial Q_{Dz}}{\partial \omega_x} & \frac{\partial Q_{Dz}}{\partial \omega_y} & \frac{\partial Q_{Dz}}{\partial \omega_z} \end{bmatrix} \begin{bmatrix} \omega_x \\ \omega_y \\ \omega_z \end{bmatrix} \tag{4.51}$$

The total damping torque is then

$$T_{aeroD} = \varrho |\underline{v}_\infty| |\underline{\omega}| \underline{Q}_{aTD} = \varrho |\underline{v}_\infty| \frac{\partial \underline{Q}_{aTD}}{\partial \underline{\omega}} \underline{\omega} \tag{4.52}$$

If both the velocity of the incoming atmosphere particles and the incident Sun light vector are written in the system Body frame as

$$\underline{v}_\infty^B = |\underline{v}_\infty| \begin{bmatrix} \cos(\Phi_a)\sin(\vartheta_a) \\ \cos(\Phi_a)\sin(\vartheta_a) \\ \sin(\Phi_a) \end{bmatrix} \tag{4.53}$$

$$s^B = \begin{bmatrix} \cos(\Phi_s)\sin(\vartheta_s) \\ \cos(\Phi_s)\sin(\vartheta_s) \\ \sin(\Phi_s) \end{bmatrix} \tag{4.54}$$

with

$$\begin{cases} \vartheta_a \in [0, 360] \text{deg} \\ \Phi_a \in [-90, 90] \text{deg} \end{cases} \tag{4.55}$$

$$\begin{cases} \vartheta_s \in [0, 360] \text{deg} \\ \Phi_s \in [-90, 90] \text{deg} \end{cases} \tag{4.56}$$

Eventually, the quotients $\underline{Q}_{aF}$, $\underline{Q}_{aTR}$, $\frac{\partial \underline{Q}_{aTD}}{\partial \underline{\omega}}$, $\underline{Q}_{sF}$, $\underline{Q}_{sT}$ can be simply computed for a mesh covering the ranges of ϑ_a , ϑ_s and Φ_a , Φ_s. The result is a set of 21 tables that can be used through 2D interpolation during a time-simulation.

4.3 6 DoF with Flexibility

4.3.1 Simulator description and diagram

The assumption of rigid bodies used so far is a realistic approximation for satellites with no appendages or deployable structures attached. However, when also long telescopic mast, appendages, thin sails, etc. are studied, an accurate research would require a study on the flexibility of those structures. Within this thesis the influence of a flexible mast on the overall system is investigated using a lumped parameter

approach. The overall system under analysis is modelled as two rigid bodies representing the satellite and the sail, connected by a flexible beam.

The conceptual design of the 6 DoF with flexibility simulator is shown in Figure 4.12, and a more detailed view of the flexible dynamics is instead reported in Figure 4.13. The state vector $\underline{x}$ now represents the union of the three state vectors, one for each modelled body, and containing its velocity, position, angular velocity and attitude.

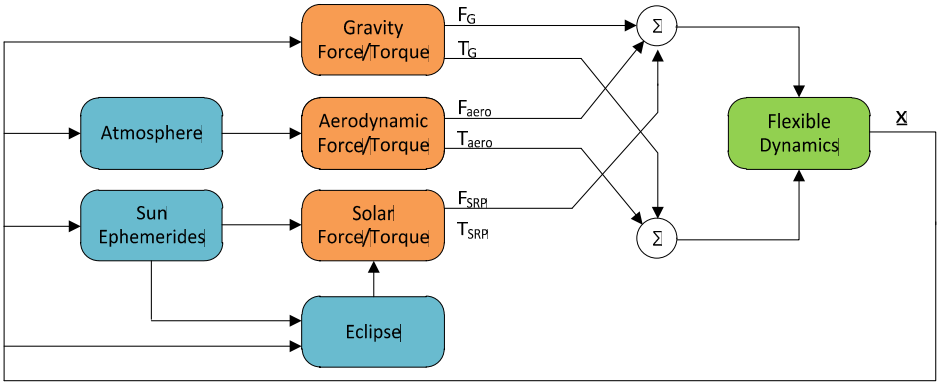

Figure 4.12: 6 DoF with flexibility simulator diagram

The validation tests done to this simulator can be found in Appendix A.3, together with the complete list of input variables this tool uses.

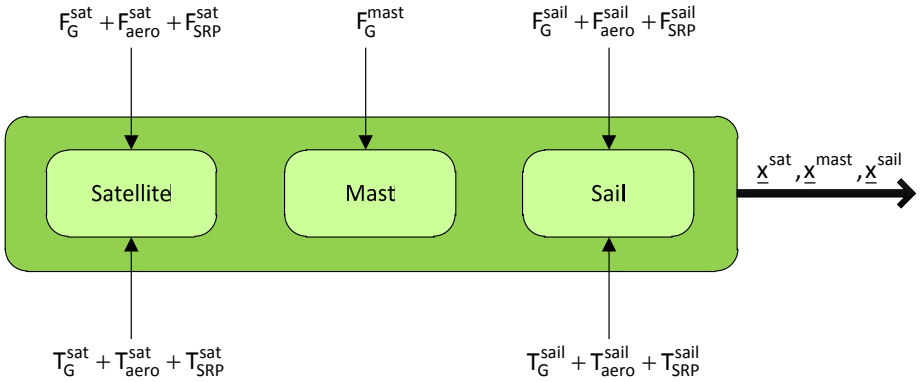

Figure 4.13: Detail of flexible dynamics

4.3.2 Lumped parameter method

The lumped-parameter method approximates a flexible body as a set of rigid bodies coupled with springs and dampers **[36]**. The spring stiffness coefficients and damping coefficients are functions of the material proprieties and geometry of the flexible member under consideration. This method is especially suited for linear structures, such as beams, in which each fundamental flexible elements is couple to two other in a simple chain.

The lumped-parameter method discretizes the beam of length L into identical generalized beam elements (GBEs), each of length $l = L / n$ and mass $m = M / n$. By making the GBEs identical, the flexibility proprieties of the beam are assumed uniform along its length. Each of the n elements consists on a body-joint-body combination, where the joints are chosen according to the flexible degrees of freedom to be modeled. The beam is obtained by welding together adjacent GBEs in a chain, as shown in Figure 4.14.

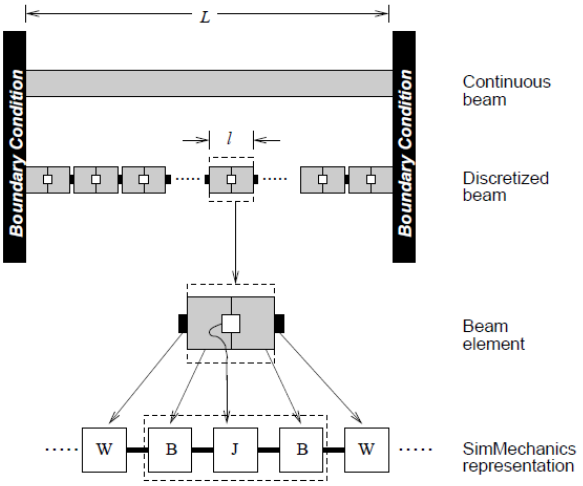

Figure 4.14: Lumped-parameter discretisation of a beam: welds (W), bodies (B), and joints (J) [36]

The material proprieties define the spring elastic constant and the damping coefficient applied to the joint.

Joints

The beam theory will not be exposed in this thesis but a brief recapitulation of the necessary relations is reported in this section.

The viscoelastic constrain, in general, acts along the three displacement directions, for the bending movements, and torsion.

In order to estimate the spring constants associated with extension (K_i^y), bending ($K_i^{\Phi_j}$) and torsion (K_i^{ϑ}) of the i element, the relative stiffness EA, EI_{jj} and GJ are required. E is the Young's elastic modulus, G is the shear modulus, A is the cross-section area, I_{jj} is the area moment of inertia normal to the direction of bending jj and J is the polar moment of inertia [**37**].

Extensional spring constant along y

$$K_i^y = \frac{EA}{l} \tag{4.57}$$

Bending spring constant around x

$$K_i^{\Phi x} = \frac{EI_{xx}}{l} \tag{4.58}$$

Bending spring constant around z

$$K_i^{\Phi z} = \frac{EI_{zz}}{l} \tag{4.59}$$

Torsional spring constant around y

$$K_i^{\vartheta} = \frac{EJ}{l} \tag{4.60}$$

where the proprieties of the beam are assumed to be constant along it.

The damping coefficients C_i, instead, do not have such a direct and analytical estimation process; they are usually evaluated experimentally. In this thesis, a conservative approach is assumed and the damping coefficient is set to 0. However, to avoid numerical instability issues, a low positive value is imposed for simulations.

4.3.3 SimMechanics™ dynamic model and integration

SimMechanics™ provides a multibody simulation environment for 3D mechanical systems. This framework has been used to implement the lumped-parameter method for the problem at hand. The flexible dynamics model developed in SimMechanics™ is then integrated in the simple 6 DoF simulator, substituting the rigid body dynamics block.

The integration method used is ode45, which is based on an explicit Runge-Kutta (4,5) formula, the Dormand-Prince pair, available in Simulink.

4.3.4 Geometry definition

Since the satellite and the sail are still assumed as rigid body, their definition is equal to what already stated in Section 4.2.2. The mast, instead, is described also through its material elastic proprieties, which are needed to compute the spring constant discussed in the previous section. Furthermore, also the number of GBE used to model the mast is now an input.

4.3.5 Perturbations

The external forces acting on the system are evaluated as expressed in Section 4.2.5, but now they are computed and applied separately for each body.

5 Analysis

5.1 Environment

In the previous chapters the main perturbations during the deorbit process have been introduced. Their role on the process itself, however, has not yet been addressed. This section analyses the atmosphere topography and how it compares to SRP for different altitudes, orbits and solar cycle stages. Furthermore, it analyses the deorbit time for different solar cycle moments.

5.1.1 Density profile

The atmospheric density is obviously dependant on the altitude but, as stated in Section 3.3.1, it is also highly influenced by the solar activity level. For a better understanding of the density topography in function of these parameters, the density maps were determined for different altitudes and two solar cycle stages. These maps are plot against latitude and solar hour.

Figure 5.1 shows the result of this study performed on the spring equinox of 1976 and 1982, corresponding respectively to a solar minimum and a solar maximum.

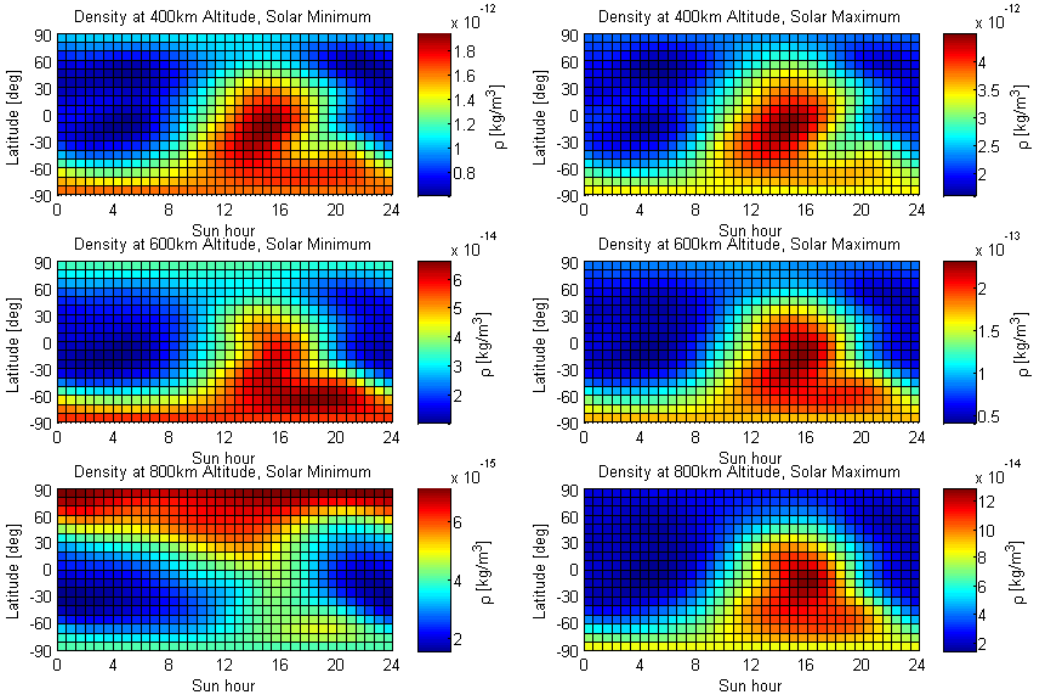

Figure 5.1: Atmospheric density in function of Sun hour, longitude and altitude, for different solar activity level

As expected, it is possible to notice the presence of the diurnal bulge, caused by the heated up and expanded low atmosphere, on equatorial latitude around 2 PM. This phenomenon is visible up to much higher altitudes during high solar activity.

Comparing the results for the same altitude, it is evident that to a solar maximum condition corresponds a higher density, again, due to the low atmosphere expansion. Furthermore, the density at the poles tends to be higher than at the equatorial areas not covered by the diurnal bulge, particularly at high altitudes. This is explained by the longer (even permanent) exposure of the polar high atmospheric layers to the solar radiation as compared to the equatorial ones that experience night. At higher altitudes the effect of the diurnal bulge is weaker, especially for low solar activity, being the highest densities measured at the poles.

5.1.2 Aerodynamic *vs* Solar force

An important factor to be evaluated regarding the LEO environment is the altitude threshold where the aerodynamic force acting on a deorbiting object, becomes dominant over the solar force (in a descending perspective). This point is dependent on the solar activity level, the altitude, the inclination of the orbit and its RAAN. It is clear that the SRP force is dominant at high altitudes, while the aerodynamic force has a stronger action at low altitudes. However, as the analysis on the previous section showed, the variability of the density profile can be quite considerable, completely changing the location of the defined threshold.

Following is reported the result of the altitude threshold analysis for a generic sail with $\Omega = 10°$ on an equatorial orbit, with zero RAAN; the aerodynamic an solar force have been calculated along one orbit and the average values for high and low solar activity conditions are showed in Figure 5.2.

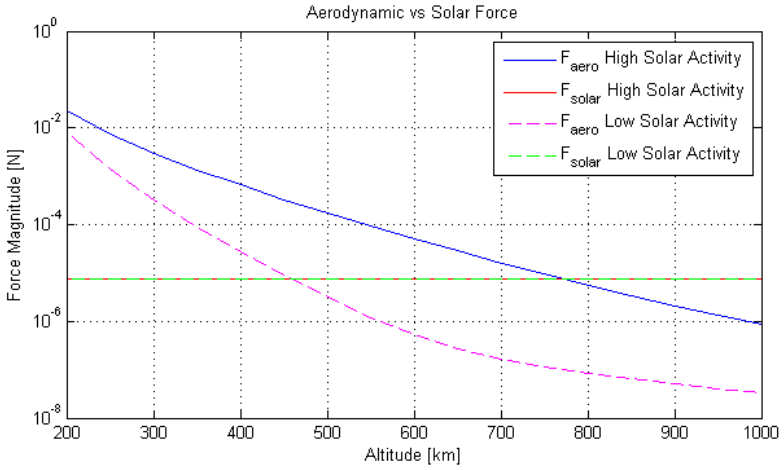

Figure 5.2: Aerodynamic and solar force comparison for different solar activity

The forces-transition point is clearly variable, passing from an altitude around 450 km in low solar condition, to almost 800 km during maximum solar activity. This effect has to be considered during the sail design procedure because it could lead to a big over- or under-estimation of the performances.

Figure 5.3, instead, shows the ratio between the average aerodynamic force and the average solar force magnitude over circular orbits, with three different altitudes at solar minimum and maximum.

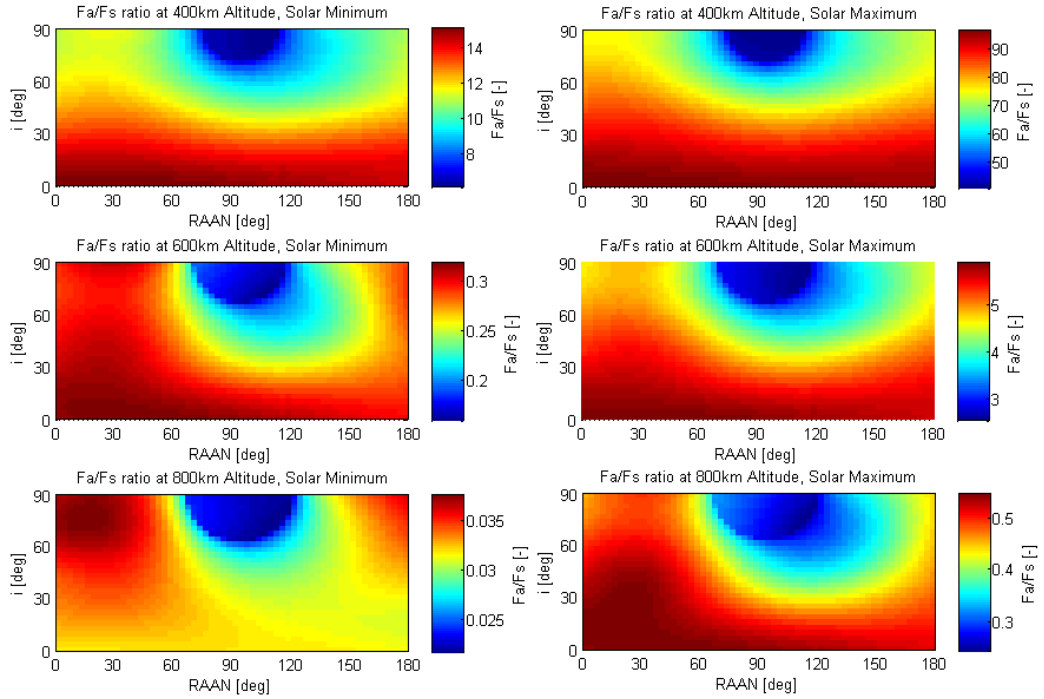

Figure 5.3: Aerodynamic/Solar force ratio against orbit inclination and RAAN, for three different altitudes, during maximum and minimum solar activity level

The resulting maps are plotted against inclination and RAAN. This analysis has been conducted with the 3 DoF simulator for an object with a ballistic coefficient $B_C = 100\ kg/\mathrm{m}^3$ and a reflectivity coefficient $C_R = 2$. The following points draw some considerations based on the results on Figure 5.3.

- As expected, the force ratio during the solar maximum, for all three altitudes, is higher than during solar minimum. This explained by the density increase related to the solar cycle.
- The altitude threshold for low solar activity is between 400 km and 600 km, while for high solar activity it is between 600 km and 800 km. This confirms the results obtained in Figure 5.2.
- The force ratio map at 600 km during low solar activity is very similar to the 800 km one for high solar activity. This is due to the fact that the aerodynamic force remains around considerable magnitudes up to higher altitudes. Again, this proves what already observed in the previous density graph.
- Generally the force ratio assumes higher values for low inclination orbits because on this orbital trajectory the spacecraft passes through the diurnal bulge, experiencing a higher aerodynamic force. This effect also explains the reason why some orbits with higher inclination and low RAAN show high ratio values as well.

- The constant presence of a low-ratio semicircle area for polar orbits with RAAN between 60° and 120° is due the absence of eclipse for these orbits. This leads to a maximisation of the in-light orbital path and, hence, to an increase of the solar force contribution (decrease of the force ratio).
- The map for solar minimum at 800 km of altitude shows a prevalence of high force ratio for polar orbits with low RAAN. This can be traced back to the higher density at the poles at high altitudes during solar minimum (Figure 5.1).
- The difference between the maximum and minimum values of the force ratio at each map is around 50% (of the maximum).

5.1.3 Solar cycle

As it has been previously seen, the solar activity highly influences the atmosphere density distribution. This, in turn, largely determines the decay of an orbiting object. Figure 5.4 shows the deorbiting time *versus* the initial epoch within an 11-year solar cycle for three different initial altitudes (circular equatorial orbits).

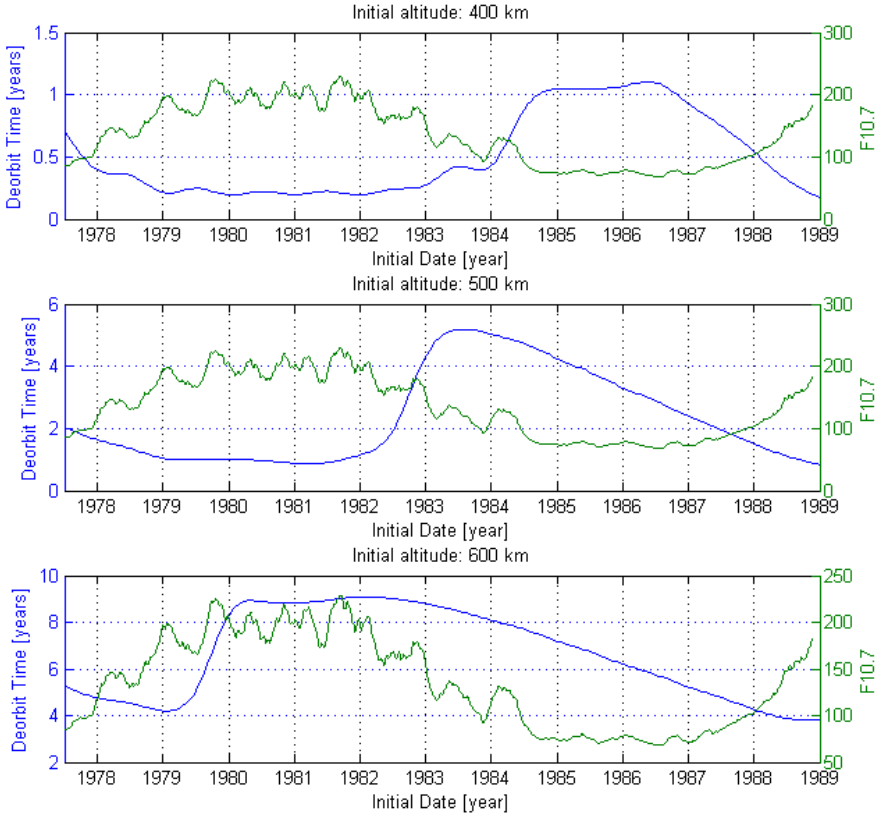

Figure 5.4: Deorbiting time for different altitudes during one solar cycle (11 years)

Naturally, the deorbiting time from higher orbits is greater. At low altitudes, the entire deorbit takes place within the solar stage in which it started (the maximum

deorbiting time recorded is of around 1 year). Furthermore, for lower orbits, the deorbiting time profile is almost in perfect counter-phase with the solar index, indicating that a deorbit beginning during a solar maximum has the minimum duration. Increasing the initial altitude, this effect is not visible anymore. Indeed, at 600 km the atmosphere is so rarefied that, even during solar maximum, the aerodynamic drag acting on the object is not strong enough to result in a deorbiting within the same solar stage. In these conditions, an object released during solar maximum will not completely decay during that same peak, thus being able to survive in orbit until the next solar maximum. An object released during solar minimum will also deorbit at the time of the next solar maximum. This causes a shift in the deorbiting time curve, being now the highest orbiting lifetimes for bodies released during the solar peak.

5.2 Sail system

5.2.1 Standard configuration

The design of the deorbiting system can be performed through the tuning of several parameters. In this analysis the design variables are limited to the following:

- Number of sail booms (sail base polygon);
- Ω sail vertex angle;
- Base area of the sail A ;
- Mast length L ;
- Optical proprieties of the sail.

The standard system baseline which has been maintained during the analysis (unless explicitly expressed) is:

	Parameter	**Value**
Sail	Material	CP-1 ($10\mu m$ thick)
	Mast attachment point	Sail tip
Boom	Material	CFRP
Mast	Material	Aluminum Al2024-T4
	Section shape	Hollow Square
	Section dimensions (h×w×t)	0.06m×0.06m×0.003m

Table 5.1: Deorbiting device fixed parameters

Moreover, the centers of mass of satellite, mast and sail are always assumed aligned along the negative Y axis of B1 reference frame.

The sail mass value used in the analysis follows the properties on Table 5.2 and depends on the selected area. Such mass value shall include also the CFRP booms mass and a 300g deployment mechanism.[**14**] The mast material proprieties used for mass and flexibility analysis are outlined on Table 5.4.

During the analysis the optical proprieties of the sail may change in function of the assumed coatings. This allows the study of the effect of this parameter within a range that covers both a totally reflective sail and a totally transparent one, without changing the base material. This shall be referred for each case.

CP-1	
Density	15.4 g/m^2
Solar transmittance	0.83
Solar absorbance	0.08
Solar reflectance	0.09

Table 5.2: CP-1 physical proprieties [16]

CFRP	
Density	15 g/m

Table 5.3: CFRP density [14]

Al2024-T4	
Density	2780 kg/m
Young's Modulus	73.1 GPa

Table 5.4: Aluminum Al2024 physical proprieties [38]

Along the analysis the satellite host considered can have different mass and dimension. This was selected as needed in function of the test objective. However, some characteristics have been preliminary set to a fixed value. Those are presented on Table 5.5.

Parameter	**Value**
Shape	Cube
Optical proprieties	Perfectly absorbent
Aerodynamic proprieties	Normal accommodation
Mast attachment point	$\begin{bmatrix} 0 & -\frac{l}{2} & 0 \end{bmatrix}$

Table 5.5: Generic satellite fixed parameters

l refers to the satellite side length.

A simple summarizing scheme of the standard assembled system configuration (satellite, mast and sail) with the tuning parameters analyzed during these studies is reported in Figure 5.5.

Some of the listed parameters have been analysed directly, while others, like the sail area, have been studied through their relation with different standard proprieties (e.g ballistic coefficient).

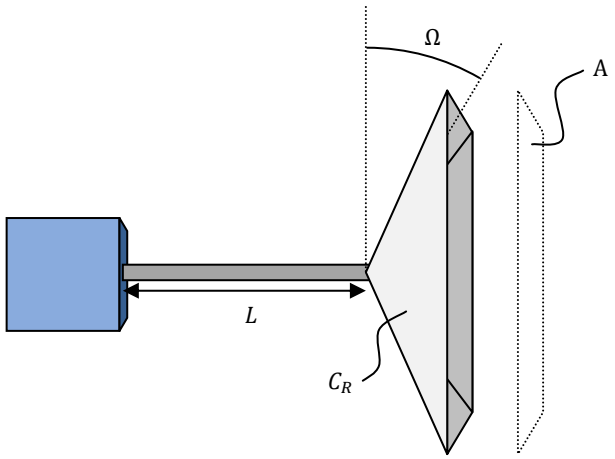

Figure 5.5: Standard deorbiting system configuration with tunable parameters

5.2.2 Ballistic coefficient

The ballistic coefficient, defined in Section 4.1.1, is a very important property for the deorbiting profile. Therefore it is fundamental to understand its relation with the deorbiting performances.

Figure 5.6 shows the deorbit time from circular equatorial orbits with different initial altitudes, for an object with various ballistic coefficients. The analysis has been performed with the 3 DoF simulator, both starting at solar maximum and minimum conditions.

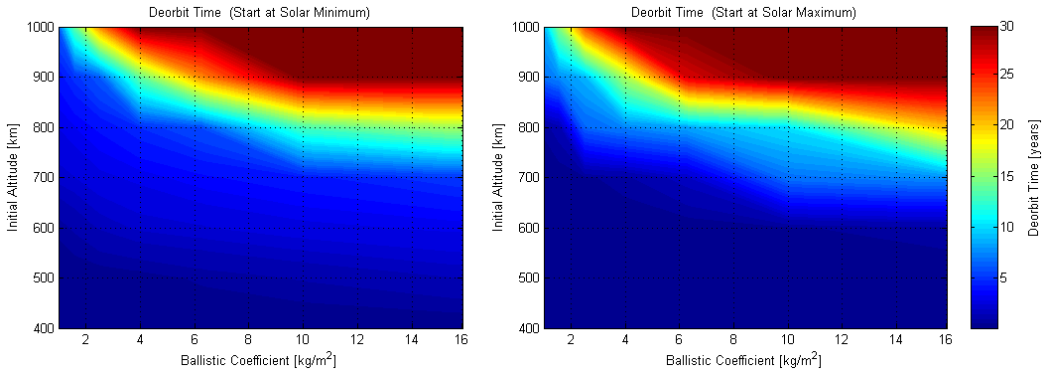

Figure 5.6: Deorbit time for different ballistic coefficient and initial altitudes

As already widely observed, to high initial altitudes corresponds a longer time to deorbit. Moreover, a greater ballistic coefficient leads, as well, to a higher deorbiting time. This means that, for the same host satellite, a larger sail decreases the necessary time to deorbit. In the same way, keeping constant the reference area of the object while decreasing its mass or increasing its C_D, contributes to a faster deorbiting.

Figure 5.6 shows that, for a deorbit that starts during a solar maximum condition, the short (less than 5 years) deorbiting time range is wider than in the solar minimum case. For increasing initial altitude, the difference between the two solar conditions results becomes smaller. Since the deorbit has to occur in less than 25 years, all simulations reaching 30 years were stopped.

The ballistic coefficient of the drag-sail deorbiting system can be preliminary approximated as

$$B_C = \frac{m_{sat}}{A_{sail} C_{D_{sail}}} \tag{5.1}$$

because the sail mass can be neglected compared to the satellite one, while the area and drag coefficient of the system are mainly defined by the sail contribution. Since the host satellite mass is not a design parameter, the main tuneable factors which are going to be analyzes, are the sail area and its drag coefficient.

5.2.3 Base polygon (number of booms)

The number of booms determines the shape of the sail base: a three-boom system is a triangular pyramid once deployed, a four-boom system results in a square pyramid, and so on. This choice is highly related to the achievable sail area and the robustness of the design [**15**].

Sail structural efficiency

With basic trigonometric relations it's possible to calculate the supported sail area given the length of deployable structure. Repeating this process for different apex half-angle ϑ, the results are shown Figure 5.7. This is an indication of the structural efficiency of different sails and it's evident that the three-boom configuration maximises this index.

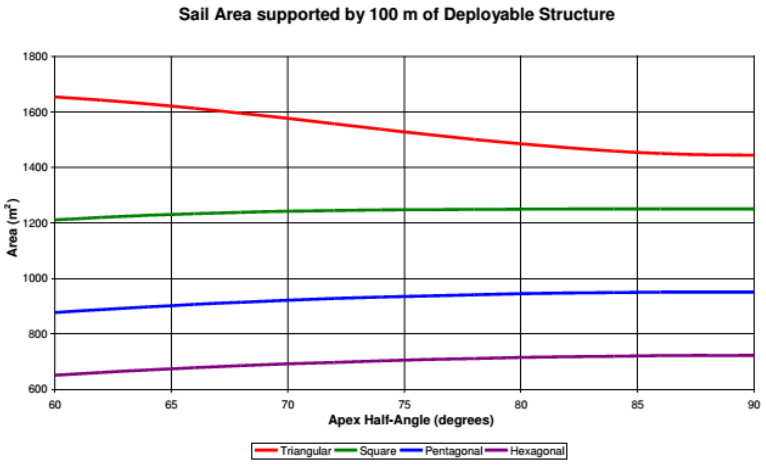

Figure 5.7: Supported sail area for different booms number

Design robustness

The robustness of a sail configuration is strictly connected to the efficiency reduction in case of boom deployment failure. It is immediate, then, to understand why a triangular sail is the least robust design: in case of failure of any one boom to deploy, the result will be a $\frac{2}{3}$ reduction of the effective drag sail area. Furthermore, the remaining $\frac{1}{3}$ of the total drag area would simply be a plane surface and therefore it could assume an attitude which produces zero drag.

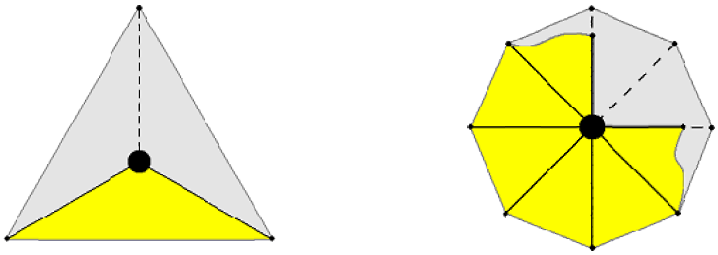

Figure 5.8: Consequence of boom deployment failure on a three-boom system (left) and on an eight boom system (right)

Considering, instead, a four-boom configuration, the loss in area in case of failure would be reduced to $\frac{1}{2}$ and the remaining portion would still provide a 3D shape, ensuring a minimum production of drag. However, the probability of failure in one or more booms would be increase of about 30%, assuming 99% of reliability of each boom.

With five or six boom, the efficiency losses in case of failure keep decreasing, but the probability of failure occurring increases instead. However, this trend reverses if seven or more booms are considered. This change is due to the fact that with seven or more booms, the failure of one would interfere with the deployment of the other ones around.

Trade-off

As described in the previous paragraphs, to maximise the structural efficiency, a three-boom system should be adopted, but in case of single boom failure, the resulting partially deployed sail could be unable to produce drag at all. On the other hand, increasing the number of booms to a maximum of six will augment the probability of failure in one or more booms. Hence, the optimum boom solution is represented by a four-boom sail and it is the configuration which will be maintained in the following analysis and design processes.

5.2.4 Force and torque quotients

In Section 4.2.6 the concept of quotient and its utility has been introduced. In this paragraph, the force and torque quotients for a system with a squared-base pyramid sail and a satellite point mass are reported. The system has the following characteristics on Table 5.6.

The aerodynamic and solar quotients are computed for different Ω angles. The aerodynamic force quotients here presented are expressed both as components of the Body axis and in the direction of the stream (drag and lift). Therefore, differently from what defined in Section 4.2.6.1, the drag and lift quotients represent the aerodynamic force components respectively along the velocity of the incoming flow and perpendicular to it. Figure 5.9 shows the force quotients for a flat square sail for different attitude angles while Figure 5.10 compares these quotients for different Ω and plots them along only one attitude angle.

Propriety	**Value**
Sail mass	1.2 kg
Sail area	30 m^2
Mast length	0.5 m
Sail optical proprieties	Typical solar sail
Sail aerodynamic proprieties	Typical solar sail

Table 5.6: Properties for a pyramidal sail input set

The aerodynamic force quotient in Z Body axis has not been included in Figure 5.10 because, for symmetry, it is identical to Q_x but with a variation along the Pitch angle. Observing the computed results it is possible to notice that the larger the Ω, the lower the maximum drag obtained when aligned with the flow, but the higher is the drag with side wind. In particular, the flat sail does not produce force along x and z for side wind, generating zero drag and lift.

The aerodynamic torque is calculated with respect to the extremity of the mast attached to the satellite because it is the actual moment transmitted to the spacecraft. Figure 5.11 presents the torque quotients for a flat square sail for different attitude angles. Figure 5.12, instead compares such quotients for different Ω plotting them along the Yaw angle.

From the computed quotients it is noticeable that the higher the Ω, the stronger the restoring and damping torques. Moreover, from the restoring torque plot it is possible to identify the two equilibrium points (four for the flat sail) for each sail shape: the stable equilibrium point at 0° and the unstable one at 180°. This means that a positive increment of Yaw angle from a null initial angle, the sail generates a negative torque re-establishing the initial condition, while from 180° the produced torque is positive and therefore driving the system away from the initial point. This confirms the intuitive *shuttlecock* stability of the configuration (satellite in front of the sail).

The restoring torque quotient around x-axis is equal to the one around z (Figure 5.12) but as function the Pitch angle, while around y axis there is no restoring torque. The damping torque around x axis is not plotted for being similar to the one around z axis.

The damping torque quotients show negative values for all the Ω, which means the damping component has always the opposite sign of the angular rotation of the body, acting as a break. This result is according to the expected.

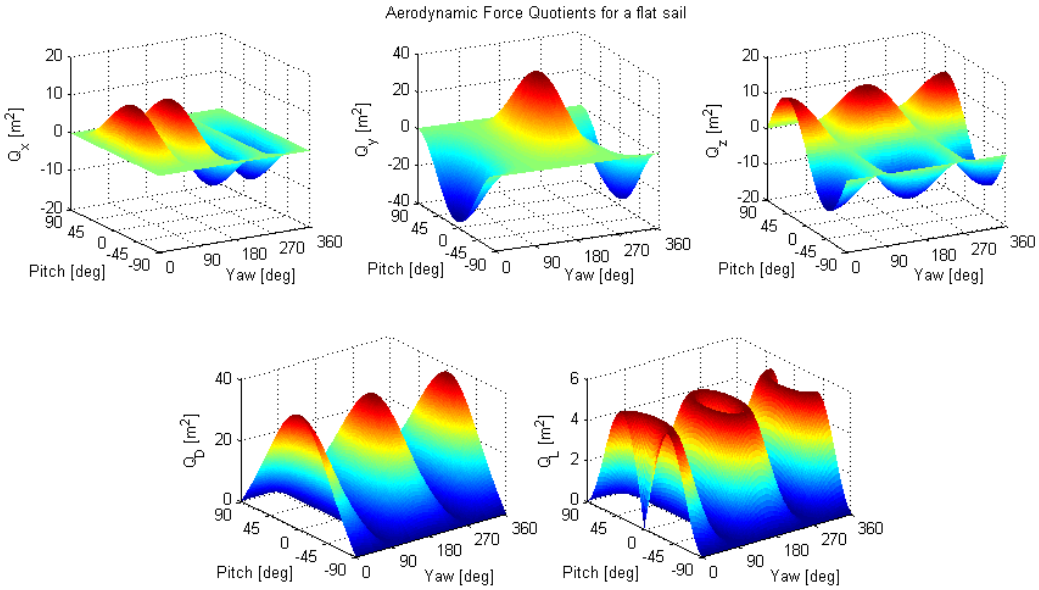

Figure 5.9: Aerodynamic Force Quotients for a flat square sail.

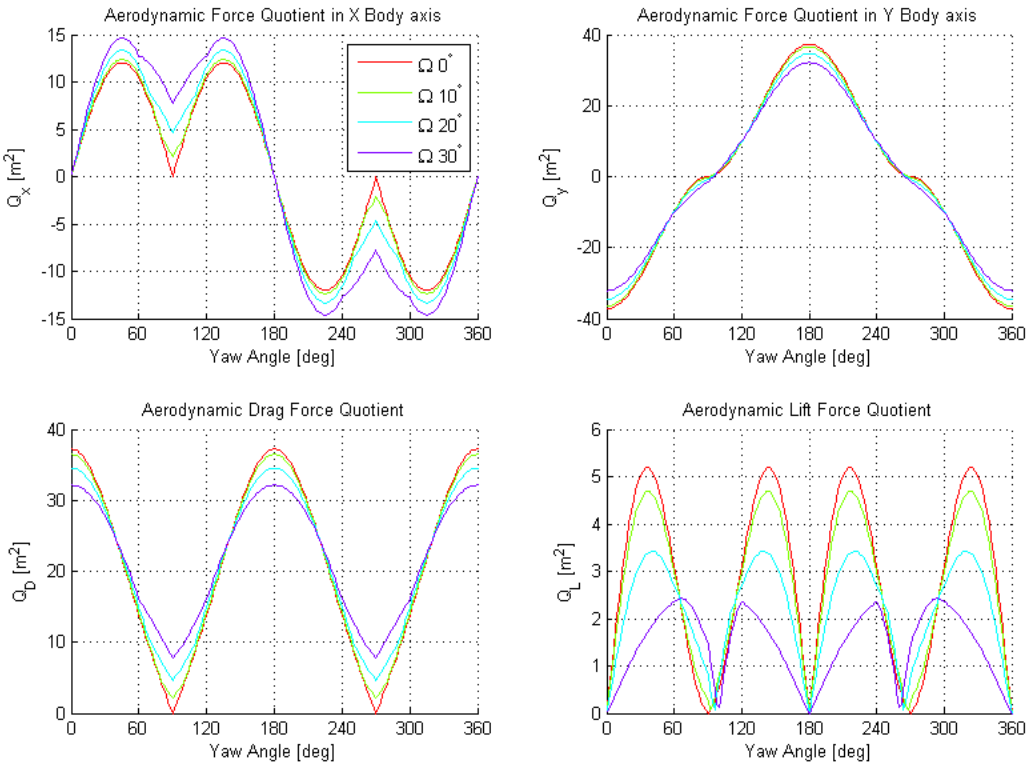

Figure 5.10: Aerodynamic force quotients for a pyramid sail with different Ω

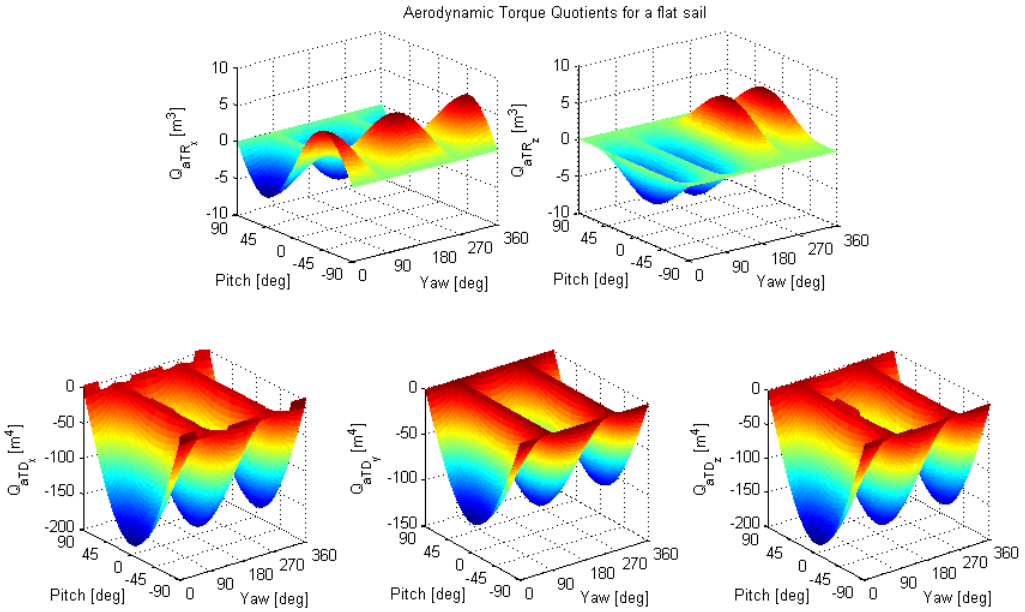

Figure 5.11: Aerodynamic Torque Quotients for a flat square sail.

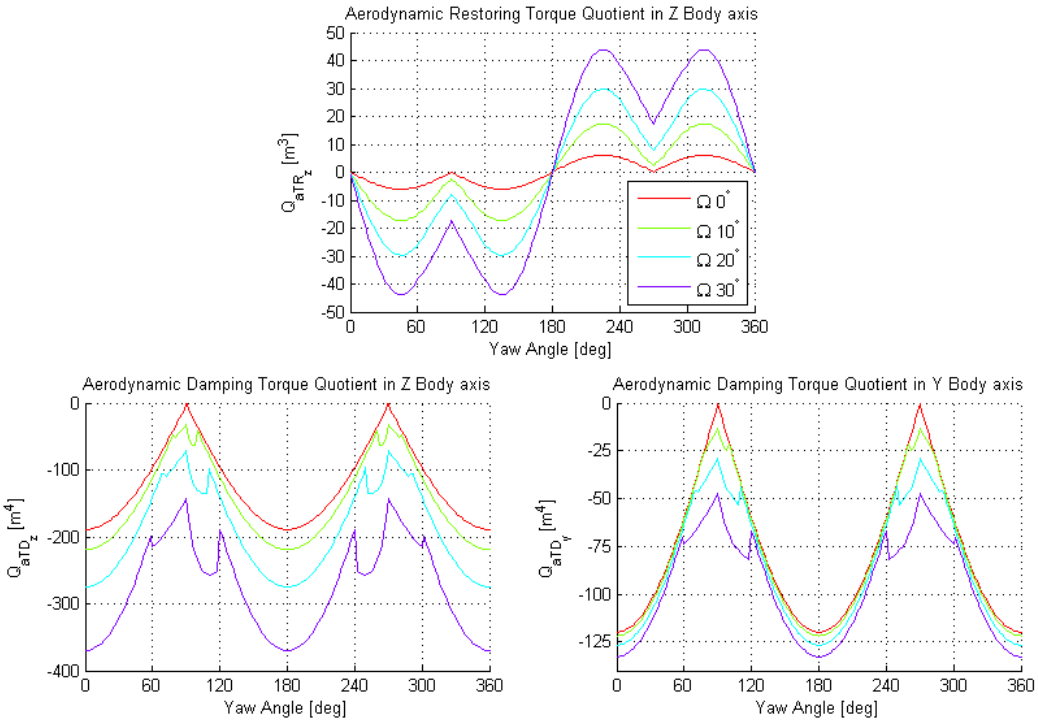

Figure 5.12: Aerodynamic torque quotients for a pyramid sail with different Ω

The solar force and torque quotients show a very similar behavior to the aerodynamic ones, hence the same conclusions can be drawn. Again, the force quotient in Z Body axis has not been included in Figure 5.13 because, for symmetry, it is identical to Q_{sx} but with a variation along the Pitch angle.

The quotients depend linearly from the changes of sail area and reflectivity coefficient. The mast length instead has an influence similar to the Ω one, but only on the torque quotients. Figure 5.14 shows the torque quotients profile for the same sail configuration treated previously, but with fixed $\Omega = 10°$.

The resulting behaviors are qualitatively equivalent to the variable Ω case of Figure 5.12, presenting increasing torque values with increasing mast length.

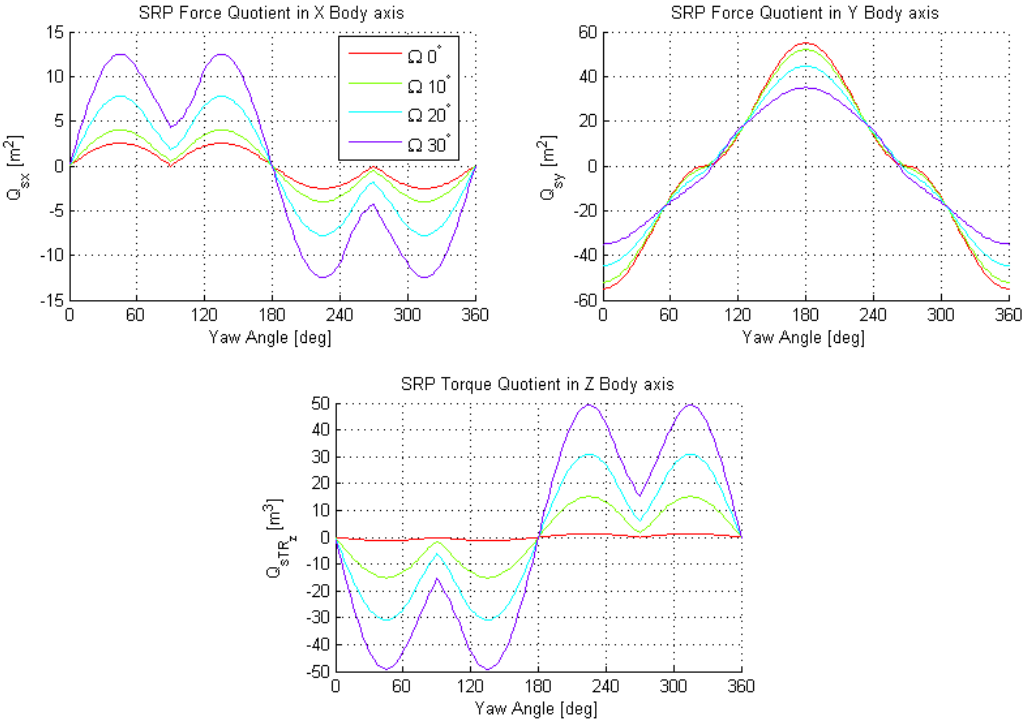

Figure 5.13: Solar force and torque quotients for a pyramid sail with different Ω

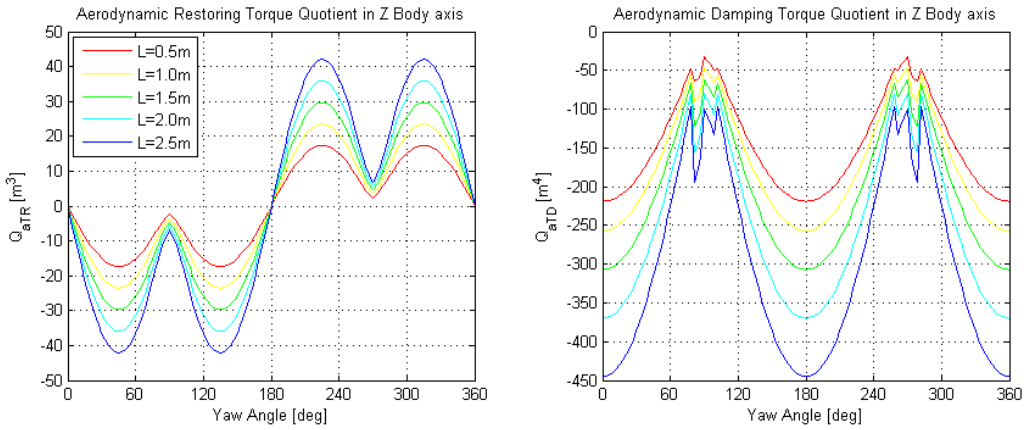

Figure 5.14: Aerodynamic and restoring torque coefficient for a pyramid sail with different mast lengths

5.2.5 Intershielding effect

The aerodynamic and solar forces acting on the deorbiting system are, generally, generated by the sail due to its larger area. However, in some situations, the deorbiting of an object does not require particularly large sails and the reference area of the satellite can be of the same order of magnitude of the sail one. To be able to identify when neglecting the intershielding produces an unacceptable error on the results, some preliminary analysis have been performed.

Without loss of generality of the results here presented, Figure 5.15 shows, for a 10° sail, the error between accounting or not for the inter-body shades. In the upper graph the drag and lift coefficient (Q_D / A_{ref} and Q_L / A_{ref}) computed considering intershielding is compared to the error committed by not accounting for it. The profiles represent different ratios of sail area over satellite area.

The difference between considering and neglecting the intershield phenomenon is mostly visible between ±60° of yaw angle. Within this range the satellite casts a shadow on the sail, decreasing its exposure to the flow/light and, consequently, decrementing its drag and lift coefficients. This decrease corresponds to the error committed when intershielding is not taken into account. It is intuitive that the larger the difference between the size of the sail and the satellite, the lower the impact of one object on the other. It is visible in the plots that the error for an area ratio sail/satellite of 35 is much smaller than, for instance, the one of ratio 2.

This analysis has been done for the aerodynamic forces quotients; for the SRP the trend is equal with similar numerical impact.

A more relative measure of the committed error can be obtained by dividing the norm of the deviation by the norm of the total aerodynamic force quotient, for all the computed points. The resulting profile for different sail/satellite area ratios is presented in Figure 5.16. In accordance with the previous graph, Figure 5.16 shows a very high percentage error for yaw angle range referred above. As before, the lower the area ratio, the larger the relative error.

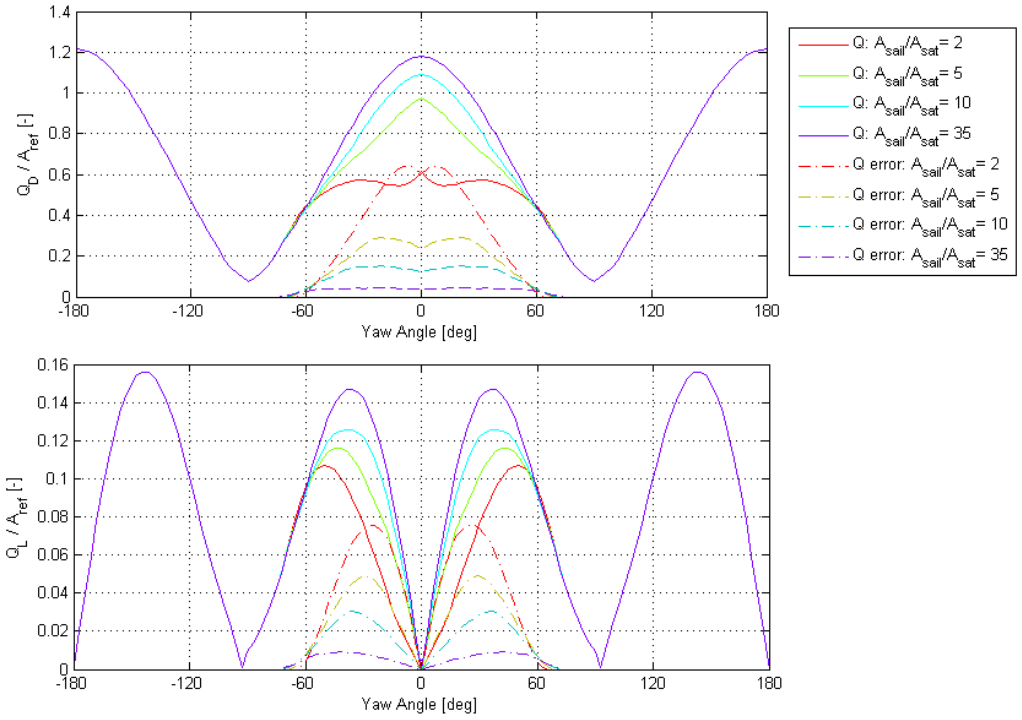

Figure 5.15: Drag and lift coefficient with intershielding and committed error when neglecting it

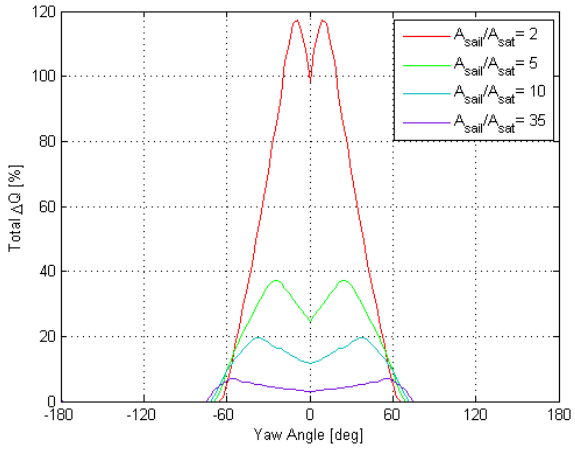

Figure 5.16: Error on the total aerodynamic force quotient computation neglecting intershielding, for different sail/satellite area ratios

It is important to evaluate how the magnitude of force error due to the errors just shown compares to the remaining environment force(s), i.e. how the maximum resulting error on the aerodynamic force compares to the minimum solar force. This, of course, has to be look at as a function of the altitude, as the relative

magnitude of two forces highly depends on this parameter. To assess this, the force quotient accurately computed (accounting for intershielding) is divided in two terms: the coarsely estimated value neglecting intershielding $\tilde{Q}_{iF}$ and the error of this approximation ΔQ_{iF}. This is

$$\begin{aligned} Q_{AF} &= \tilde{Q}_{AF} + \Delta Q_{AF} \\ Q_{SF} &= \tilde{Q}_{SF} + \Delta Q_{SF} \end{aligned} \tag{5.2}$$

Computing the maximum error committed not considering intershielding and dividing it by the minimum of the remaining environment force, the following ratios are obtained

$$\begin{aligned} \frac{\Delta F_{A\max}}{F_{S\min}} &= \frac{\varrho \left|\underline{v}\right|^2 \Delta Q_{AF\max}}{P Q_{SF\min}} \\ \frac{\Delta F_{\mathrm{S}\max}}{F_{A\min}} &= \frac{P \Delta Q_{SF\max}}{\varrho \left|\underline{v}\right|^2 Q_{AF\min}} \end{aligned} \tag{5.3}$$

These ratios are shown for different altitudes, respectively in the upper and lower graphs of Figure 5.17. This way it is possible to identify when the error committed by neglecting the intershielding when computing one of the forces is greater than the remaining force. In the graphs the 1 line is highlighted for easier reading of the points/altitudes where the error becomes larger than the remaining force. Moreover, for completeness, the analysis has been performed in both solar maximum and minimum conditions. As expected, for the error in the aerodynamic quotient, the higher the ratio area sail/satellite, the lower the altitude threshold. For the solar quotient the rational is the inverse. The maximum solar activity makes both thresholds rise in altitude.

As can be seen from the plots that there is no altitude for which the lines of the two ratio types (for the same sail area ratio and the same solar cycle moment) are simultaneously below the 1 line. This means that for every (considered) sail sail/sat size and both for solar high and low activity, the maximum error on one of the forces is always higher than the minimum value of the other force. It is then natural to conclude that whenever a sail-satellite configuration is simulated in 6DoF under both aerodynamic and solar force, the intershielding effect must be taken into account.

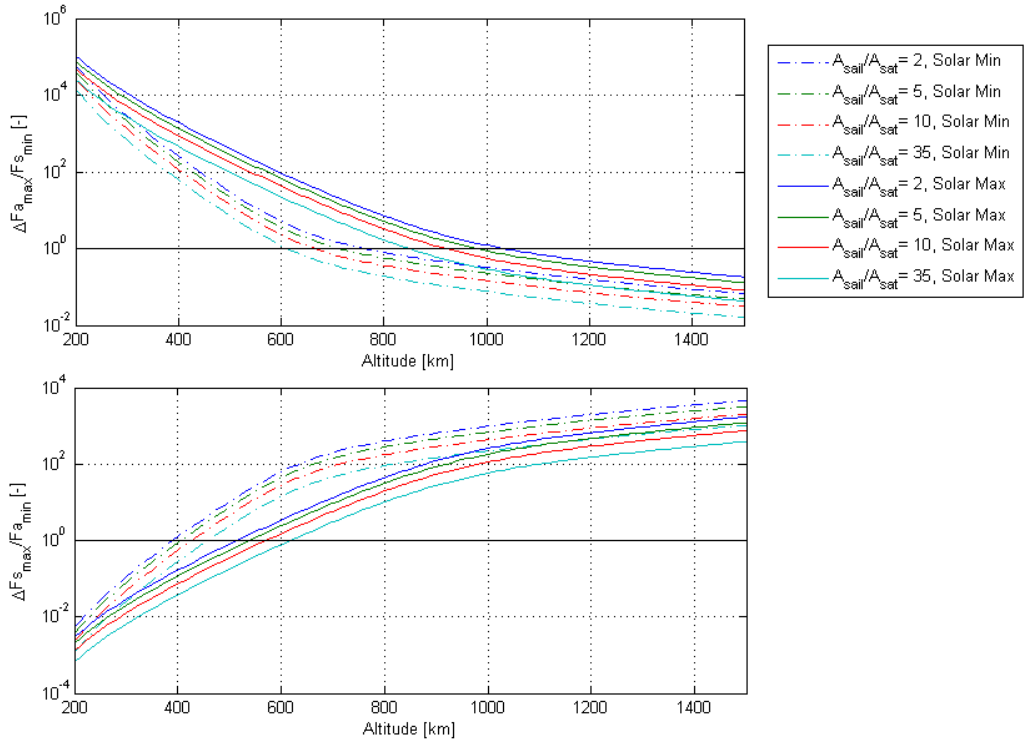

Figure 5.17: Maximum intershield error compared to minimum force

5.2.6 Effect of attitude on force along altitude

It is now clear that the attitude and the system shape has an important impact on the deorbiting performances. It is therefore useful to review the force magnitude distribution along altitude having in account the variability of the force quotients.

Figure 5.2 shows the altitude profile of the aerodynamic and SRP forces. From there it was possible to infer on the altitude for which the aerodynamic force becomes predominant over the SRP and vice versa. However, if the range of the force quotients for a system (that here serves as example) is considered, this plot becomes the one shown on Figure 5.18. This analysis has been done for a 30 m^2 sail with $\Omega = 10°$, on a circular equatorial orbit, with zero RAAN, but it represents the general trend of the aerodynamic and solar forces acting on a sail at different altitudes and attitudes. The quotients used for the generation of this graph are:

- $Q_{S\,\min}$: the solar force quotient for the sail parallel to the Sun vector;
- $Q_{S\,\max}$: the solar force quotient for the sail perpendicular to the Sun vector;
- $Q_{D\,\min}$: the drag force quotient for the sail parallel to the air flow vector;
- $Q_{D\,\max}$: the drag force quotient for the sail perpendicular to the air flow vector;

These quotients characterize the best and the worst attitude cases in terms of produced force for the system considered. They allow the calculation of the force

limits at each altitude. The obtained bands include all the possible obtainable forces, depending on the attitude, at each altitude. The drag force has been reported in the maximum and minimum solar condition.

It is therefore possible to observe that the altitude threshold under study is not a precise point at all but, instead a large region of intersection of the aerodynamic and the SRP force bands.

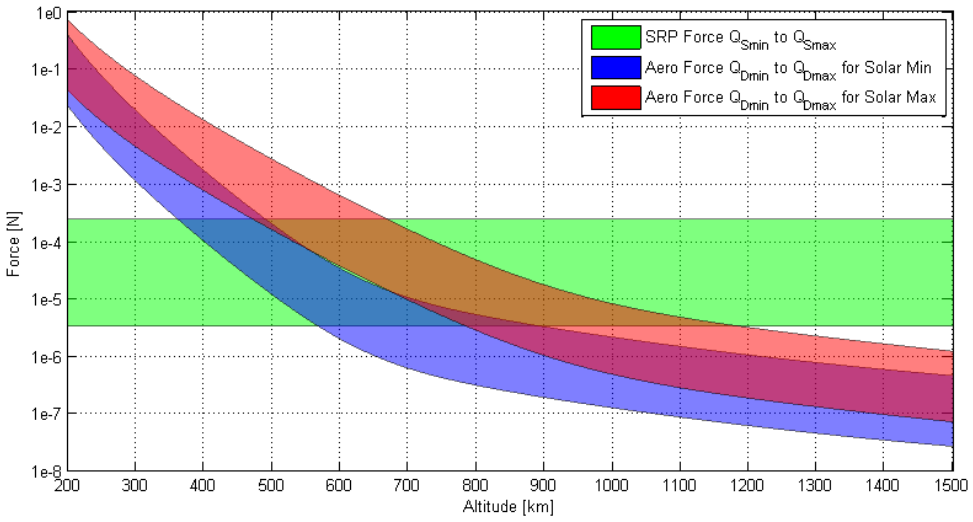

Figure 5.18: Aerodynamic and SRP force comparison for best and worst attitude configurations

5.2.7 Initial conditions and average drag coefficient

An important property of the sail design is the effective drag it generates when oscillating or tumbling. This gives the designer an idea of the loss of performance caused by the non-ideal attitude motion. To study this dynamic property, the sail attitude behaviour as a response to initial Angle of attack and Angular rate is here observed. The drag coefficient is equivalent to $C_D \equiv Q_D / A_{ref}$.

Figure 5.19 shows the average drag coefficient for different sail Ω angles, in function of various initial angles of attack a. This study has been conducted with the 6 DoF simulator but considering the satellite as point mass of 100 kg, while the rest of the deorbiting system has the characteristics expressed on Table 5.7.

This sail is subjected to a fixed flow of velocity $\underline{v}_\infty = \begin{bmatrix} 0 & 7.6 & 0 \end{bmatrix} km/s$ at a constant density equivalent to an altitude of 400 km, and its behaviour under different initial angles of attack has been studied. The solar action is here neglected because the purpose of this study is the aerodynamic force influence. The results of this analysis are shown in Figure 5.19.

For low angles of attack the flat sail produces the highest average C_D but at $a = 90°$ it has zero drag so it remains still, parallel to the flow. For higher Ω the average drag shows lower values for low angles of attack. At higher angles however the drag increases with Ω as the 'side' also increases. Higher Ω sails thus show a

more uniform curve of average C_D. The profiles of all four sails are not symmetric around $a = 90°$ because the system departing from high angles of attack reaches the stable position of $a = 0°$ oscillating through all the others angle of attacks conditions; this determines a lower average drag coefficient respect to the cases with a low initial AoA.

Propriety	Value
Sail shape	Pyramid
Sail Base Area	20 m^2
Sail mass	1kg
Sail aerodynamic proprieties	Typical solar sail
Mast length	2 m

Table 5.7: Average C_D *vs* initial AoA, for different Ω, input set

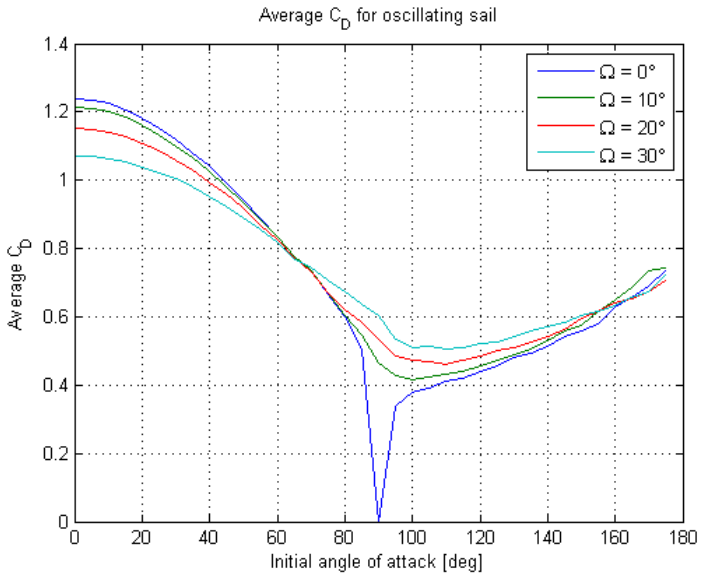

Figure 5.19: Average C_D of an oscillating sail for different Ω

A similar survey has been conducted for an identical system but for different initial angular velocity values. The outcome is reported in Figure 5.20.

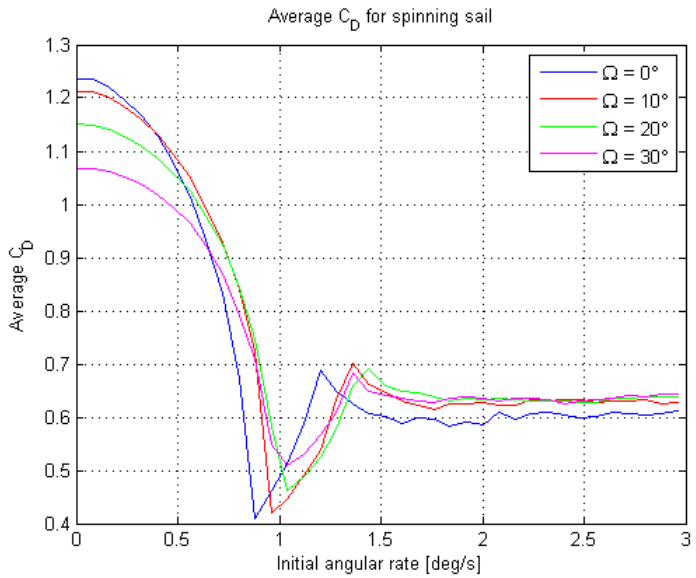

Figure 5.20: Average C_D of a sail for different Ω under initial angular rate

Under initial angular rate the sails yield maximum average C_D for low initial rates. In this condition, the initial rate is low enough for the restoring torque to break it and force an oscillatory motion the stable attitude. As the initial angular velocity increases the highest reached angle during oscillations also rises, quickly decreasing the average C_D. A minimum of this coefficient is achieved when the oscillation peaks are around 90deg, attitude for which the exposed area is minimal. Passed that point, there is an increase of the average drag as the drag coefficient profile has a lobe in the back of the sail similar to the one in front. When the restoring torque fails to break the initial angular velocity, i.e. when the system arrives at 180 still with rotation rate, attitude oscillations do not happen anymore and instead the system tumbles. After passing the tumbling threshold the average C_D converges to the mean value of the coefficient *vs* attitude profile, weighing equally all orientations. The flat sail shows a slightly lower average C_D value during tumbling, while the higher Ω shapes present very similar values.

These studies have been conducted analyzing the response to the initial angle/angular velocity around the pitch axis. For symmetry, the results here shown are extended also to the Yaw angle behavior. The roll does not affect the drag.

The same initial conditions analysis has been conducted for different mast lengths with the results reported in Figure 5.21 and Figure 5.22. The most obvious conclusion is on the independence of the average C_D from the mast length for each initial angle of attack. This is because changing the mast length only influences the oscillation frequency around the stable attitude, the drag coefficient average value remains constant. A more detailed explanation about this effect will be provided in Section 5.2.9.

The response of systems with different mast length to an initial angular velocity, instead, shows a behavior very similar to what described for different Ω. However, the average C_D profiles for different lengths differ from each other only in the angular velocity threshold for which the initial rotation cannot be broken. A longer mast system has the threshold of tumbling at a lower initial angular velocity because the restoring torque it produces, although higher than that of a shorter mast system, is not strong enough to break the motion of its higher inertia. The constant asymptotic value reached during tumbling (for high initial angular rate) is equal among all configurations and it is coincident with the one observed in Figure 5.20. These results find a confirmation in the following paragraphs.

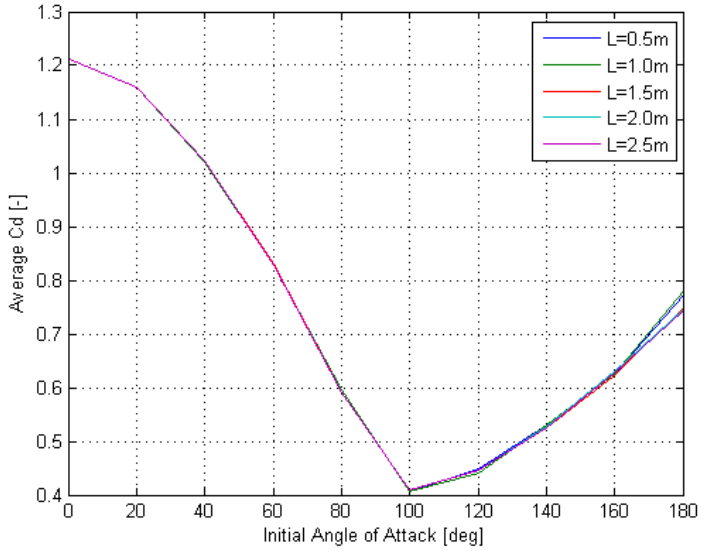

Figure 5.21: Average C_D of a oscillating sail for different mast lengths

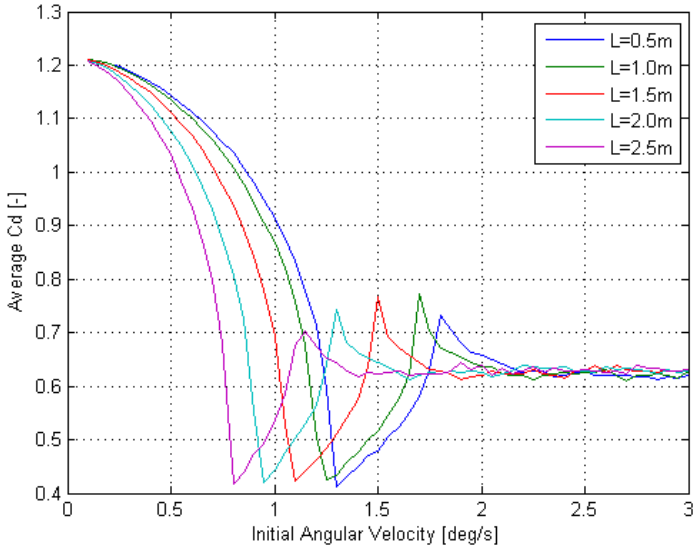

Figure 5.22: Average C_D of systems with different mast length under initial rate

5.2.8 Damping ratio

As already seen when deducing the aerodynamic quotient expressions, there is a damping fraction of the total moment, which means that, when oscillating or tumbling the flow is slowly extracting energy from the system. A measure of this damping can be studied through the observation of two consecutive attitude peaks in an oscillatory attitude motion. Figure 5.23 shows an example of damped attitude profile for a sail with the following characteristics:

Propriety	Value
Shape	Pyramid
Area	20 m^2
Ω	30°
Initial AoA	50°

Table 5.8: Damped sail oscillation parameters

This sail is subjected to a fixed flow with a velocity of $\underline{v}_\infty = [0 \quad 7.6 \quad 0] km/s$, at a constant density equivalent to an altitude of 400 km, with no SRP, for a total of 5 days. This simulation has been performed with the 6 DoF simulator but considering the satellite as point mass of 100 kg.

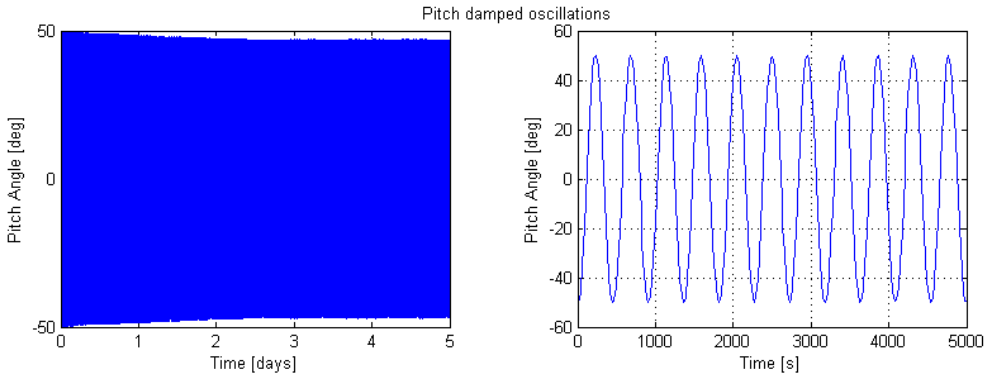

Figure 5.23: Damped oscillation around Pitch axis caused by aerodynamic – plotted for 6 days (left) and one orbit period (right)

In Figure 5.23 it is possible to notice a light damping effect which, obviously, becomes more evident increasing the simulation duration.

The oscillation damping can be evaluated through the damping ratio, defined by logarithmic decrement [**39**]

$$\xi = \frac{1}{\sqrt{1 + \left(\frac{2\pi}{\ln\left(\frac{x_0}{x_1}\right)} \right)^2}} \tag{5.4}$$

where x_0 and x_1 are, respectively, the amplitude of the first and second peaks.

The damping ratio has been evaluated for a system with different initial angles of attack and for different Ω. As for the previous analysis, a deorbiting system with a 100 kg point-mass satellite is subjected to a fix flow with a velocity of $\underline{v}_\infty = [0 \quad 7.6 \quad 0] km/s$, and a density equivalent to 400 km altitude. The 6 DoF simulator with no SRP was used. In this simulation only Pitch angle was considered (so angle of attack is here equivalent to Pitch angle).

Propriety	Value
Sail shape	Pyramid
Sail Area	20 m^2
Sail mass	1kg
Sail aerodynamic proprieties	Typical solar sail
Mast length	0.5 m

Table 5.9: Damping attenuation *vs* initial AoA angle, for different Ω, input set

The result of this analysis is shown in Figure 5.24. As it is visible the damping ratio is extremely small. This is due to the large relative difference between the flow velocity and the component induced by the rotation of the spacecraft (which is the only source of damping). The higher is the initial Pitch angle, the stronger is the damping of the oscillations. This may be explained by the fact that, for higher amplitude oscillations the rotation motion reaches higher angular rates scaling up the damping torque fraction which depends on the angular velocity.

However, differently from what could have been deduced from Figure 5.12 where the flat sail had the lowest damping torque quotient, here it shows the highest damping ratio. This can be explained by the lower inertia of a flat sail. Indeed, recalling the expression of the angular velocity variation:

$$\dot{\underline{\omega}} = -\underline{\underline{J}}^{-1}\underline{\omega} \times (\underline{\underline{J}}\underline{\omega}) + \underline{\underline{J}}^{-1}\underline{T}_R + \underline{\underline{J}}^{-1}\underline{T}_D \tag{5.5}$$

it is observed that the last term, which is the damping contribution to $\dot{\underline{\omega}}$, is directly proportional to the damping torque but inversely proportional to the inertia of the system. Since the inertia grows with the square of the distance to the moment centre, while the torque increases linearly with it, it is now clear why the flat sail damping ratio shows such a higher ratio. This behaviour can be easily expressed in a graphical way showing the ration between the aerodynamic damping torque quotient and the inertia moment both around the Z Body axis. Figure 5.25 shows that the highest values, in magnitude, of this ratio, and therefore damping effect, correspond to the flat sail. This has an exception for side wind case where the flat sail do not produces relatively damping torque.

Again the mast length impact was also studied. The damping ratio for oscillations under different initial attitudes was done using a similar simulation setup as for Ω. Figure 5.26 shows that a longer mast provides a lower damping ratio.

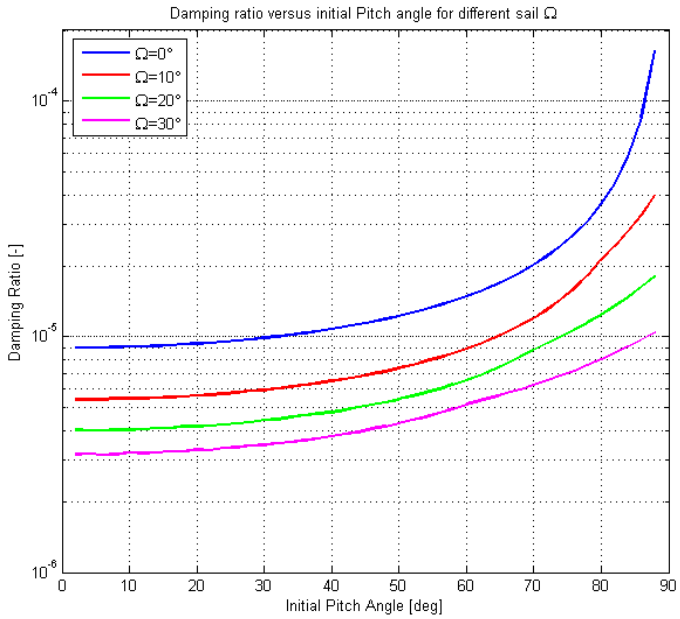

Figure 5.24: Damping ratio of a sail with different initial AoA and Ω

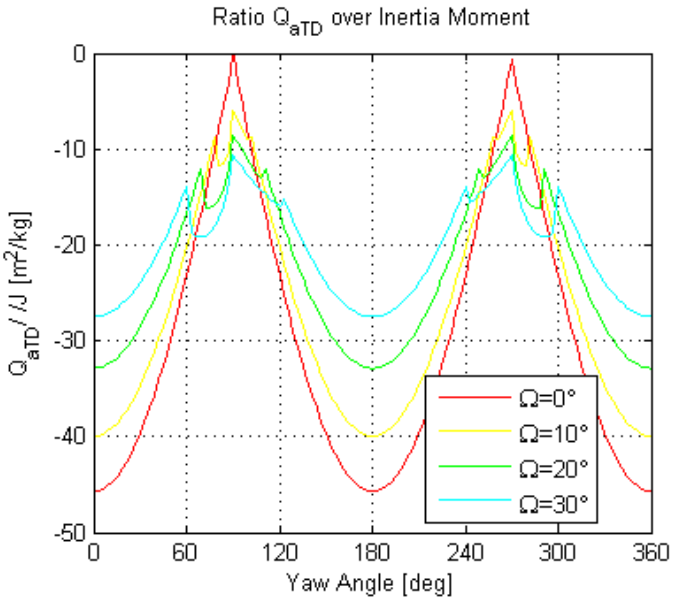

Figure 5.25: Aerodynamic damping torque quotient and inertia moment ratio for different Ω

As shown for Ω, the ratio of damping torque quotient divided by the inertia moment revealed the role of the inertia in the damping effect. The results presented in Figure 5.27 give another perspective on the fact that a shorter mast (lower inertia) indeed yields a better damped response to oscillation.

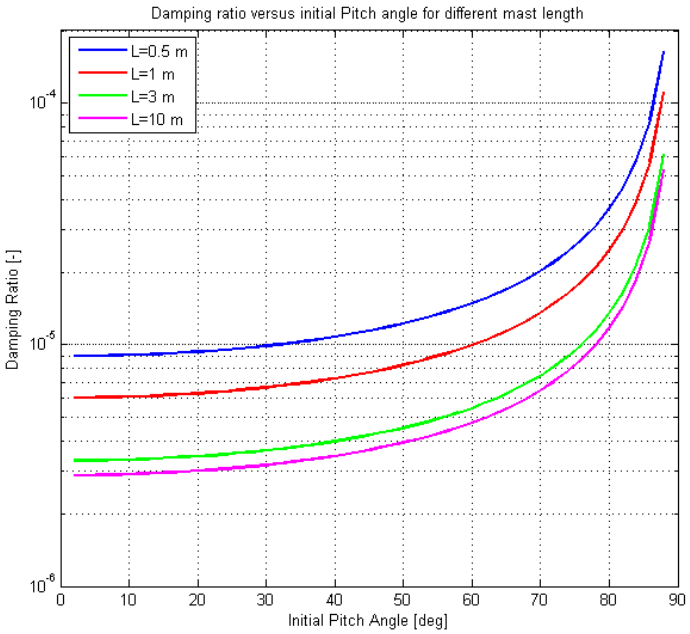

Figure 5.26: Damping ratio of a sail with different initial AoA and mast length

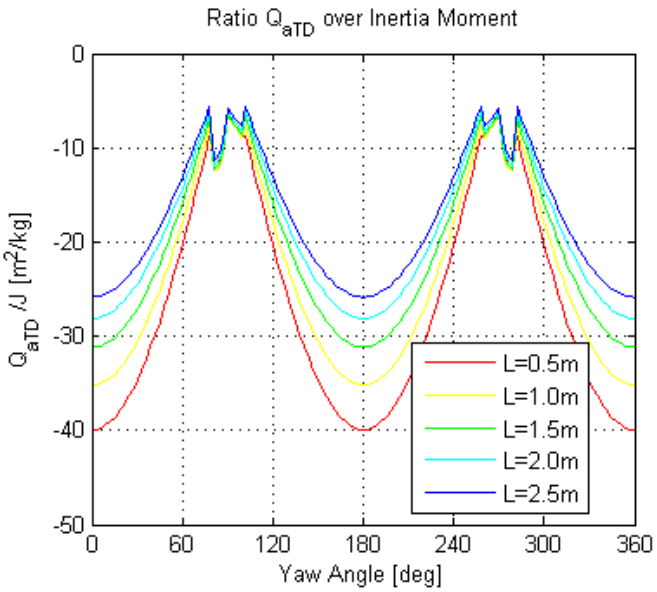

Figure 5.27: Aerodynamic damping torque quotient and inertia moment ratio for different mast lengths

5.2.9 Speed of restoring

While the damping torque contains information about the ability of the system to attenuate oscillations over time, returning to the stable attitude, the restoring torque is tightly connected to the speed response of the system. This means that an

object capable of producing a high restoring torque responds quickly to a tracking change. However, it is also more sensitive to disturbances. The restoring torque influences the average C_D as it defines the threshold of tumbling motion.

To understand the influence of Ω and the mast length L on the restoring torque, the ratio between the restoring torque quotient and the inertia moment, has been plotted in Figure 5.28.

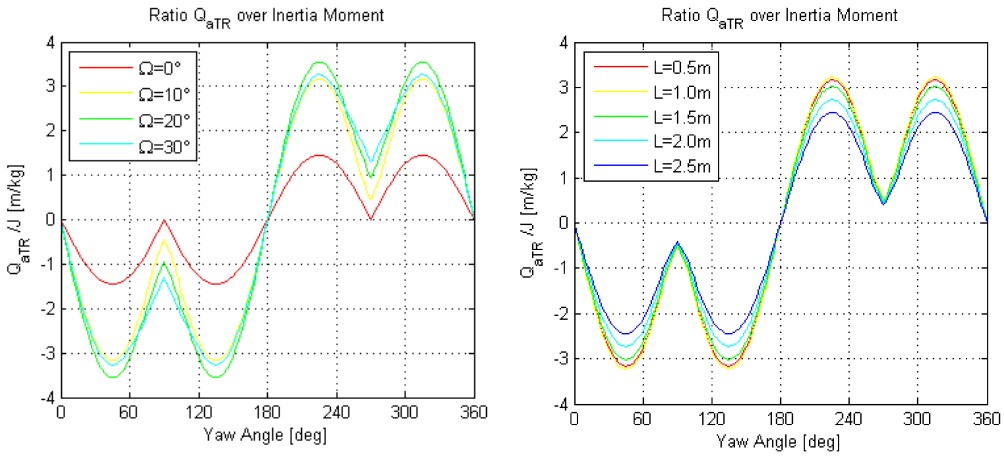

Figure 5.28: Aerodynamic restoring torque quotient and inertia moment ratio for different Ω (left) and mast lengths (right)

Differently from the damping results, the restoring torque maximum values are not coincident with the maximum or minimum of the parameters understudy: an Ω of 20° and an L of 1 m show the highest values. These two parameter values provide a faster/more reactive system.

5.2.10 Flexibility

The mast length not only influences the dynamics of system but it also changes its flexible behaviour. This is fundamental both for the study of vibration issues (out of the scope of this research) and for the possible consequences of the relative movement of satellite and sail on the attitude behaviour. This latter situation is mainly caused by the bending of the mast due to an unbalanced system of forces acting on the satellite and sail.

In order to obtain a coarse measure of the mast deflection for a broad set of loads and mast lengths, this structural piece can be analysed using a Euler-Bernoulli cantilever beam model under tip loading. The static tip deflection for this model is

$$v_{tip} = \frac{P_{tip} L^3}{3EI} \tag{5.6}$$

Where L is the beam length and P_{tip} is the load applied on the tip. The theoretical assumptions to obtain the cantilever beam displacement v_{tip} have been treated in Section 4.3.2.

The beam characteristics used in this analysis correspond to the standard telescopic mast proprieties set for this research (*vide* Section 5.2.1). Of those, the parameters here used are summarized in the following table.

Propriety	Value
Cross section shape	Hollow square
Cross section width w	0.006 m
Cross section height h	0.006 m
Cross section thickness t	0.003 m
Young's modulus E	73.1 GPa

Table 5.10: Flexible beam proprieties

The tip load magnitude range used in the analysis includes the most typical values of transmitted forces between satellite and sail for a deorbiting. Figure 5.29 shows the tip deflection expressed as percentage of the relative beam length, obtained with Expression (5.6).

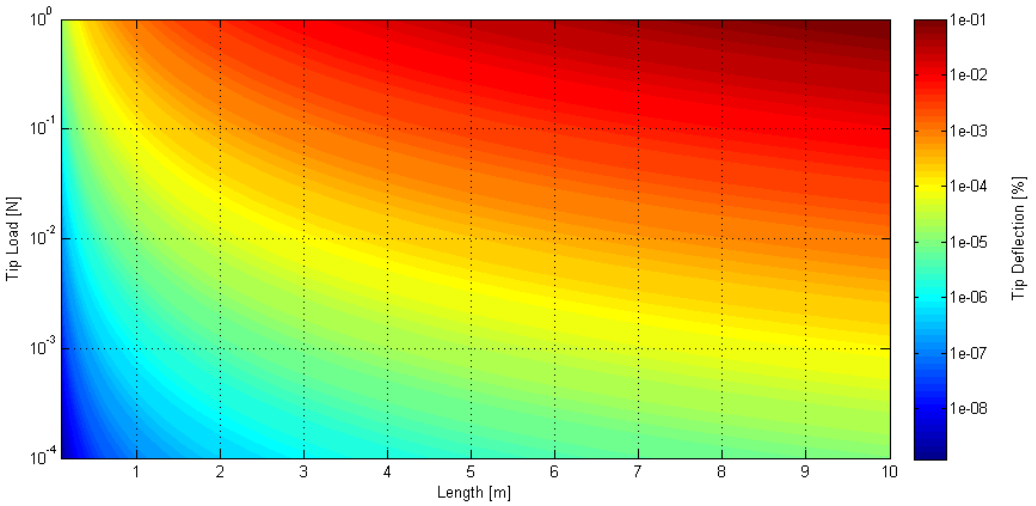

Figure 5.29: Tip deflection of a cantilever beam (in percentage of beam length) for variable tip load

As expected, a longer beam results in a greater tip deflection but, even the maximum displacement does not produce a considerable misalignment between the two beam extremities. However, the impact of this displacement on the deorbiting performance will be studied in Section 6.2.5 and in Appendix A.3.1.

5.3 SRP effects

During a deorbiting the two main non conservative forces acting on the object are the aerodynamic and solar one. The aerodynamic force acts approximately on the direction of the velocity, always slowing down the object. This makes it, in general, the most effective external force in the deorbiting process. The solar force instead acts approximately in the direction of the incoming Sun light, which can have

multiple orientations with respect to the velocity vector, depending on the position, the orbit and the epoch. Hence, its effect on the attitude can be unpredictable, especially when its order of magnitude is similar to the one of the aerodynamic force/torque.

This section shows how the SRP force/torque can, for certain conditions, cause instability.

5.3.1 Attitude stability under SRP

To observe the effect of the solar radiation pressure on the attitude of an object during the deorbiting, a test with the following system input has been performed:

Propriety	Value
Satellite mass	100 kg
Satellite dimensions (l×h×w)	1m×1m×1m
Satellite aerodynamic proprieties	Normal accommodation
Sail mass	1.2 kg
Sail shape	Pyramid
Sail Area	30 m^2
Sail Ω	10°
Sail aerodynamic proprieties	Typical solar sail
Mast length	0.5 m

Table 5.11: Attitude SRP destabilization test input parameters

The attitude of the system has been analysed on a 500 km altitude orbit, with 80° of inclination and 90° of RAAN. These orbital parameters were selected in order to obtain an eclipse-free orbit during Vernal Equinox (from Figure 5.3). The effect of the SRP has been excluded in a first simulation and included in a second one, emulating, for example a totally transparent sail *vs* a totally reflective one, respectively. These simulations have been performed with the 6 DoF simulator for a duration of 8 days.

Figure 5.30 and Figure 5.31 shows the different attitude profiles and rates (Pitch and Yaw) in these two conditions.

It is clear that the presence of the SRP strongly destabilize the attitude behavior of the system. The resulting tumbling decreases the average drag of the sail therefore increasing the deorbiting time. This effect, however, depends on many factors as the altitude, the solar cycle stage and the presence of eclipses. The effect of the latter is studied in the following section.

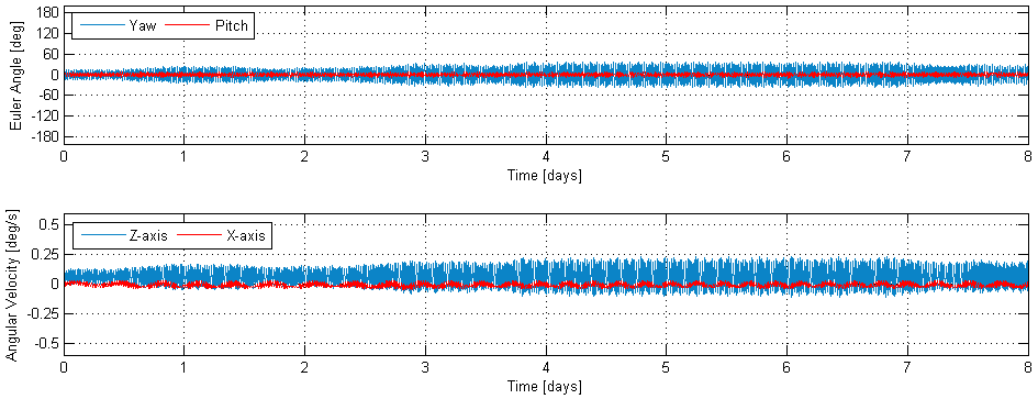

Figure 5.30: Attitude at 500 km altitude with totally transparent sail

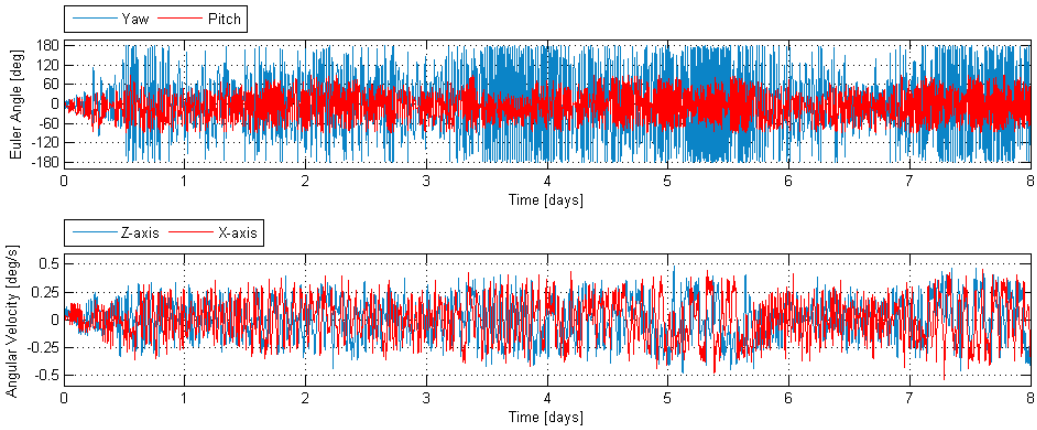

Figure 5.31: Attitude at 500 km altitude with totally reflective sail

5.3.2 Eclipse disturbance

Eclipses cause an on/off effect in the SRP force and moment. The switching happens reasonably suddenly considering the rate of change of the remaining orbital disturbances. Such quick transitions may have a highly destabilizing effect on the attitude motion of the spacecraft. Two particular cases are:

- when the SRP torque drives the attitude behavior and the aerodynamic torque is relatively weak (the spacecraft oscillates around the Sun direction). This happens mostly at high altitudes, especially for low solar activity;
- when the spacecraft oscillates around the velocity axis (flow direction) but the SRP moment has still a magnitude comparable to the aerodynamic one. This occurs at medium altitudes.

To have an example of this, a simulation run for each of these cases is here shown. To better isolate the effect of the eclipse, the density along the orbit has been kept constant and equal to the average value for the initial altitude. The orbital parameters for both simulations were selected so that the precession due to J2

would cause the spacecraft to experience eclipses only on the second half of the simulated time window.

The deorbiting system used in both test cases is characterized by the proprieties reported on Table 5.11. The orbital parameters are summarized on the following table.

	Parameter	**Value**
Sun Tracking	Altitude	750 km
	Eccentricity	0
	Inclination	68°
	Epoch	Spring equinox
	Solar level	Low
Flow Tracking	Altitude	600 km
	Eccentricity	0
	Inclination	70°
	Epoch	Spring equinox
	Solar level	High

Table 5.12: Eclipse effect analysis orbital parameters

Figure 5.32 shows the attitude profile for the Sun tracking condition, while Figure 5.33 report the results of the analysis for flow tracking case.

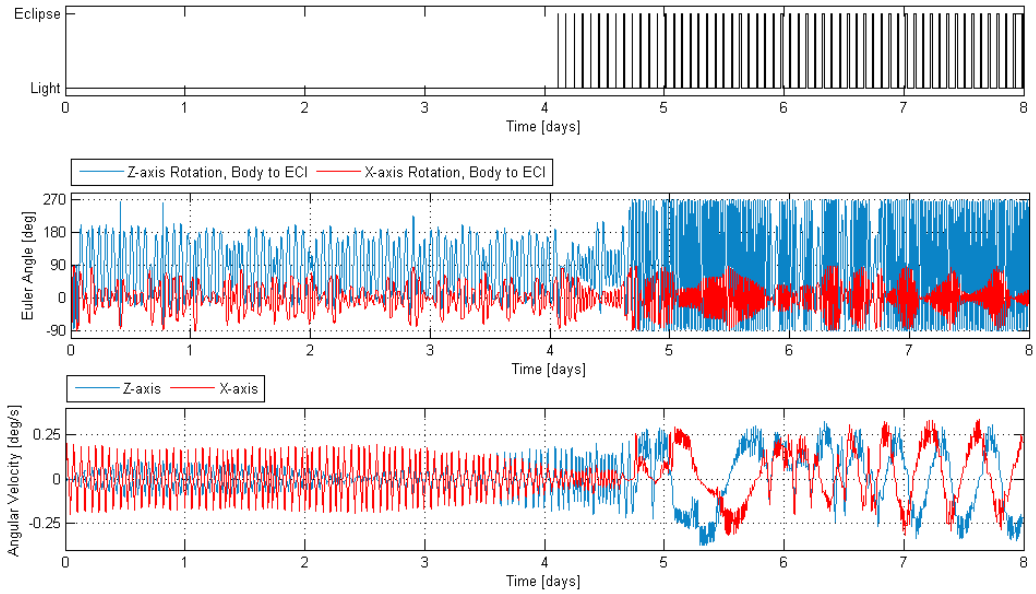

Figure 5.32: Eclipse effect at 750 km altitude, with low solar activity (Sun tracking)

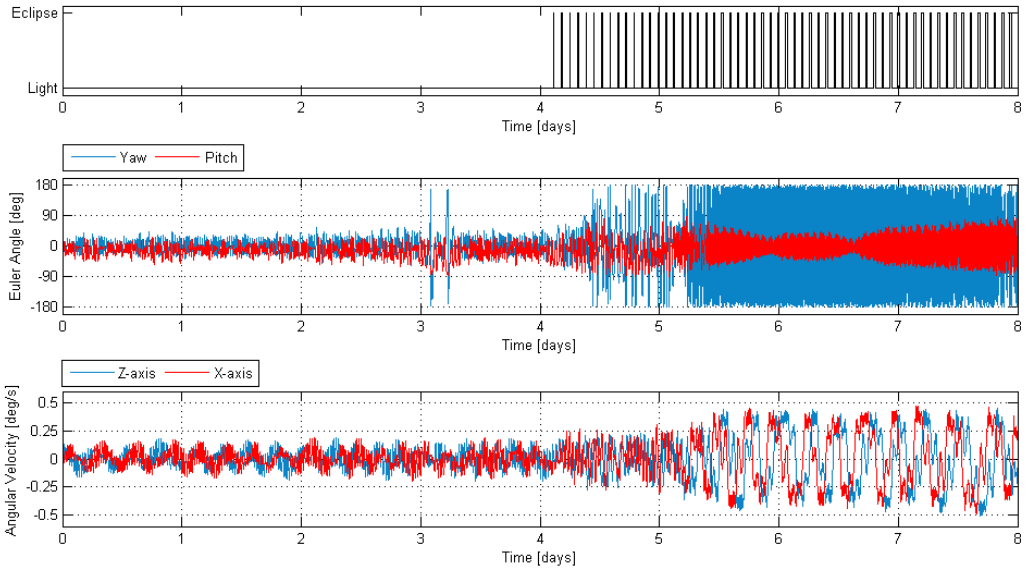

Figure 5.33: Eclipse effect at 600 km altitude with high solar activity (flow tracking)

On both Figure 5.33 and Figure 5.32 the spacecraft starts by having a regular oscillatory motion around a stable attitude: in the case of Figure 5.33 around the velocity direction, and on the case of Figure 5.32 around the Sun direction. This oscillation is visibly broken shortly after the beginning of the eclipse season. After this point, and in both cases, the spacecraft enters a tumbling state, noticeable not only for the wide and fast changes of the attitude angles but also for the angular rate drift. Such tumbling motion causes a decrease of the average drag coefficient, and ultimately a longer deorbit time.

5.3.3 Sail Optical Properties

As the previous section described, the SRP action can have destabilizing effects on the system attitude. However, at high enough altitude, this force is dominant causing the satellite-sail system to oscillate around the Sun direction. (This was also depicted in the previous section.) In such case, the main ΔV is induced by the SRP. The effect of this action on the orbit is not trivial since, unlike the aerodynamic induced one, it can assume multiple directions with respect to the orbit. In **[15]** the SRP force/torque is shown to increase deorbit duration for most initial orbits, except for high inclined ones under low solar activity. However, the results there presented are obtained for a drag assisted deorbit device including magnetic dampers. These dampers help to stabilize the spacecraft when tracking the Sun/flow as well as attenuate and aid the recovery from the instability caused by the transition from Sun tracking to flow tracking. This technology is not in the scope of this research, therefore such results cannot be assumed to apply to the sail designs here treated. Not being possible to include in the scope of this thesis a thorough 6DoF testing of the SRP effect, a small scale testing was performed.

The tests were run in the 6DoF simulator for initial orbits (circular) of 650/750 km altitude, three levels of solar activity and two transparency extremes (fully

transparent and fully reflective). The orbital inclination influence was studied using a coarse mesh in the range of 0 - 80 deg. To expedite the simulation, making it feasible in the available timeframe, the spacecraft used was 0.3 m×0.3 m×0.3 m with a 10 kg mass and a 100 m^2 sail.

The results of these runs are presented on Figure 5.34.

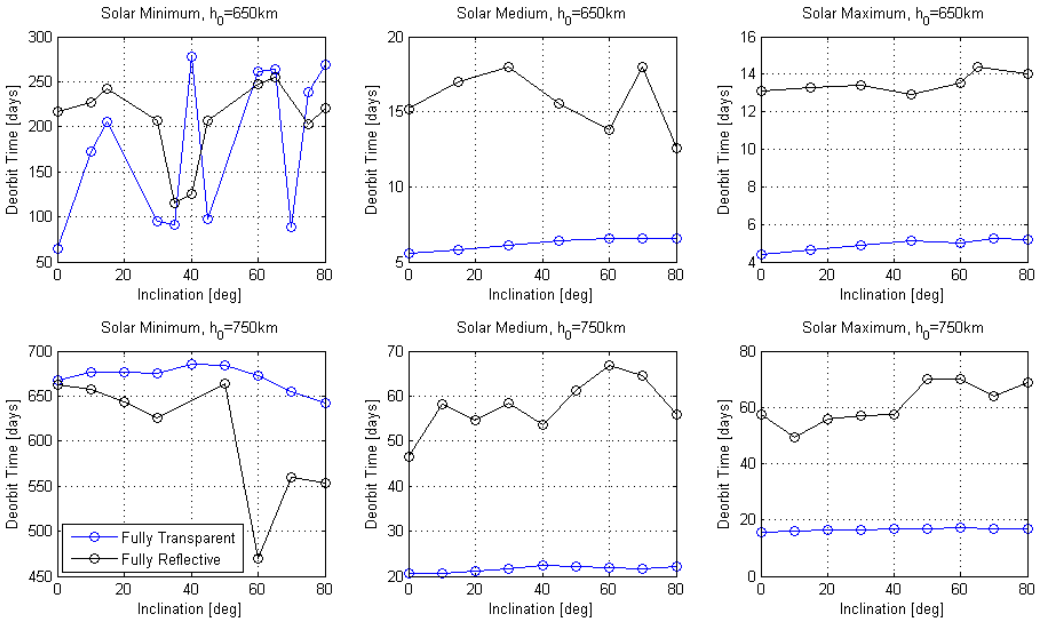

Figure 5.34: Deorbit times for fully transparent and fully reflective sails.

It is noticeable that only for low solar activity there are cases of shorter deorbit duration for a fully reflective system. For initial orbit of 650 km at low solar activity no solid conclusion can be drawn regarding the advantage of an optical profile over the other. At such altitude the magnitude of the SRP and the aerodynamic forces are similar enough to have the system constantly on the edge of attitude instability. For an initial altitude of 750 km the results better defined and a fully reflective sail yields lower deorbit time especially at high inclinations. The results here described, however, lack the generality needed to be applicable in a design case as they were obtained for perfect initial attitude conditions, specific orbital parameters and for a very low ballistic coefficient system. However, they show that for certain conditions it is indeed true that a fully reflective system (without extra damping) deorbits in a shorter time than a transparent one.

5.4 Orbital test runs

So far, several geometry parameters and environmental conditions have been found to influence the attitude performance. In this section the influence of these factors will be assessed in full orbital conditions and in function of the altitude.

Using the 6DoF simulator, the attitude behaviour in orbit of several sail designs was tested for a range of altitudes. For each (starting) altitude the attitude and

orbital motion of these designs was, for each simulation, propagated for 10 orbits. The test was performed twice: once for high solar activity and once for low. The average drag coefficient and the Root Mean Square (RMS) of the angle of attack were recorded for each test. A 1 $m \times 1$ $m \times 1$ m and 100 kg satellite was used in all simulations. SRP was included and for each altitude the initial orbit was circular and equatorial. Figure 5.35 presents the results for different Ω, sail area and mast length.

For each plot it is visible that the maximum C_D values are obtained at the lower altitude region and the minimum occur at the high altitude region. In between the is ramp-like transition that happens in a limited range of altitudes. At high altitudes the atmosphere is not dense enough to overcome the SRP disturbing action and force alignment of the spacecraft with the flow. The action of the two forces together causes, in most cases, tumbling motion, which dramatically decreases the average C_D. As the atmosphere gets denser with the decrease of altitude, the spacecraft takes longer to start and, eventually, it becomes able to sustain oscillation around the velocity axis. At low altitudes the magnitude of the aerodynamic force is so much higher than that of the SRP that no tumbling takes place. A much higher average C_D is obtained then. At this point the increase of air density only decreases the amplitude of the attitude oscillation. A better sail design should have the transition from low to high C_D as high in altitude as possible. This is an indication of its stability and flow tracking properties, making it more effective deorbiting device.

The main conclusions taken from the shown figures are:

Solar Cycle – this is the main driver of the altitude at which the transition from tumbling to oscillatory motion happens. All designs show a difference of about 200 km between their transition altitudes for low and for high solar activity.

Omega – the flat sail shows a clearly higher performance over the two pyramidal sails here tested. Its transition altitudes are at least 20 km higher than the two other designs.

Area – an increase in size of the sail results in slight increase in drag coefficient due to the lower influence created by the satellite shade. This results in a slightly better tracking performance.

Mast length – the longest mast showed the best performance of the three. Indicating that, within certain limits, a longer mast increases stability and flow tracking performance.

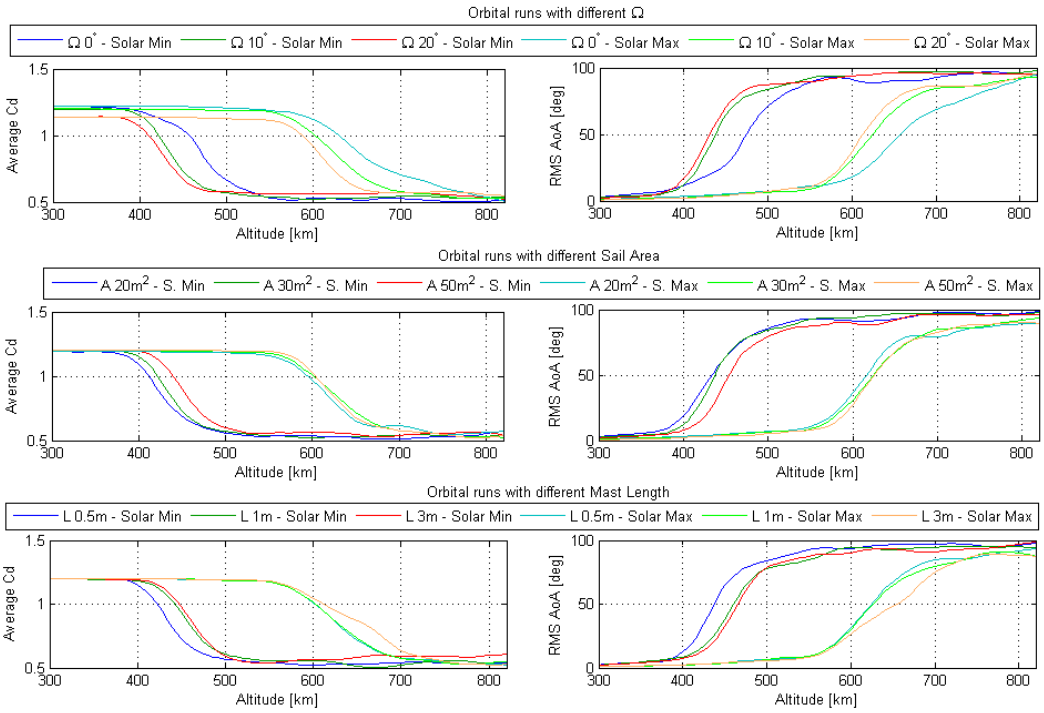

Figure 5.35: Average C_D and RMS Angle of Attack on orbital runs for several sail designs as function of the altitude.

5.5 Performance with damaged sail

The impact of the debris or meteoroid bodies with the deorbiting system could have destructive effect on the entire structure. It could lead to a decline of the deorbiting process or even to its failure and possible creation of new debris. The probability of collision between an orbiting object and the sail, and its effect on the deorbiting performances, has been subjected to a preliminary analysis.

In order to investigate the impact on the sail performances, a system with the following propriety has been implemented in the 6 DoF simulator.

Propriety	Value
Sail mass	1.5 kg
Sail area	30 m^2
Sail Ω	0°
Mast length	0.5 m
Sail aerodynamic proprieties	Typical solar sail

Table 5.13: Damaged sail input set

The aerodynamic quotients of the sail have been computed considering the presence of a puncture/hole in the sail surface. The puncture/hole was modelled with variable diameter values in order to emulate different colliding-object sizes. The simulation of this damage has been performed by removing the affected sail

segments from the forces computation. The worst scenario is represents the failure of an entire sail sector. The results are shown on Figure 5.36.

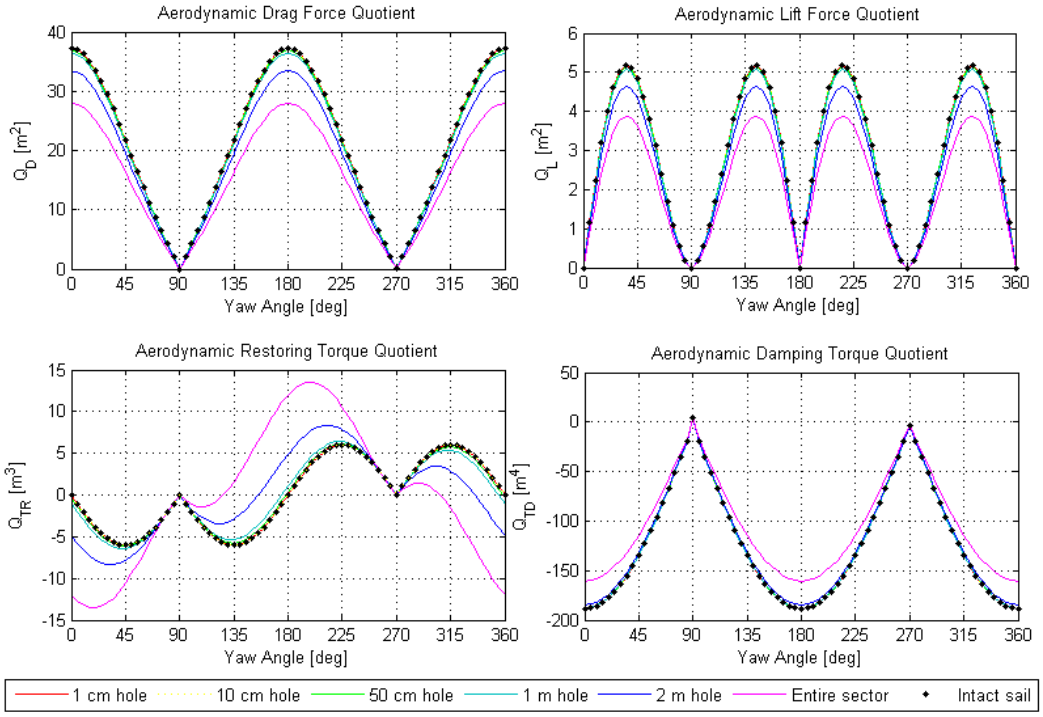

Figure 5.36: Aerodynamic quotients for a damaged sail (hole size refers to diameter)

From this analysis it can be observed that, for a typical drag-sail area, puncture sizes up to 50 cm in diameter have barely visible impact on the quotient curves. A noticeable decrease of performance happens only for very large size holes (>1m diameter, 2.5% of the sail base area). For such holes in the sail surface the drag quotient is considerably reduced and the stable attitude (yaw for which the restoring torque is null with a descending slope) shifts. Note that this offset of the stable equilibrium does not correspond anymore to a maximum of drag quotient curve: when stable the sail does not generate its maximum drag. With a lost section the sail loses almost completely its original restoring torque profile obtaining a very different behaviour.

The damaged sail quotient curves here presented could, in a more complex simulation environment, be used together with a probabilistic debris/meteoroid impact model (*vide* Appendix C) for a Monte Carlo-like campaign aiming to study, in an even more realistic way, the deorbiting process.

5.6 Summary of results

- In general, equatorial orbits show much higher predominance of aerodynamic over SRP force than inclined orbits. This is due to the equatorial diurnal bulge in the atmospheric density.
- The altitude threshold at which the aerodynamic becomes dominant over the SRP force shifts of about 200 km from high to low solar activity (higher threshold for high solar activity).
- For low orbits, deorbit time shows an inverse trend with respect to the solar activity: lower solar levels cause higher deorbit durations, and higher solar levels result in faster deorbit. For high altitudes this trend is almost perfectly inverted.
- The optimum number of sail booms is four (square base). This shape offers the best trade-off between structural efficiency and robustness.
- The area is the most fundamental property of a drag sail. It highly determines the effectiveness of the device by decreasing the system ballistic coefficient, i.e. increasing the aerodynamic force on the system. A larger sail is obviously better. This is true also because a larger sail suffers far less from the interactions with the satellite wake/shade, having a much more consistent and predictable performance over all attitudes.
- A flat sail, besides having a strongest damping effect, is capable to provide a higher reference area, and therefore a stronger drag contribution around the stable attitude. This, however, is counter weighted by the low drag on the side directions which brings its average C_D to values similar to the ones of sharper sails, with the disadvantage of offering very low or null restoring torque around the 90 deg angle of attack. A flat device also delivers higher damping capabilities. Pyramidal sails, on the other hand, show higher contribution of the restoring torque for the angular rate change, being, therefore faster and more agile to follow a reference (Sun or flow). This property has to be approached with caution since it also means higher vulnerability to disturbances which might drive the system to a tumbling state. On the conducted orbital test runs the flat sail has shown a better performance over the pyramidal ones.
- It was observed that the length of mast connecting the sail to the host satellite influenced the attitude performance of the system. A longer mast showed worse damping ratio levels: the damping quotient of longer mast systems was found to be larger, however, due to the even larger growth of the inertia moment, the damping ratio tends to monotonically decrease. In terms of speed of response, the trend is not so linear: going from a shorter mast to a longer mast the agility of the system seems to first increase and then, after a maximum value, decrease again. Orbital testing at several altitudes showed that a longer mast (within the studied limits) tends to promote performance. However, such testing was here done for specific spacecraft size, orbital and initial attitude conditions, being therefore

necessary a case to case study to understand the best choice of mast length for each design case.

- The damping effect of the aerodynamic action is, in general, extremely weak. This is due to the large relative difference between the flow velocity and the component induced by rotation (which is the only source of damping).
- The intershield phenomenon was found to decrease the performance of the sail (and ultimately of the entire system). This decrease is the highest, the closer the sail area is to the cross sectional area of the host satellite. The impact of such a shading phenomenon in the aerodynamic and SRP force levels was found to, in most altitudes, assume non-negligible values. There is then a need to always consider the intershield effect in orbital simulations.
- The optical properties of the sail system were found to influence the attitude performance of the configuration. 6DoF full deorbit testing revealed that for high solar activity, having a fully transparent sail results in minimal deorbit time. A tendency for a fully reflective system to decrease deorbit time was found for high altitude highly inclined initial orbits in combination with low solar activity.
- The solar radiation pressure action on the sail system proved to be highly destabilizing, especially at the transition altitudes where SRP and aerodynamic forces have comparable magnitudes. Such destabilizing effect was found to be further magnified by the occurrence of eclipses. These introduce a violent on/off switching feature in the SRP action, creating quick force unbalances that rapidly drive the system to a tumbling state.
- Tightly connected to the mast length, the flexibility of this structural piece was found to result in extremely small mast tip deflections for the type of mast under study and under the typical aerodynamic and SRP loads.
- The altitude and solar activity levels proved to be some of the most influential factors for the sail system performance. In the orbital test runs simulated, the attitude behaviour, and thus the average drag performance, was deeply dependant on the orbital height and on the solar cycle period. High solar activity resulted in an increase of the altitude at which tumbling is replaced by oscillatory motion of about 200 km for all tested designs.
- The quotient investigation on sail failure due to debris/meteoroid impact showed that only a very large loss of surface area ($>2.5\%$ of the sail base area) results in considerable degradation of performance of the drag system. The restoring torque quotient is the one that shows a greater change. For an entire sail sector missing the distortion of the restoring torque quotient curve is such that most of the attitude stability properties of the original sail are lost.

6 Test Cases

In this chapter the feasibility of the drag enhancement devices is verified for realistic space debris. In order to do so, two representative cases have been selected. To these, several design sizes and options were evaluated. For each, the corresponding mass budget has been compiled.

6.1 Host selection

Taking into account the range of altitude under study and most populated orbits, two possible spacecraft which could benefit from such a deorbiting system have been chosen. These are Proba-V and AVUM at EoL configuration. Both of these objects belong to the VERTA ESA program, and were launched with Vega in 2013. Figure 6.1 shows the AVUM upper stage with a in a payload configuration using VESPA adapter with Proba-V as first payload.

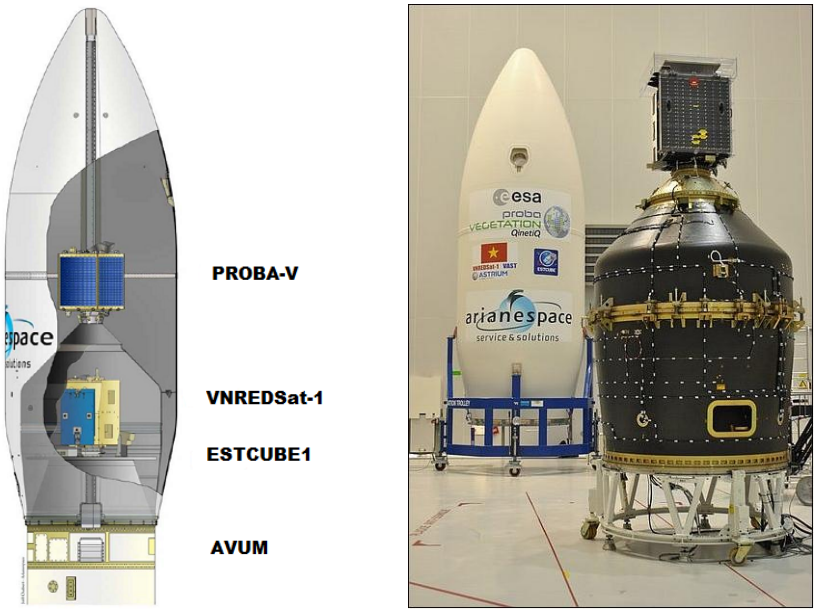

Figure 6.1: Proba-V and AVUM launch configuration [40]

6.2 Proba-V

Proba-V is the primary payload of the first launch within the VERTA programme and fundamental part of the VEGETATION project .

For this small Earth observation satellite (Figure 6.2) no disposal strategies were planned. Due to its high SSO orbit and low cross sectional area, it is believed it will not deorbit naturally within 25 years. To verify such hypothesis the ballistic coefficient for this spacecraft of 228.9 kg/m^2 was estimated using a 0.64 m^2 cross sectional area and a C_D of 0.94 (estimated by averaging the drag coefficient values computed for all the possible Yaw and Pitch combinations). Since Figure 5.6 does not reach such high ballistic coefficient value, the NASA Debris Assessment

Software (DAS) [**41**] was used to evaluate the deorbiting time. The software estimated that the spacecraft does not deorbit within the 25 years limit. A drag sail is thus here dimensioned and tested to allow its decay within a shorter period.

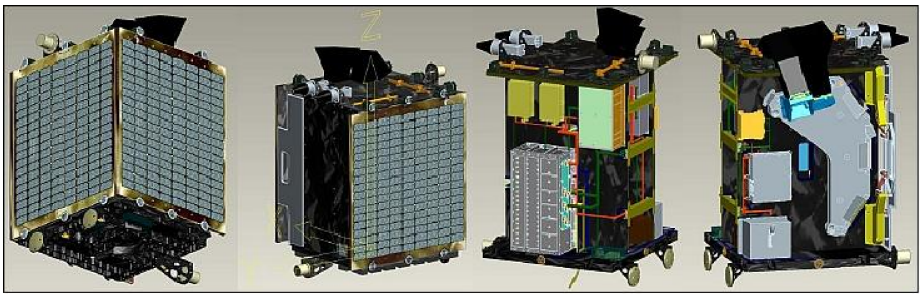

Figure 6.2: PROBA-V spacecraft accommodation, outer platform views on left, inner platform views on right [42]

6.2.1 Model

Proba-V has a regular cuboid shape. Its initial total mass is 138 kg and, since it does not include a mass-expendable thrust system, its mass can be considered constant throughout the mission. The outer dimensions of this spacecraft are about 1 m x 0.8 m x 0.8 m (Figure 6.3). Table 6.1 summarizes Proba-V geometrical proprieties and the estimated inertias used to model it.

Geometry	
Shape	Cuboid
Mass	138 kg
Dimensions	1 m x 0.8 m x 0.8 m
J_{xx}	18.86 kgm^2
J_{yy}	14.72 kgm^2
J_{zz}	18.86 kgm^2

Table 6.1: Proba-V model geometric and inertial proprieties

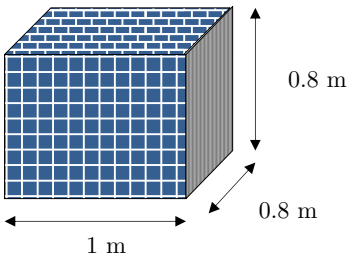

Figure 6.3: Proba-V model as implemented

The bus structure of Proba-V is composed of aluminum and CFRP panels. Three of its lateral faces are covered by GaAs photo-voltaic arrays with glass coating. Averaging the optical proprieties of the solar panels [**43**] and the aluminum panels [**44**] an approximated value is obtained. The results are shown on Table 6.2. The aerodynamic surface momentum transfer constants for Proba-V were not known, hence a normal accommodation is assumed (Table 6.3).

Optical Proprieties	
τ	0
ρ_a	0.7
ρ_s	0.3
ρ_d	0.0

Table 6.2: Proba-V model optical proprieties

Aerodynamic Proprieties	
σ_n	1
σ_t	0
$\frac{v_b}{\lvert v_\infty \rvert}$	0

Table 6.3: Proba-V model aerodynamic proprieties

The spacecraft was placed on its operational orbit on the 07/05/13 and has a nominal mission lifetime of 2.5-5 years. The initial orbital profile was reconstructed from the TLE of the spacecraft provided right after the deployment. The Two-Line Elements and the correspondent keplerian elements are shown, respectively, on Table 6.4 and Table 6.5.

```
PROBA-V
1 39159U 13021A   13130.11134104 -.00000110  00000-0 -29551-4 0   101
2 39159  98.7260 209.3311 0004852  47.9374 312.2220 14.22707777   425
```

Table 6.4: Proba-V TLE at BoL [26]

Initial Orbit	
Type	SSO
a [km]	7194.34
e	0.0004852
i [deg]	98.72
Ω [deg]	209.33
ω [deg]	47.937
υ [deg]	227.79

Table 6.5: Proba-V orbital parameters at BoL

Due to the high altitude and small dimension of the spacecraft, it can be assumed that no relevant natural deorbiting take place during its operative lifetime, and therefore the starting orbit for the simulated decay can be considered equal to the one provided on Table 6.5.

6.2.2 Ballistic coefficient and sail size

The ballistic coefficient is a central parameter in the estimation of the deorbit profile. Its value, when the sail is deployed, can approximated by

$$B_C = \frac{m_{sat}}{A_{sail} C_{D_{sail}}} \tag{6.1}$$

Checking Figure 5.6, the necessary ballistic coefficient value for a deorbit from around 800 km below 25 years is in the order of 20 kg/m^2. Running the 3DoF simulator for a deorbit simulation starting from the orbit of Proba-V and using a

range of ballistic coefficient of 2-20 kg/m^2 yields the results presented in Figure 6.4. There, on the left plot, the deorbit duration shown a function of the ballistic coefficient for two different initial solar cycle stages (high and low). The one on the right shows the corresponding year of re-entry. Here, due to lack of future solar data, real data from 1976-2015 was used instead.

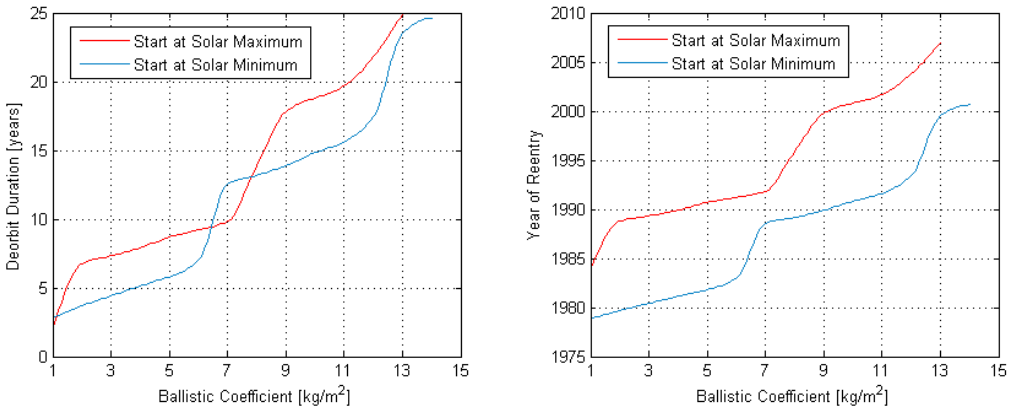

Figure 6.4: Deorbit time (left) and year of re-entry (right) from an 820 km altitude orbit, against ballistic coefficient

As expected, the higher the ballistic coefficient, the longer the time to deorbit. Moreover, because of the high initial altitude, the usual trend of deorbit duration with respect to solar cycle is inverted; in this case a descent started during a solar maximum lasts longer than the one started during solar minimum. This result is in accordance with what previously deduced from Figure 5.4. There is, however, a slight exception for B_C around 7 kg/m^2 for which an inversion of this trend is visible.

From the right plot, it is evident the alignment of the step-like trend of the two curves. The periodical change in slope is due to the different solar cycles stages at which the final part of the decay occurs. The shallow inclinations of the curve indicate a solar maximum moments while the steep slope a solar minimum. During a solar maximum a wider range of ballistic coefficients decay in a very similar duration, whereas during a Sun minimum solar level a much tighter range does not survive in orbit.

Considering the low fidelity of the 3 DoF simulator and the inevitable approximation errors related to the environment models, it has been decided to reduce the allowed deorbiting time for this study to 10/15 years. Figure 6.4 shows that the corresponding ballistic coefficients are in a range up to 8.3 kg/m^2. Another margin is here taken though: if a ballistic coefficient of 8.3 kg/m^2 is chosen and designed for, a very slight increase of the effective ballistic coefficient value results in a considerable extension of the deorbit time, especially for the solar maximum curve. Notice that an increase of the effective B_C of 10% places the deorbit 3 years after the intended 15 year limit. If the selected value is instead 7.5 kg/m^2, then such a drift in the effective value still results in deorbit within 15 years.

The lower limit of the ballistic coefficient range has to be imposed in function of the maximum allowable sail area. This value has been imposed, for mass and stowed volume reasons, equal to 50 m^2. Since the major aerodynamic contribution is generated by the sail, the system ballistic coefficient has been approximated with the sail C_D. The latter is assumed to be equal to the asymptotic value for a tumbling flat sail (as presented earlier in the analysis in Figure 5.20). This hypothesis is justified by the high initial orbit under exam. There, the deorbiting system (and therefore the sail) is expected to spin for most of the descent. For this reason the average drag coefficient of the entire system is approximated with a $C_D = 0.6$. With this value, the maximum area of 50 m^2 and Proba-V mass, the computed ballistic coefficient lower limit results $B_C = 4.5 kg/m^2$. The considered ballistic coefficients range is therefore between 4.5 and 7.5 kg/m^2.

Remembering the drag quotient definition, the ballistic coefficient can be written as

$$B_C = \frac{m}{A_{ref} C_D} = \frac{m}{Q_D} \tag{6.2}$$

Therefore, the drag quotient corresponding to the selected ballistic coefficient set has been computed. The resulting range is Q_D =[30.6; 19.4]The equivalent area range considering a tumbling C_D of 0.6 is around 30 to 50 m^2.

6.2.3 Sail shape and attachment point

As it was explained in the Analysis section, a 4-boom sail is the one that offers the best geometrical and robustness characteristics. The one here design shall be a square base sail.

For the selection of the sail angle Ω, the analysis performed in Chapter 5 has led to the conclusion that, overall, a flat sail seems to be the best trade-off between performance, weight and robustness.

The choice of the attachment point of the mast is limited mainly from the presence of the solar arrays. The centre of the top or nadir spacecraft face has been chosen. The mast is then assumed to be perpendicular to the satellite surface and aligned with the host CoM. Such alignment is determinant in maintaining the sail perpendicular to the flow when at its stable attitude.

6.2.4 Sail optical properties

In Section 5.3.3 the influence of the optical properties of the sail on the deorbit duration was assessed. As a result, it was found that there is a tendency for more opaque objects to deorbit faster than transparent ones from high altitude, highly inclined orbits and under solar minimum condition. However, these results should be strongly dependant on many factors as the initial attitude conditions, initial RAAN, ballistic coefficient of the object, etc.. Hence, such findings may not be fully applicable to the current design. Moreover, despite the apparent matching of the starting solar period, the actual operative life of Proba-V is not surely known, hence the real initial solar condition could be far from the above depicted scenario. The

lack of detailed information leads to a more conservative selection for this design parameter, for which an intermediate value is therefore assumed. This is made by considering a sail made of a transparent film which has been coated to provide an optical transmission coefficient τ of 0.5 and, hence, an equal fraction of interacting photons β. Recalling the CP1 membrane optical proprieties:

- Solar absorptance $\beta\varrho_a = 0.08$
- Solar reflectance $\beta\varrho_s + \beta\varrho_d = 0.09$

Imposing no diffusive reflection, assuming the ratio $\gamma = \frac{\varrho_s}{\varrho_d}$ to stay constant and setting $\tau = \beta = 0.5$, the resultant absorptance and reflectance coefficient are:

$$\begin{aligned} \varrho_s &= \frac{\gamma}{\gamma+1} = 0.5294 \\ \varrho_a &= \frac{1}{\gamma+1} = 0.4706 \end{aligned} \tag{6.3}$$

6.2.5 Mast length and flexibility

The mast length definition requires not only the results obtained in Chapter 5, but also a more 'systems engineering' approach. Indeed from the performed analysis, it seems that having a longer mast leads to better performances mainly due a wider stability range of the system. A greater stability margin makes the system less reactive to the disturbances, even if an excessive length can prevent a continuous realignment with the flow during the deorbit. However, it is obvious that a longer mast implicates a growth of the total system mass, reducing the benefits of this light-weight deorbiting solution. Also the introduced flexibility could worsen the both the dynamic behaviour inducing unpredicted attitude couplings and reducing the robustness of the system.

The selected mast lengths range has been chosen setting as lower limit the **[14]** solution of about $L = 0.5m$, while the upper limit has been computed by conservatively imposing a maximum mass of the sail deorbiting system equal to 5% of the total host mass **[15]**. Considering a 50m^2 sail (worst test case) and a contingency margin of 20%, the maximum admissible mast length, with standard section and material, is about 2 m.

Such mast length range boundaries have been used to study the mast flexibility effects on Proba-V. The system shall undergo the strongest stresses when in low orbit and for largest size of sail. The flexibility analysis here presented is then focused on these worst case conditions. The tested orbit is circular at 400km altitude, with a sail of 50 m^2 and, for being so low, neglecting the SRP forces (which are several orders of magnitude lower than the aerodynamic load). Initial Pitch and Yaw angles of 20° and 60°, respectively, have been imposed. This simulation has been performed with the 6 DoF Simulator with Flexibility, with a 4 GBEs mast model, where no torsion and elongation have been allowed.

Sensors were placed at the Mast-Satellite and Mast-Sail interfaces, measuring the reaction and torque forces at the extremities. Figure 6.5 and Figure 6.6 show the signals collected for a 0.5m long mast. As expected, at such low altitudes the aerodynamic force causes F_y to be the dominant reaction force. Moreover, the sail is subjected to higher aerodynamic contribution due to its large surface, which results in greater transverse reaction force components and lower bending moments at the mast interface.

The low magnitude of the reaction forces causes imperceptible mast tip displacement amplitudes in the order of nanometres, as Figure 6.7 shows.

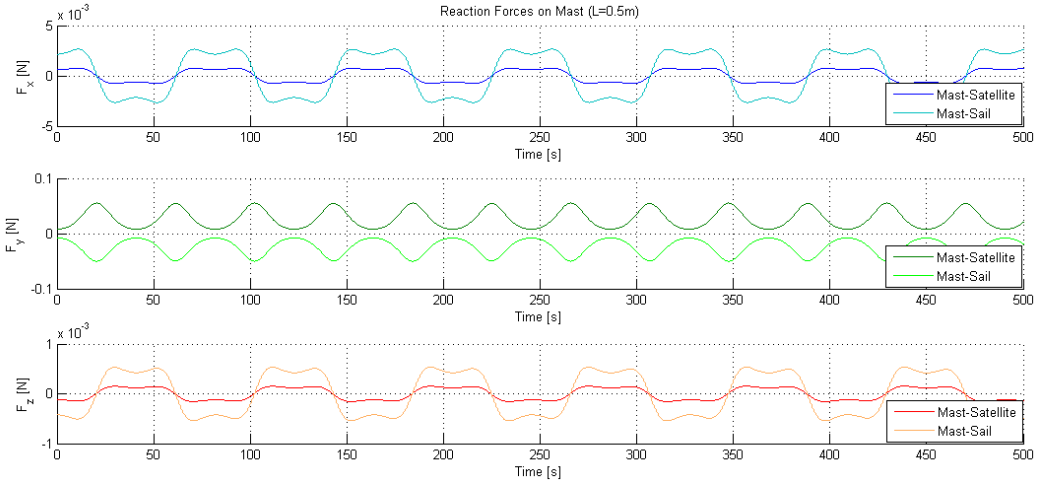

Figure 6.5: Reaction forces on the 0.5 m long mast extremities

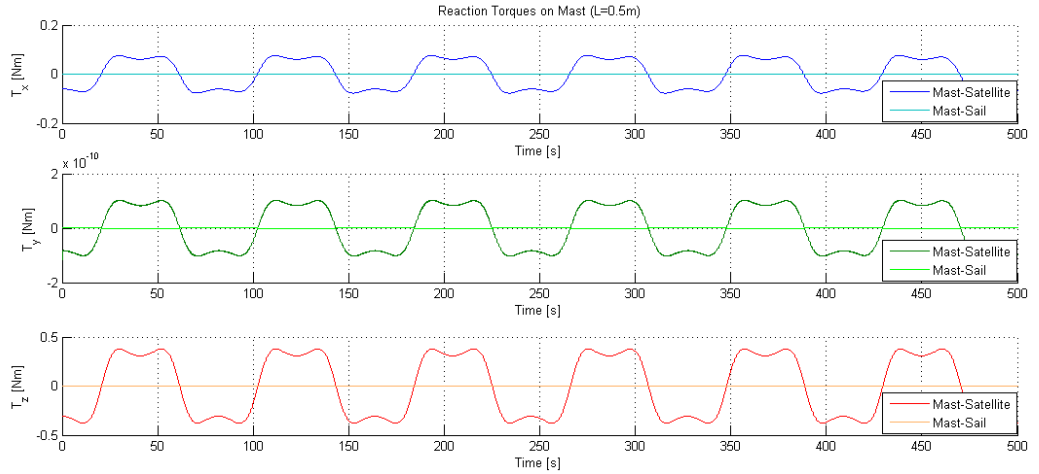

Figure 6.6: Reaction torques on the 0.5 m long mast extremities

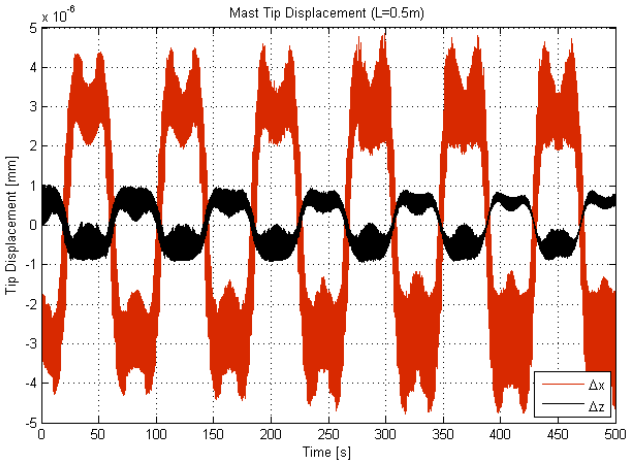

Figure 6.7: Tip displacement one the mast-sail interface respect to the undeformed configuration, for a 0.5m long mast

The same test has been performed for a 2 meter long mast. As deduced in Chapter 5 the longer mast the slower the system response. Indeed, the force and torque oscillations of Figure 6.8 and Figure 6.9 show a lower frequency with respect to the precedent case. The magnitude of the forces and torques involved are considerably higher. However, the mast tip displacement, also in this case, does not go above a micrometer (Figure 6.10). In the analogous test that has been described in Appendix A.3.1 during the validation of the 6 DoF simulator with flexibility the attitude profile for matched perfectly the one of a rigid system with similar tip deflection magnitudes. Hence, in the current simulation, the system motion is not expected be influenced by the flexibility for the mast length range considered.

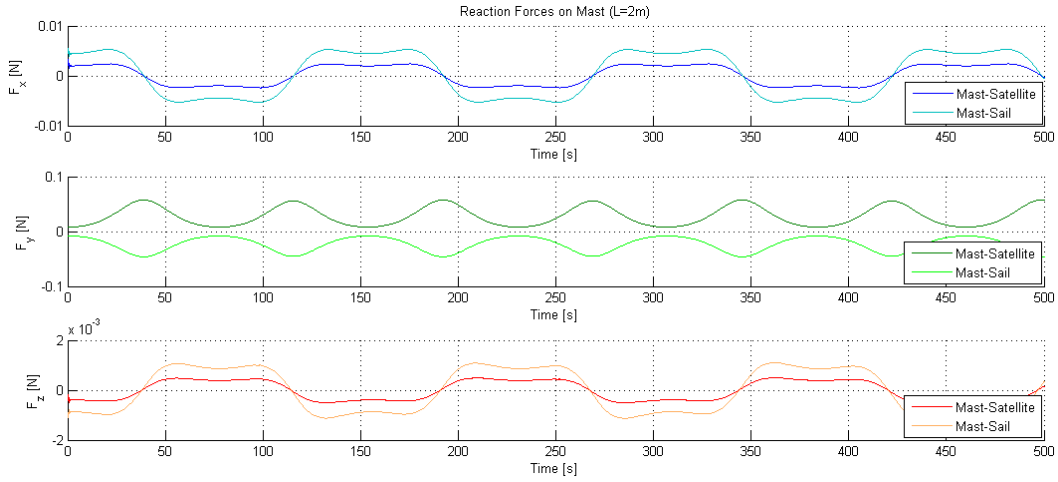

Figure 6.8: Reaction forces on the 2 m long mast extremities

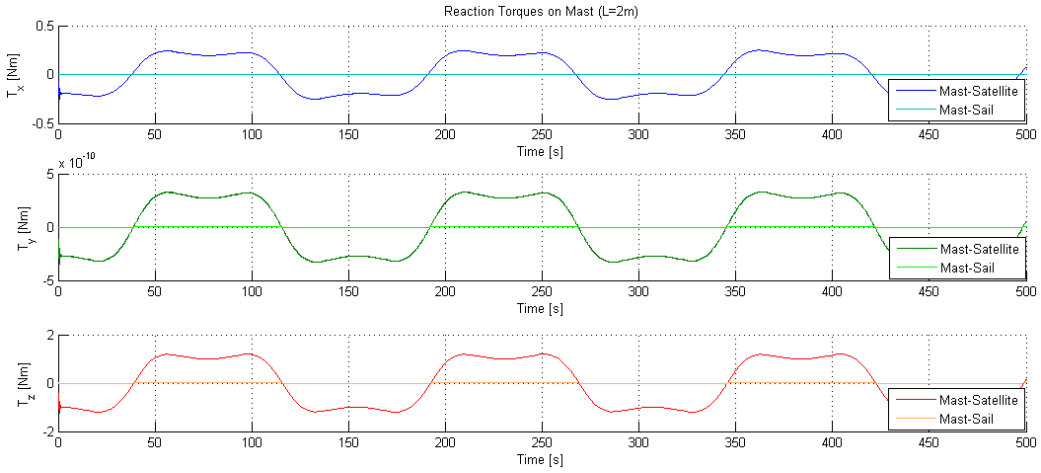

Figure 6.9: Reaction torques on the 2 m long mast extremities

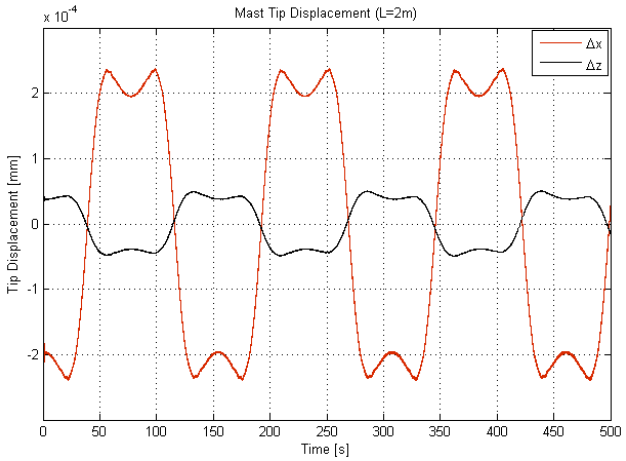

Figure 6.10: Tip displacement one the mast-sail interface respect to the undeformed configuration, for a 2m long mast

6.2.6 Overall sail system and mass budget

The designed Proba-V deorbiting system design is summarized on the following table.

	Parameter	Value
Mast	Shape	Hollow prism
	Section dimensions (h×w×t)	0.06m×0.0m6×0.003m
	Length	[0.5÷2.5] m
	Material	Aluminum 2024
	Density	2780 kg/m3
	Young's modulus	73.1 GPa

Sail	Shape	Pyramid
	Area	[30÷50] m2
	Ω	0
	Density	15.4 g/m2
	Optical proprieties	$\tau = 0.5$ $\varrho_a = 0.4706$ $\varrho_s = 0.5294$ $\varrho_d = 0.0$
	Aerodynamic proprieties	Typical solar sail

Table 6.6: Proba-V design characteristics

Table 6.7 summarizes the selected material mass proprieties for the deorbiting device:

Component	**Material**	**Density**
Sail	CP-1	15.4 g/m^2
Boom	CFRP	15 g/m
Mast	Al2024-T4	2780 kg/m^3

Table 6.7: Proba-V material proprieties

With these values and the designed parameter ranges, the mass budget is as follows

Component	**Minimum Mass**	**Maximum Mass**
Sail	0.46 kg	0.77 kg
Boom (x4)	0.23 kg	0.30 kg
Mast	0.96 kg	3.84 kg
Deployment mechanism	0.36 kg	0.60 kg
Total	2.01 kg	5.51 kg
Total w 20% margin	2.41 kg	6.61 kg

Table 6.8: Proba-V selected design mass budget

where the deployment mechanism mass has been scaled linearly (with respect to the sail area) from the one described in [**14**]. Moreover, due to the design maturity level, a contingency margin of 20% has been applied [**45**]. The resulting margined total mass respects the 5% of the host mass limit.

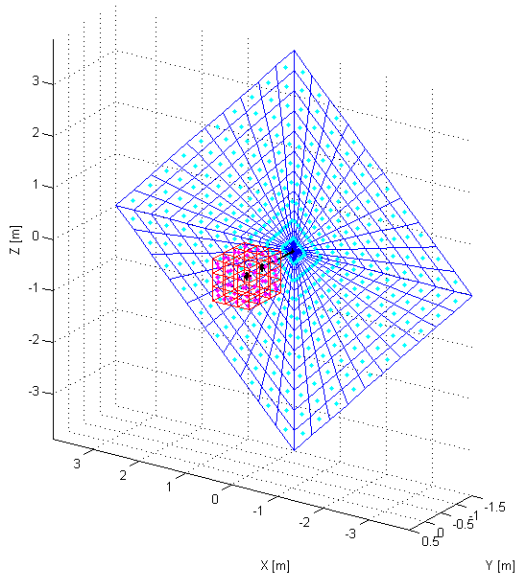

Figure 6.11: Proba-V deorbit configuration (30m² flat sail, 1 meter mast)

6.2.7 Full Deorbit 6DoF Test

Full deorbit tests or Proba-V with the 6 DoF simulator have been performed to better validate behavior of the system and to fully check the feasibility of the selected design for a realistic case.

The used initial orbital parameters are reported in Table 6.5. With these, six tests in total have been executed, changing one or more tunable parameter in each of them. Also the effect of the Solar Activity Level (SAL) has been analyzed, performing simulations both in maximum and minimum solar conditions. This choice has been done due to the impossibility to predict the exact Proba-V end-of-life moment; therefore the extreme conditions have been selected. The six cases analyzed and the correspondent parameters set are reported on the following table. In all these tests the initial attitude has been assumed to the stable one in RTN reference frame.

Case	SAL	A [m²]	τ	Ω [°]	L [m]
1	Max	30	0.50	0	1
2	Min	30	0.50	0	1
3	Min	50	0.50	0	1
4	Min	50	0.50	0	2
5	Min	50	0.50	10	1
6	Min	50	0.83	0	1

Table 6.9: Proba-V full deorbit tests summary

The possible comparisons between the simulations results have been here reported.

	Case 1	**Case 2**	**Case 3**
SAL	Max	Min	Min
A **[m]**	30	30	50
T_{est} **[years]**	13.00	13.00	5.47
T_{eff} **[years]**	18.02	13.82	5.86
Deviation [%]	38.62	6.31	7.13

Table 6.10: Proba-V full deorbit time deviation between 3DoF and 6DoF simulations

Table 6.10 shows the results for cases 1, 2 and 3, reporting the deorbiting times T_{est} estimated from Figure, in function of the ballistic coefficient, the effective deorbiting times obtained by simulation T_{eff} , and the deviation on these with respect to the estimated value. Notice that the studied sail areas corresponds to the limits of the area range considered. These correspond to the ballistic coefficient range boundaries of $B_C = 4.5$ and $B_C = 7.5$. As expected, a bigger area led to a faster deorbiting. For different solar conditions (constant sail area) the results showed more than 5 years of difference. The estimated orbit time of cases 1 and 2 was 13 years, but from Figure 6.4 it is clear that, depending on the initial solar level, the solar activity period in which the re-entry occurs, presents very different B_C *vs* time slope profiles. As previously explained, a shallow slope corresponds to a solar maximum period, while a steep one to a solar minimum. A small offset in the effective ballistic coefficient for a re-entry during a solar minimum, results in a much larger deviation of the deorbiting time. As a confirmation of this, the effective ballistic coefficients in cases 1 and 2 are respectively 9.1 and 8.9 kg/m^2, corresponding to deviations of 21.3% and 18.6%. Despite such a small difference in the ballistic coefficient deviations, the two resulting deorbiting times show a much higher discrepancy with respect to the expected value.

A series of confrontations between the analyzed cases under solar minimum conditions is here performed. Note that case 3 has been used has reference for the computation of the effective time deviations.

Table 6.11 reports a confrontation on the deorbiting time between two different sail area values. It can be observed that, in the tested configuration, a decrement of 40% of the area led to a increase of deorbiting time of around 136%.

	Case 3	**Case 2**
A **[m^2]**	50	30
T_{eff} **[years]**	5.86	13.82
Deviation [%]	135.83	

Table 6.11: Proba-V full deorbit deviation for different sail areas

Table 6.12 shows instead that, doubling the mast length, the deorbiting time is subjected to an increment of 1.54%. The increase in mast length resulted in a performance worsening, however such a small difference does not allow to draw a solid conclusion. In Chapter 5 the performed analysis on the mast length showed a

slight trend opposite to what obtained in this test. This shows that the influence of the mast length on the performance of deorbit is not at all linear. It therefore requires extensive orbital testing in a variety of conditions to allow a solid understanding.

	Case 3	**Case 4**
L **[m]**	1	2
T_{eff} **[years]**	5.86	5.95
Deviation [%]	1.54	

Table 6.12: Proba-V full deorbit deviation for different mast length

In Table 6.13 the results on tests with different Ω are presented. In accordance with the previous analysis studies, a flat sail leads to slightly better performances in terms of deorbit time.

	Case 3	**Case 5**
Ω **[°]**	0	10
T_{eff} **[years]**	5.86	6.07
Deviation [%]	3.58	

Table 6.13: Proba-V full deorbit deviation for different Ω

As last test, the deorbiting time obtain obtained for two different transparency sail proprieties is reported. As already stated in previous chapters, under the analyzed orbital and solar conditions, the role of the optical proprieties on the deorbit performances is not trivial to state. Indeed, despite a better result obtain with $\tau = 0.5$, the deviation cannot lead to conclusive considerations.

	Case 3	**Case 6**
τ	0.5	0.83
T_{eff} **[years]**	5.86	6.16
Deviation [%]	5.12	

Table 6.14: Proba-V full deorbit deviations for different sail optical proprieties

The altitude evolutions corresponding to these 6 cases run are show in Figure 6.12.

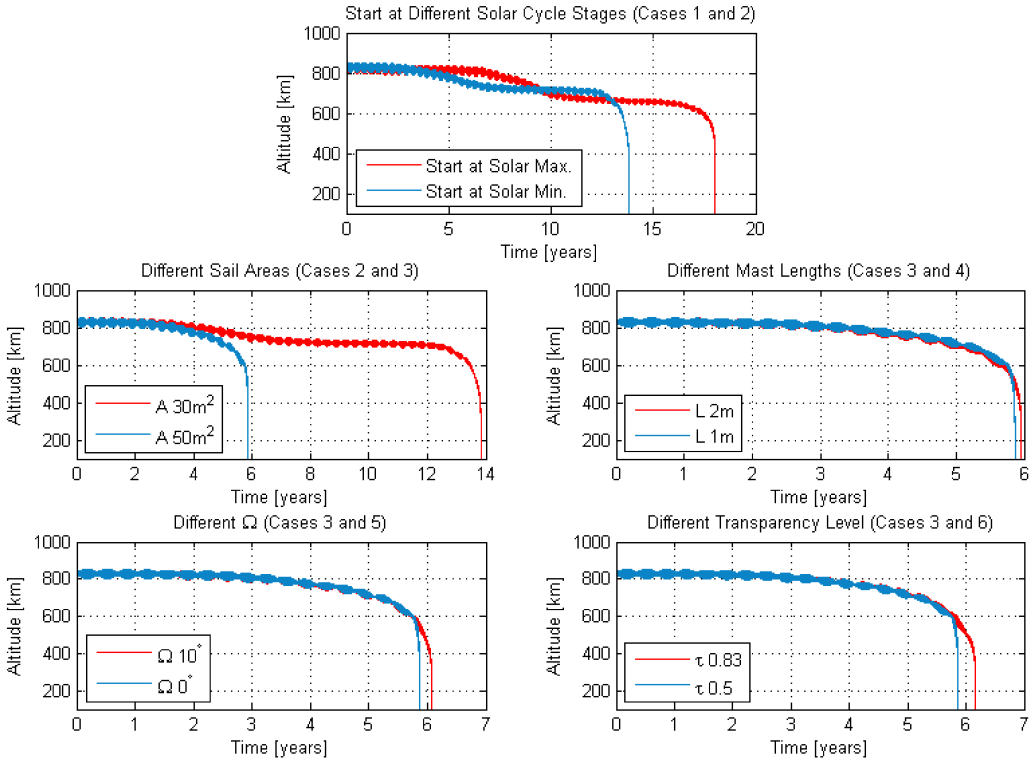

Figure 6.12: Altitude evolutions for the Proba-V full deorbit runs

6.3 AVUM at EoL

AVUM is the multiple-burn upper stage of Vega launcher. It can be equipped with a single or a multiple payload adapter, depending on the mission objective. The case under study provides for the deployment of the main payload (Proba-V) and of other two secondary probes, and therefore a multiple payload adapter is required (VESPA). AVUM and VESPA single designs are showed in Figure 6.13 and their assembly is visible in Figure 6.1.

In the VV-2 mission, after successfully deploying Proba-V, Vega's upper stage performs a burn before the top half of VESPA is ejected [**42**]. Another burn is then initiated to circularize the orbit at a lower altitude where the secondary payloads are deployed. Finally, a last burn places the spent AVUM with the VESPA boat tail still attach on a trajectory

AVUM in VV-2 mission, delivers Proba-V on its operational orbit, and it also release the upper part of VESPA in order to expose the secondary payloads. After a burn to change orbit and reach the secondary payloads release position, the AVUM with the VESPA boat tail still attach, perform a last burn to deorbit. AVUM configuration at EoL, therefore, includes an extra mass given by the lower part of VESPA, which changes also the inertial and aerodynamic characteristic of the debris.

Despite a propelled deorbit strategy has been provided for AVUM, the drag-sail option has been analyzed in this research to highlight the possibility of a relevant mass saving with a passive solution. Furthermore, without a propelled manoeuvre, AVUM deorbit would not occur within the 25 years limit.

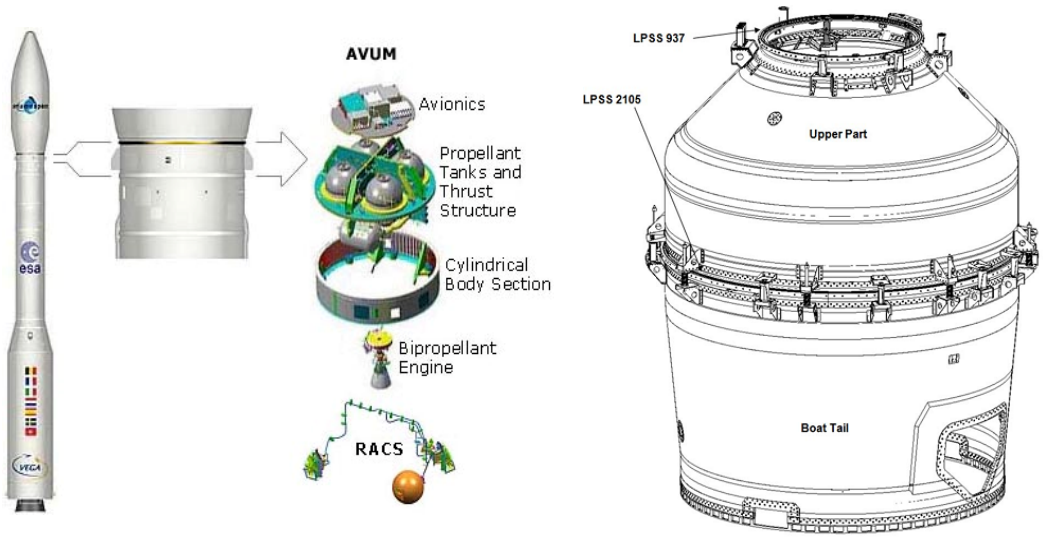

Figure 6.13: AVUM configuration (left) and VESPA (right) [40]

6.3.1 Model

The AVUM EoL configuration is more articulated respect to the Proba-V one and it can't be simply modelled with the basic solid shapes implemented in this simulator version. Therefore AVUM was here modelled as a cylinder with the dimensions provided in Table 6.15.

The external surface of the configuration AVUM and Vespa at EoL is almost completely composed by aluminum panels with black coating; therefore it is assumed a material with high absorbance proprieties (Table 6.16). Due to lack of information on the aerodynamic surface momentum transfer constants for AVUM a normal accommodation was assumed (Table 6.17).

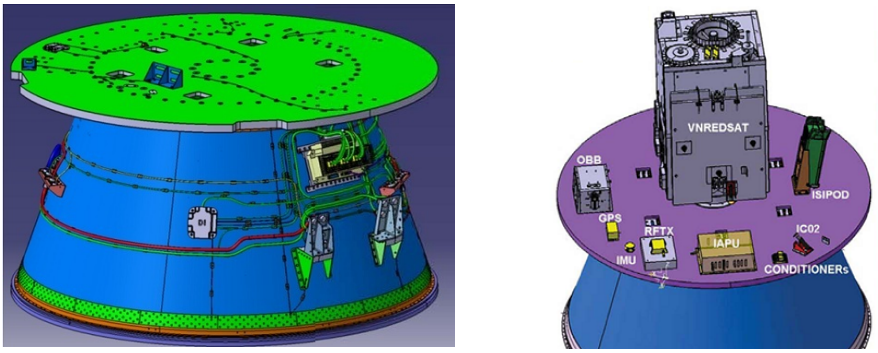

Figure 6.14: VESPA internal adapter [40]

Geometry	
Shape	Cylinder
Mass $[kg]$	830
Height $[m]$	1.95
Radius $[m]$	0.9875
J_{xx} $[kgm^2]$	520
J_{yy} $[kgm^2]$	440
J_{zz} $[kgm^2]$	520

Table 6.15: AVUM model geometrical and inertial proprieties

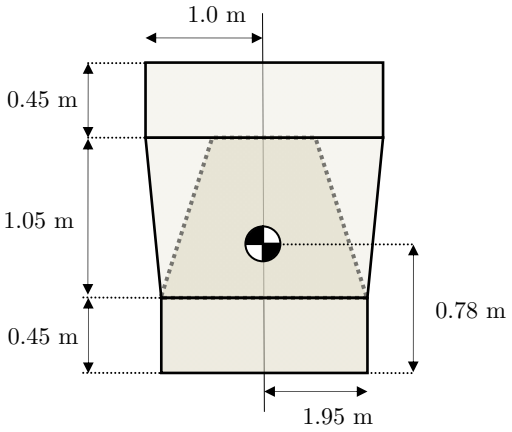

Figure 6.15: AVUM at EoL diagram

Optical Proprieties	
τ	0
ρ_a	0.8
ρ_s	0.2
ρ_d	0.0

Table 6.16: AVUM optical proprieties

Aerodynamic Proprieties	
σ_n	1
σ_t	0
$\frac{v_b}{\lvert v_\infty \rvert}$	0

Table 6.17: AVUM model aerodynamic proprieties

To estimate the initial orbit on which AVUM begins its descent, the first TLE of the payload VNREDSAT-1 has been used. It follows the mentioned data and the relative orbital parameters.

```
VNREDSAT-1
1 39160U 13021B   13128.52182430  .00005798  00000-0  10499-2 0    70
2 39160  98.1321 206.9901 0001926  25.3828 334.7400 14.66697732   190
```

Table 6.18: AVUM TLE at EoL [26]

Initial Orbit	
Type	SSO
a	7049.76km
e	0.0001926
i	98.13°
Ω	206.99°
ω [deg]	25.38°
υ [deg]	205.26°

Table 6.19: AVUM orbital parameters at EoL

6.3.2 Ballistic coefficient and sail size

As it was done for Proba-V, the design process of a drag sail device for AVUM starts by analysing the decay from its nominal orbit. Figure 6.16 depicts the deorbiting time from the orbit of AVUM for different ballistic coefficients for a start at low and at high solar activity. Again, due to lack of extensive predicted future solar data, values from 1976-2015 were used instead.

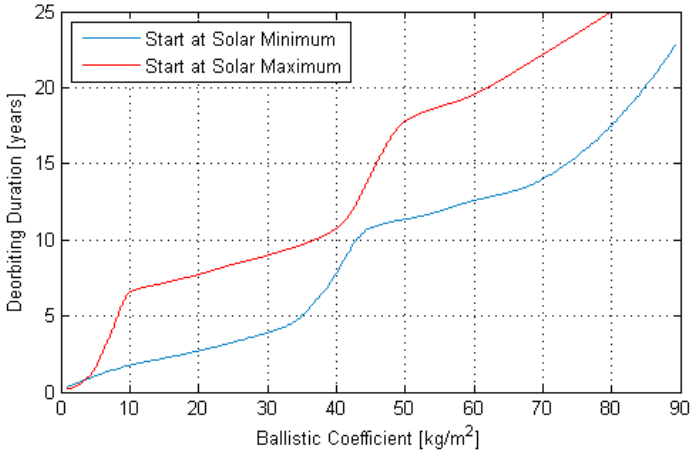

Figure 6.16: Deorbit time from AVUM's orbit as function of the ballistic coefficient

The difference between a deorbit starting at opposite solar cycle stages is even greater than for the Proba-V case. This was expected since this is a lower orbit. The deorbit duration from a start at high solar activity is here consistently longer than for a low activity one. Indeed for a departure at solar minimum most of the lower range of ballistic coefficient decays within 5 years, i.e. at the first solar maximum encountered. For a start at the maximum, since the spacecraft starts high enough to survive the high cycle moment at which it begins the descent, this same range only finishes its decay between 5 and 10 years. Again it is possible to perfectly distinguish in the plotted curves the steep and shallow slopes of low and high solar periods, respectively.

As before a deorbit time ceiling of 10-15 years is aimed at. Differently from the Proba-V case, in which the deorbit start was somehow uncertain due to possible extension of the mission duration, in the case of AVUM this epoch shall be perfectly known. Such leads to a much better knowledge of the solar conditions AVUM would be exposed to at the start of its journey. Of course a large uncertainty level would still persist since future Sun cycle evolution predictions carry a great deal of error. Still, in the case of AVUM it is possible to assume that, if a specific deorbit time is desired, a sail with specific dimensions for the solar conditions at hand shall be selected for the flight. Two upper limits for the sail size are then here discussed: one for a start the solar high, and one for a start at solar low.

For a decay beginning during solar high peak, if a 10-15 year descent is desired a ballistic coefficient lower than 45 kg/m^2 is necessary. However, to aim exactly at a 15 year deorbit means that the spacecraft would re-enter during a solar minimum which, in the curve, represents a high slope of B_C *vs* Duration. Such steep slope, together with the uncertainty around the plotted curve and the actual equivalent ballistic coefficient of the falling object, would very easily result in a large drift of the deorbit duration. In practice, this means that a deorbit programmed to finish during solar minimum is much less robust than one programmed to end at solar maximum. This is intuitive since at solar minimum the density levels are so low that a slight increase of the effective ballistic coefficient can mean survival of the object in orbit until the next maximum. A way to make the design more robust is then to aim at a deorbit around a solar high period. A maximum ballistic coefficient of 35 kg/m^2 is then selected. For this figure, a deviation of 30% still places the deorbit duration within 15 years, representing a delay of 35%.

If the deorbit trajectory shall start at a solar minimum a look at Figure 6.16 gives a maximum ballistic coefficient of around 70 kg/m^2. This amount should make the spacecraft re-enter almost exactly at the end of a solar maximum, which, although better than the previous case, is not the most robust scenario. A ballistic coefficient value of 60 kg/m^2 shall then be considered, for which a deviation of 30% means only a delay of 15% (still resulting in deorbiting within 15 years).

The minimum ballistic coefficient, similarly to the Proba-V case, is constrained by size, mass and accommodation limits, as well as by mechanical design limits. These constraints are extremely difficult to grasp at such a study design concept level. For the previous design exercise a 50 m^2 system was considered as maximum size. Here, such a system size, assuming a conservative average C_D of 0.6 like before, should result in a deorbit within 3.6 years for start at low-solar and around 8.7 years starting at high-solar. AVUM, however, is a much larger spacecraft than Proba-V, being able to accommodate a considerably larger deorbit device. A sail of 100 m^2, for example, would not be unrealistic. These dimensions would decrease the effective ballistic coefficient 50%, respectively. However, the resulting decrease in decay duration would not have the same relative proportion, being of about 1-1.5 years in both cases. Due to lack of both system and operational knowledge of AVUM it shall be here assumed that such a reduction of deorbit duration does not compensate the further increase of the sail device size beyond 50 m^2. This is then maximum considered dimension for the sail system here designed and shall represent a ballistic coefficient of around 28 kg/m^2.

Table 6.20 summarizes the system dimensions and deorbit durations discussed above. A conservative C_D of 0.6 was used to convert ballistic coefficient values to equivalent sail size. This approximation shall be verified further in this document.

	Minimum Sail Size		Maximum Sail Size
	Solar Min	Solar Max	
B_C [kg/m^2]	60	35	28
Area [m^2]	23	40	50
T_{est} [years]	12.6	9.6	3.6 (Solar Min) 8.7 (Solar Max)

Table 6.20: Proposed sail sizes for AVUM deorbit

6.3.3 Telescopic mast position and sail orientation

The choice of the telescopic mast attachment point for AVUM requires a careful analysis due to its irregular shape.

As it was done for Proba-V, the mast-sail device shall be aligned with the CoM of the system. This is an important constraint since a misaligned sail does not present its maximum cross sectional area to the flow at the stable attitude, not producing its maximum drag. Figure 6.17 exemplifies the loss of C_D performance resulting from a sail axis misalignment with respect to the satellite CoM. A misalignment would create much larger bending loads on the mast than the ones studied until now. For these reasons a Sail-Satellite configuration with a CoM misalignment assembly is discarded.

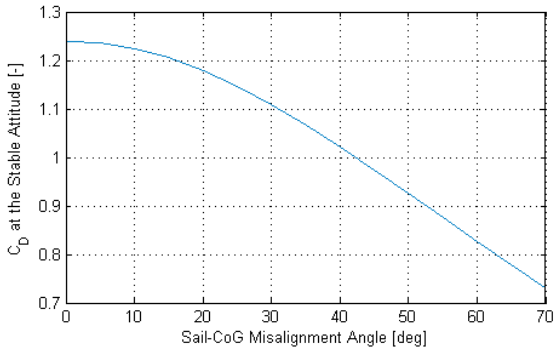

Figure 6.17: Drag coefficient in function of sail misalignment

The connection point should also be careful looked at, as simply choosing it in the outer surface of the VESPA is not feasible because of the tight space that exists between the adapter and the fairing. Due to the engine nozzle on the bottom side of AVUM, also this surface is not accessible. The only remaining possibility is therefore the adapter internal platform. As shown in Figure 6.14, the center of the platform space is occupied by one of the secondary payloads (VNREDSAT). This forces the sail system to be installed in a decentred position, requiring the mast to be deployed at an angle relative to the platform in order to comply with the necessary CoM alignment.

The proposed assembly position lies between one of the faces of the payload (VNREDSAT) at a distance of Δx of the platform center. For this study AVUM is considered axisymmetrical, hence the attachment position point is arbitrarily

chosen to lie on the X half positive plane ($z = 0$, $x > 0$) of the spacecraft (Figure 6.18). The distance Δx , however, shall be carefully selected.

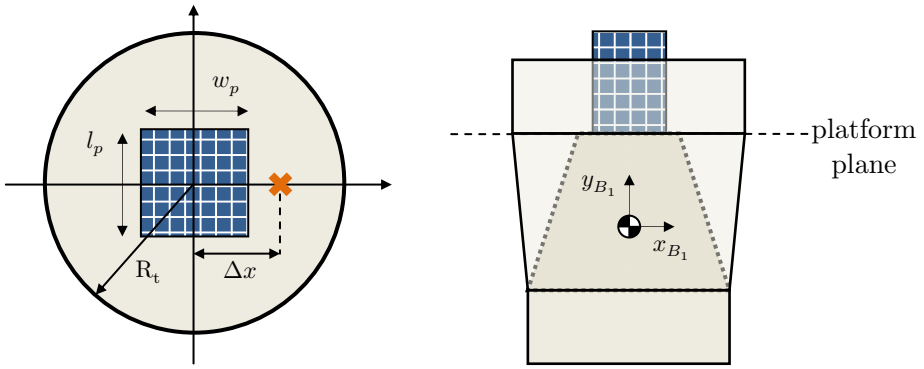

Figure 6.18: Payload platform and attachment point diagram

The distance Δx is constrained not only by the width of the payload and the radius of the platform, but also by the height of the boat tail of VESPA (the top cylindrical piece visible in Figure 6.15). Taking in account the dimensions shown on Figure 6.19, the range of Δx is

$$\Delta x_{\min} = \frac{w_p}{2} \ , \qquad \Delta x_{\max} = \frac{R_t b}{a+b} \qquad \Rightarrow \qquad 0.3 \text{ m} < \Delta x < 0.62 \text{ m} \tag{6.4}$$

which constrains the angle of the mast ϑ to the limits

$$\vartheta_{min} = 0 \ , \qquad \vartheta_{max} = \arctan\left(\frac{R_t}{a+b}\right) \qquad \Rightarrow \qquad 0 < \vartheta < 40.5^{\circ} \tag{6.5}$$

The minimum length of the mast is also constrained by the top part of the boat tail of VESPA as the sail shall be 'outside' this upper cylinder when deployed. A second constrain on the length of the mast is the size of the payload sharing the platform with the sail device. In the unlikely situation of failed release of this payload the capability of the upper stage to still deorbit must be guaranteed. In that sense, the sail shall be able to successfully deployed with the payload in its original position. These two limits on L , depicted in Figure 6.19.

$$L_{min} = \max\left(L_{min,Vespa}, L_{min,payload}\right) \tag{6.6}$$

These limits are function of the attachment point Δx as

$$L_{min,Vespa} = \frac{1}{\sqrt{\Delta x^2 + b^2}}\left[\Delta x\left(R_t - \Delta x\right) + ba\right] \tag{6.7}$$

$$L_{min,payload} = \frac{1}{\sqrt{\Delta x^2 + b^2}}\left[\Delta x\left(\frac{w_p}{2} - \Delta x\right) + bh_p\right] \tag{6.8}$$

The evolution of these limits as well as the value of ϑ along Δx is shown on Figure 6.20.

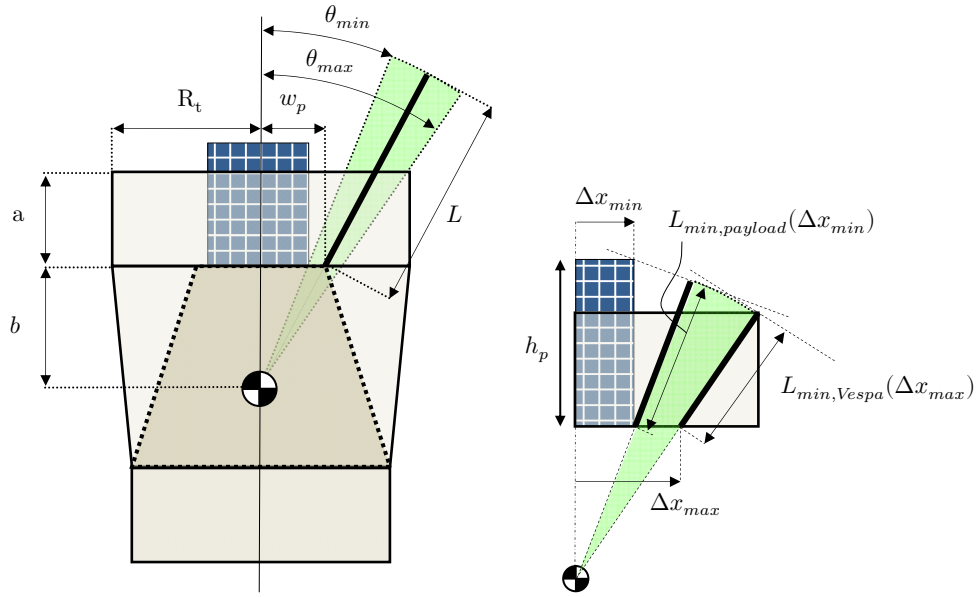

Figure 6.19: Attachment point limits

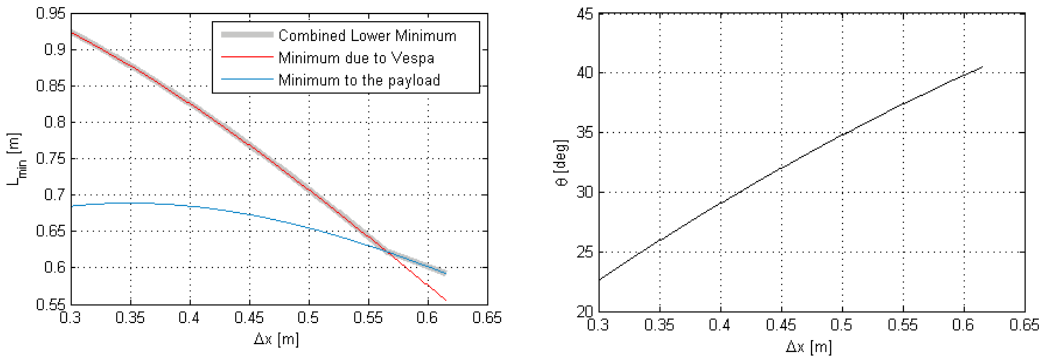

Figure 6.20: Minimum length and attachment angle as function of Δx position.

It is visible that around $\Delta x = 0.57$ the two limits for the mast length cross creating a transition in the combined limit curve. The assembly angle ϑ grows approximately linearly between 22.6 and 40.5 within the range of Δx .

6.3.4 Stable equilibrium attitude

As explained in the previous section, the assembly of the drag sail device on AVUM cannot be done along one of the main geometry axis of the upper stage. This most surely results in a stable equilibrium attitude which is not aligned with one of the spacecraft body axes. Furthermore, due to the odd alignment, there might be an aerodynamic moment generated by the upper stage that prevents the stable attitude of the overall system from coinciding with the sail-mast axis. It is

important then to check for possible misalignment and its consequence on the system nominal performance.

The alignment angle between the stable equilibrium attitude and the sail-mast axis was observed for different values of sail area, Δx , and mast length. While Δx and mast length were found to have minimal effect on this alignment angle, the results from function of the sail area are depicted in Figure 6.21 due to its relevance. The drag coefficient for the stable orientation is also presented in comparison with the maximum value for the configuration.

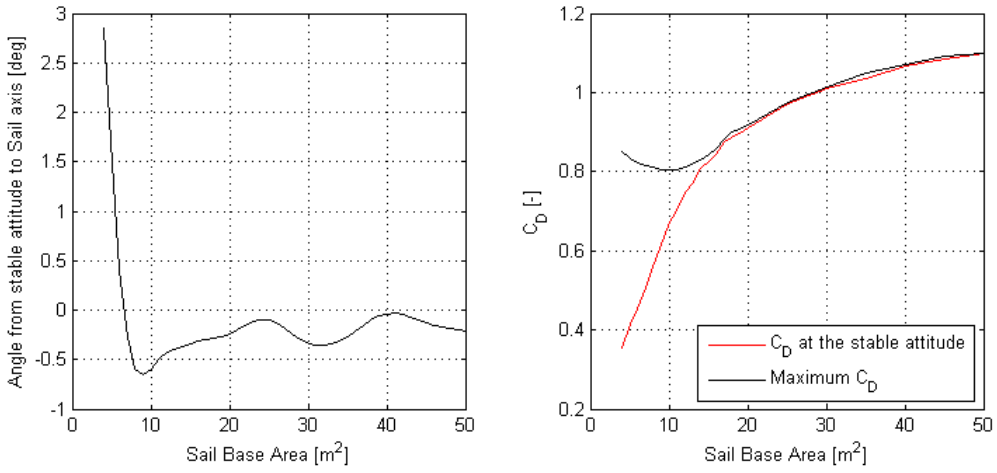

Figure 6.21: Angle between stable attitude and sail-axis and C_D as stable attitude as function of the sail base area.

The sail area is by far the parameter that most influences the stability attitude offset from the sail-mast axis. However, for the range of areas considered for the current design (20 to 50 m^2) the deviation is very small and mostly driven by the numerical error caused by the discretization of the surface. Indeed, the C_D obtained at the stable attitude for this range of areas is practically coincident with the maximum value.

6.3.5 Aerodynamic quotients

The drag and restoring torque aerodynamic quotients considering different values of area, mast length and attachment point are here presented.

Figure 6.22 shows the drag quotient and restoring torque quotient in function of Yaw and Pitch for different areas of sail, Figure 6.23 for different Δx values and Figure 6.24 for several lengths of the mast. The Yaw here used is offset an angle equal to ϑ from the longitudinal axis of the satellite so that the 0 Yaw angle coincides with the mast direction. The Pitch evolution shown is for Yaw=0. All quotients are adimensinalized by A_{ref} (being equivalent to coefficients) to allow comparison among different sails.

A lower area (23m^2) results in a slightly lower drag coefficient, especially around the stable attitude. The larger sails show very similar performances for all orientations. The torque coefficients are virtually the same for all three sizes.

Changing the attachment point distance to the centre of the payload platform from 0.3 m to 0.6 m results in a slight decrease of the drag coefficient around the stable attitude. The differences in torque coefficient are also very slight, having a higher peak torque around the Yaw axis the configuration with $\Delta x = 0.6$ m and higher maximum torque around the Pitch axis the one with $\Delta x = 0.3$ m.

The largest differences in the coefficients shown happen for different mast length: a larger length results in a considerably higher torque around both Yaw and Pitch axes. This is in line with the findings of the Chapter 5.

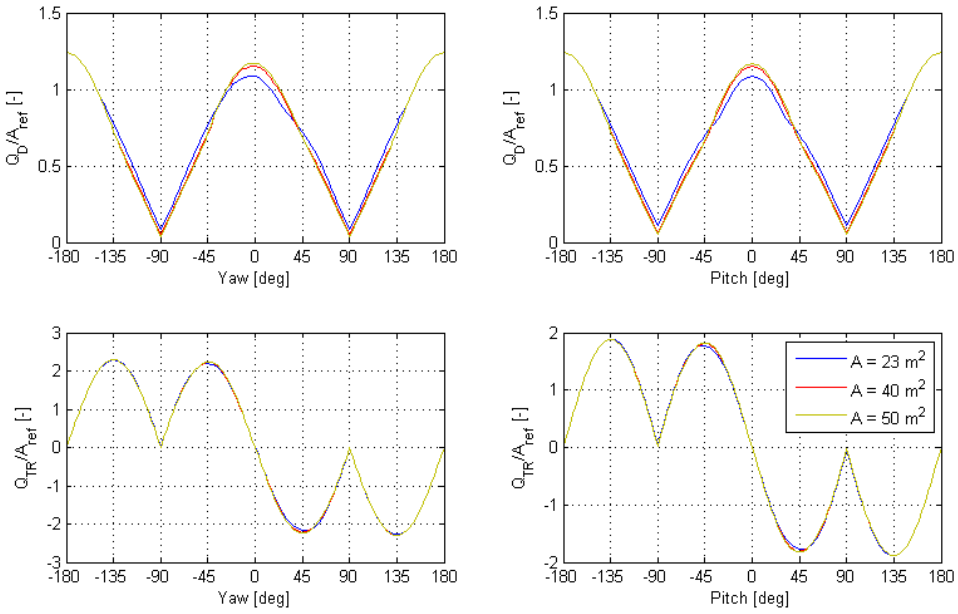

Figure 6.22: Drag quotient and restoring torque quotient in function of Yaw and Pitch for different sail base areas

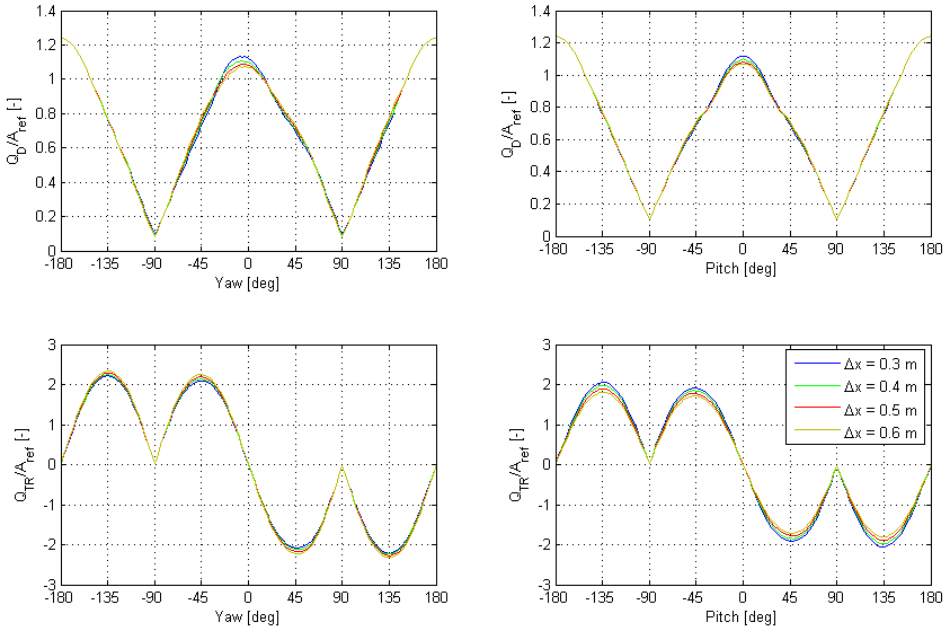

Figure 6.23: drag quotient and restoring torque quotient in function of Yaw and Pitch for different attachment positions

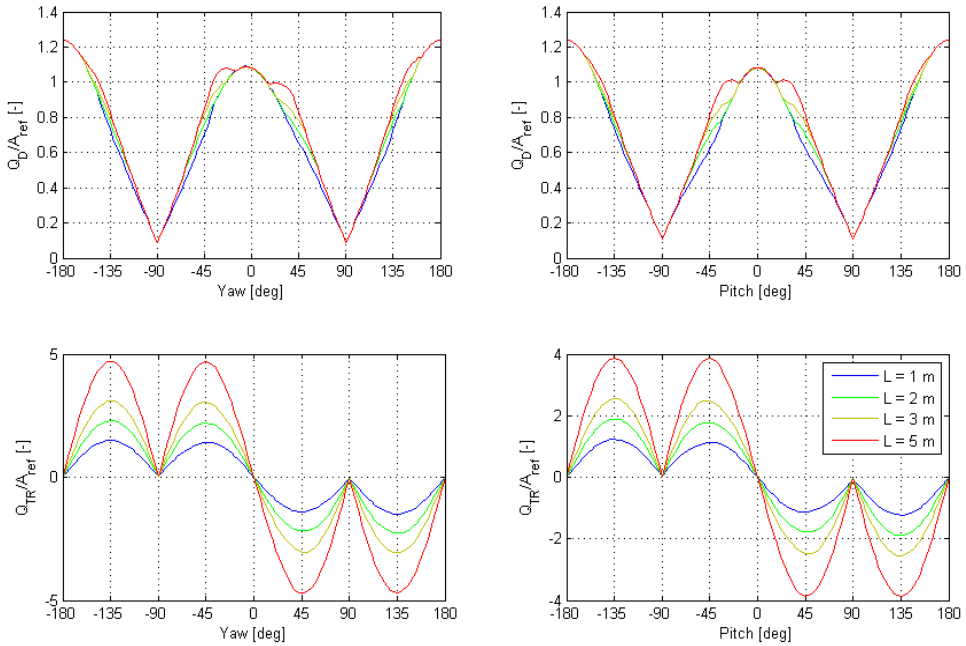

Figure 6.24: drag quotient and restoring torque quotient in function of Yaw and Pitch for different mast lengths

6.3.6 Sail geometry choice

To allow a proper choice of the attachment point, the average drag coefficient for different Δx was recorded for dynamic tests starting with initial angular velocity. The results are presented in Figure 6.25.

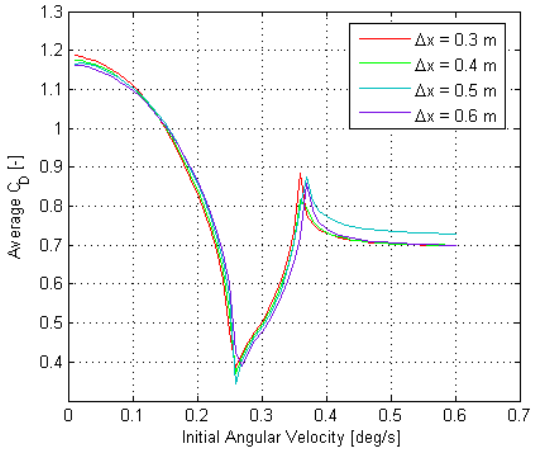

Figure 6.25: Average C_D for different Δx as function of initial angular rate

It is visible that the attachment point position changes only very slightly the average C_D, especially for low initial rates. During tumbling, a Δx of 0.5 m seems to perform a notch better than the remaining values.

Given the slight advantage shown by the Δx of 0.5 m this value has been selected. Additionally to the performance demonstrated, this value is close to the middle of the possible range (0.3 to 0.6 m) offering good separation distance from both VESPA tail boat top edge and payload. One should note that, although not studied in detail, the extreme values of this range would not have been achievable in the real design, as the attachment point calculation were done neglecting the width of the mast (which is 3 cm). For the 0.5 m Δx there is, however, enough distance between mast centre line and boat tail edge (around 15 cm) to allow good accommodation of the mast width.

It has been seen previously seen in this document that a longer mast, in general, increases the stability properties of the system, however the upper limit for this dimension is inevitably set by implementation and assembly issues (size, mass, storage method, etc.). The scope of this document does not cover the level of detail necessary to define a real limit for this configuration parameter. Therefore, in an attempt to stay within a feasible set of design dimensions, the length of the mast has been conservatively chosen as 2 m, in line with what has been done for the Proba-V study.

6.3.7 Mass budget

The designed Proba-V deorbiting system design is summarized on the following table.

	Parameter	Value
Mast	Shape	Hollow prism
	Section dimensions (h×w×t)	0.06×0.06×0.003 m
	Length	2 m
	Material	Aluminum 2024–T4
	Density	2780 kg/m3
	Young's modulus	73.1 GPa
Sail	Shape	Pyramid
	Area	[23; 40; 50] m^2
	Ω	0
	Density	1540 kg/m^3
	Optical proprieties	$\tau = 0.5$ $\varrho_a = 0.4706$ $\varrho_s = 0.5294$ $\varrho_d = 0.0$
	Aerodynamic proprieties	Typical solar sail

Table 6.21: AVUM design characteristics

Table 6.22 summarizes the selected material mass proprieties for the deorbiting device:

Component	Material	Density
Sail	CP-1	15,4 g/m2
Boom	CFRP	15 g/m
Mast	Al2024-T4	2780 kg/m3

Table 6.22: AVUM material proprieties

With these values and the designed parameter ranges, the mass budget is as follows

Component	Small Sail (23 m^2) Mass budget	Medium Sail (40 m^2) Mass budget	Large Sail (50 m^2) Mass budget
Sail	0.35 kg	0.62 kg	0.77 kg
Boom (x4)	0.20 kg	0.27 kg	0.30 kg
Mast	3.84 kg	3.84 kg	3.84 kg
Deployment mech.	0.28 kg	0.48 kg	0.60 kg
Total	4.67 kg	5.21 kg	5.51 kg
Total w 20% margin	5.60 kg	6.25 kg	6.61 kg
Saving compared to deorbit propellant*	92.6%	91.7%	91.3%

Table 6.23: AVUM selected designs mass budget

* The AVUM missions include an EoL deorbit burn manoeuvre to decrease the orbital perigee of the upper stage enough to force its re-entry. The propellant for this burn is naturally accounted for in the mass budget of the vehicle and amounts to about 75.7 kg. This value was here obtained for a burn duration of 95.7 s, a thrust of 2450 N and an engine I_{sp} of 315.5 s [**46**].

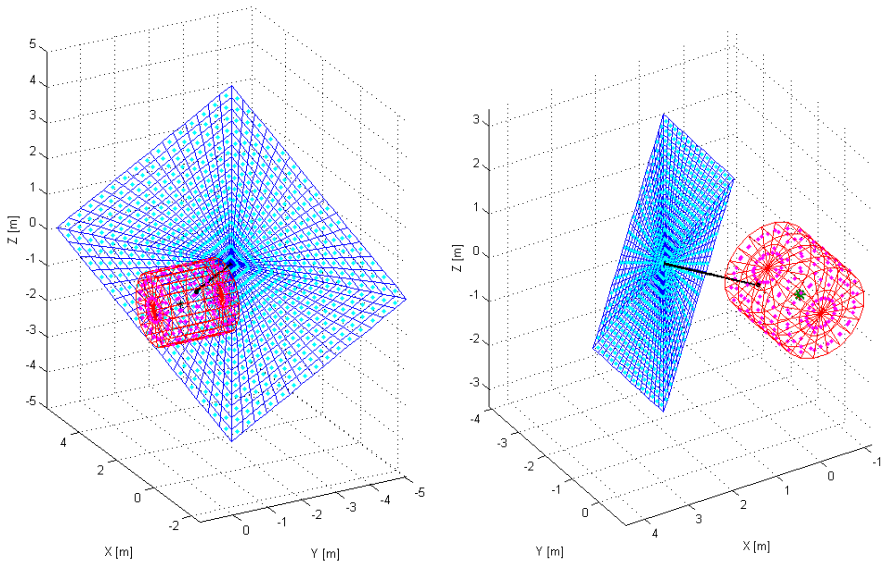

Figure 6.26: Simulation models of AVUM deorbit configurations, 50m^2 (left) and 23m^2 (right)

7 Conclusions

In this research the theme of drag-sail assisted deorbit has been investigated. The theoretical fundamentals behind LEO environment, orbital and attitude dynamics and geometrical proprieties of deorbiting sails have been carefully studied. With the acquired background a set of orbital decay simulation tools was developed, including an NRLMSISE-00 atmosphere model, a zonal harmonics gravity and SRP. Spacecraft and sail surface geometry models were built considering the shielding and intershilding phenomena for both flow and light body interactions. Flexible satellite-sail connection behaviour was also integrated in the software environment.

By means of these simulation algorithms the role of the environment on the system decay has been analysed as well as the influence of the geometry on the attitude behaviour, and its effect on the deorbit profile. Finally, based on the analysis outcome, a preliminary design of two real test cases was performed.

From the conducted analysis, a higher orbital inclination results in a lower average aerodynamic action, mainly due to a solar-induced high density diurnal equatorial zone. The solar influence on the atmosphere, being cyclic, causes deorbit duration to change according to the period at which it is performed; for lower orbits deorbiting duration shows a counter-phase relation with the solar flux variation, while for higher orbits this trend is inverted.

The drag-sail shape that shows the best trade-off between efficiency and robustness was found to be the squared base one. From this class of sails, the stronger damping effect and higher drag coefficient achievable with a flat sail indicate that this design, despite having null side drag and showing slower dynamics, is preferable over the pyramidal sail. Orbital testing at a wide range of altitudes corroborated the analysis, showing considerably improved performance of the flat sail with respect to pyramidal ones.

A larger sail proved, not only to shorten deorbiting times as it would be expected, but also to decrease the relative magnitude of the intershielding interactions between satellite and sail. Such interactions showed non-negligible importance over all the considered altitudes. On the other hand, wider sail inevitable has higher probability of impact with other orbital debris. It has been observed that, in case of collision, the hole produced causes (not accounting for momentum variations) considerable efficiency degradation for a surface loss of, at least, 2.5% of the total sail base area. The most visibly affected property of the punctured sail was the restoring torque due to the area unbalance created by the hole. This has an important role on the system stability and, therefore, in case of debris collision different attitude behaviour can be expected.

Analysis of different mast lengths showed that, in general a longer, mast leads to better performance. However, the increase of system inertia associated with larger distance between satellite and sail may also cause performance degradation.

Orbital attitude simulation for a wide range of altitudes revealed that the altitude for which the sail system attains a stable oscillatory motion is mostly influenced by the solar cycle period; it was observed to be around 400-500km for minimal solar activity, and 600-700km for maximal.

The SRP force/torque has a highly destabilizing effect on the system's attitude, especially at altitude in which its magnitude is comparable to the aerodynamic one. The on/off switching action of eclipses further magnifies such effect. A transparent sail is then preferential for most cases since it minimizes the interaction with solar radiation, leading to better deorbit performances. An exception of this seems to be the deorbiting from high altitude highly inclined orbits for low solar activity. Here, the SRP action actually promotes the decay.

The study of a sail-assisted Proba-V deorbit has proven the feasibility of this system, confirming and enriching the analysis results on which the test design has been based. Full 6 DoF simulations indicate deorbit time of around 6 years for such system, with a footprint of less than 5% of the satellite dry mass. Flexibility testing for a 2-meter mast proved the occurrence of infimal deflections of the structure tip due to the relatively low load level. These tests were conducted under worst case orbital conditions. AVUM deorbiting design exercise resulted in similar performances to Proba-V, despite the considerable mass difference. The proposed configuration allows about 92% of mass saving with respect to the required for the currently adopted propelled deorbit.

As evinced, the drag-sail is a highly performing solution, capable of deorbit results in perfect compliance with the international mitigation guidelines. The outcome of this thesis represents a further demonstration of this deorbiting method potential, providing a critical overview of the related problems and constituting a departure point for future studies.

8 Future work

Given the work developed in this thesis, the possible follow-ups are various. Below, is a collection of some believed to be the most relevant.

- Despite the recognised level of accuracy of the NRLMSISE-00 atmosphere model used for this research, more recent models exist that have higher fidelity. For instance, JB-2006 and JB-2008, for considering a wider range of solar data, are highly recommended for further studies in this field [**23**].
- In order to be able to design and simulate drag deorbit systems for future missions, atmosphere model input prediction method could be used. A widely used estimation methodology that is worth investigating in this framework is the MSFC Lagrangian Linear Regression Technique (MLLRT) [**47**].
- The current tool has a limited set of implementable geometries for the satellite and deorbiting device, in many cases, inevitably leading to rough approximation of the real bodies. For this reason a wider variety of shapes and interconnections should be part of following software versions. Moreover, the presence of appendices (i.e. solar arrays) is very common; therefore, the possibility to add multiple moduli to the main body would be an important feature.
- The sail, in a first approximation, has been modelled as rigid body. However, such a thin film certainly undergoes flexible behaviours, especially for large surfaces. For this reason, a flexible membrane model should substitute the current rigid one, evaluating this effect on the attitude and deorbiting performances.
- The adopted configuration of structural components has been based on literature or specific assumptions. However, a detailed study of the design of these elements for specific missions should be performed. For instance, the mast section may need to be changed in function of the chosen sail storage approach, or a different deployment fashion could be beneficial. Furthermore, the selected boom technology has been tested for sails up to 25m^2 of area [**14**], therefore a structural analysis with wider surfaces is suggested.
- The damping properties of the studied sail systems were shown to be extremely small. This causes eventual tumbling/oscillatory motion to last for long periods of the deorbiting. The addition of alternative means of damping would certainly result in increased performances. For instance, passive magnetic dampers, which dissipate kinetic energy by magnetic hysteresis, could be considered [**15**].
- If post-EoL active attitude control is a possibility, it is worth looking into its use for sail alignment and disturbance rejection (even if only during the

initial – more unstable – stages of the deorbit trajectory). Actuators such as reaction wheels or magnetic torquers are strong candidates in such a scenario. Moreover, an optimal Solar-Aerodynamic attitude profile could be followed leading to shortest deorbit durations.

- In the analysed cases described in this document, the satellite has been assumed to start the deorbiting with a stabilized attitude. However, during the sail deployment transitory, the attitude control would, most probably, be disabled, leading to possible induction of initial rotation motion. This effect could be considered by testing a wide range of initial conditions in a Monte Carlo-like campaign.
- Satellites which rely on chemical propulsion could reach the EoL with residual propellant in the tanks. This produces sloshing effects which dynamically change the inertia proprieties of the system. This problem should be investigated extensively because it is capable to induce instability phenomena difficult to predict and control.
- Due to the difficulty of tuning of some of the study sail geometry parameters (such as mast length), extensive Monte Carlo simulation would allow a much finer selection of such properties, resulting in improved attitude behaviour and ultimately in shorter deorbit times.
- The theory behind probability of impact of debris on the sail surface has been briefly introduced in this thesis. However, this represents a fundamental problem for such and extended surface transiting through the most debris-polluted orbits. The collision probability computation could, for example, be integrated in the dynamic orbital simulation for a Monte Carlo-like campaign. This would allow an even more realistic representation and testing of the deorbiting process. In addition to the performance loss computation due to a damaged sail, the momentum variation due to the impact and its effect on the system attitude could be analysed.
- Finally, the international debris mitigation guidelines also impose limitations on the risk of human casualty. It states that, "if a space structure is to be disposed of by uncontrolled re-entry into the Earth's atmosphere, the total debris casualty area for components and structural fragments surviving re-entry will not exceed 8 m^{2}" [**47**]. This implies the need to study the collapsing and fragmentation behaviour of the deorbiting structures in low atmosphere and the possibility of different sail design to bring the system to compliance.

Bibliography

[1] United Nations, "Space Debris Mitigation Guidelines of the Committee on the Peaceful Uses of Outer Space," Office for outer space affairs, Vienna, 2010.

[2] Rex D., "The effectiveness of space debris reduction measures," *Advances in Space Research*, vol. 13, no. 8, pp. 249-262, 1993.

[3] Mehrholz D., "Detecting, Tracking and Imaging Space Debris," *ESA Bulletin*, no. 109, 2002.

[4] Alby F., "CNES operational practices for space debris risk limitation and protection," *Acta Astronautical*, vol. 40, no. 28, pp. 283-290, 1997.

[5] Mueller A.C., "The Effect of Particulates from Solid Rocket Motors," *Advances in Space Research*, vol. 5, no. 2, pp. 77-86, 1985.

[6] Adringa J., "A Systems Study on How to Dispose of Fleets of Small Satellites," Massachusetts Institute of Technology, Cambridge, Massachusetts, USA, MSc Thesis 2001.

[7] Rex D., "Will Space run out of Space? The Orbital Debris Problem and its Mitigation," *Space Policy*, vol. 14, pp. 95-105, 1998.

[8] Ruggiero A., Pergola P., and Andreucci M., "Active Removal of Space Debris: Expanding foam application for active debris removal," University of Pisa - Aerospace Engineering Department, Pisa, Italy, Final Report 2011.

[9] Bonin G., Hiemstra J., Sears T., and Zee R.E., "The CanX-7 Drag Sail Demonstration Mission: Enablign Environemntal Stewardship for Nano- and Microsatellites," in *27th Annual AIAA/USU Conference on Small Satellites*, Logan, Utah, USA, 2013.

[10] Meyer K., "Atmospheric Re-entry Disposal for Low Altitude Spacecraft," *Journal of Spacecraft and Rockets*, vol. 37, no. 5, pp. 670-674, 2000.

[11] NASA. (2014, Accessed in April) Phys.org. [Online]. http://phys.org

[12] University of Surrey. (Accessed in 2014, April) University of Surrey. [Online]. www.surrey.ac.uk

[13] Lappas V., "Gossamer Systems for Satellite Deorbiting: The Cubesail and DEORBITSAIL Missions," in *1st International Symposium on Solar Sailing*, Herrsching, Germany, 2007.

[14] Fernandez J.M., Schenk M., Prassinos G., and Erb S., "Deployment Mechanisms of a Gossamer Satellite Deorbiter," in *15th European Space Mechanisms & Tribology Symposium – ESMATS 2013*, Noordwijk, The Netherlands, 2013.

[15] Harkness P.G., "An aerostable drag-sail device for the deorbit and disposal of sub-tonne, low earth orbit spacecraft," Cranfield University, School of Engineering, Bedfordshire, Cranfield, UKPh.D. THESIS, Ph.D. Thesis 2006.

[16] NeXolve, LaRC™-CP1 Polyimide: Transparent polyimide with low moisture uptake and low dielectric constant, Datasheet.

[17] Vallado D.A., *Fundamentals of Astrodynamics and Applications*, Third Edition ed.: Microcosm Press - Springer, 2007.

[18] LAPAN. (2014, Accessed in April) Realtime Space Debris Surveillance. [Online]. http://orbit.bdg.lapan.go.id

[19] Hawkins R.A. Jr, "Analysis of an Inflatable Gossamer Device to Efficiently De-orbit Cubesats," California Polytechnic State University, San Luis Obispo, CA, USA, MSc Thesis 2013.

[20] American National Standards Institute, "Space systems — Estimation of orbit lifetime," International Standard 2010.

[21] Sidi M.J., *Spacecrafts Dynamic and Control, a Practical Engineering Approach.*: Cambridge University Press, 1997.

[22] NorthWest Research Associates. (2014, Accessed in March) NWRA. [Online]. http://www.nwra.com/

[23] ECSS Secretariat, "Space Engineering, Space Environment," ESA, European Cooperation for Space Standardization (ECSS) ECSS-E-10-04B, 2008.

[24] COSPAR, "Models of the Earth's Upper Atmosphere," COSPAR International Reference Atmosphere 2012.

[25] Wang H.B. and Zhao C.Y., "Effects of various solar indices on accuracy of Earth's thermospheric neutral density models," *Science in China*, vol. 52, no. 7, pp. 1120-1128, July 2009.

[26] CelesTrak. (2014, Accessed on February) CelesTrak. [Online]. http://celestrak.com/

[27] AGI. (2014, Accessed in March) AGI Dynamic Earth Data. [Online]. ftp://ftp.agi.com/pub/DynamicEarthData/

[28] Coomunity Coordinated Modelling Center. (2013, Accessed in December) CCMC. [Online]. http://ccmc.gsfc.nasa.gov/

[29] Gargasz M.L., "Optimal Spacecraft Attitude Control using Aerodynamics Torques," Air Force Institute of Technology, Wright-Patterson Air Force Base, Ohio, USA, MSc Thesis 2007.

[30] Moe K. and Moe M.M., "Gas–surface interactions and satellite drag coefficients," *Planetary and Space Science*, no. 53, pp. 793–801, 2005.

[31] McInnes C.R., *Solar Sailing, Technology, Dynamics and Mission Applications.*: Springer, 1999.

[32] Srivastava V.K., Pitchaimani A.M., and Chandrasekh B.S., "Eclipse prediction methods for LEO satellites with cylindrical and cone geometries: A comparative study of ECSM and ESCM to IRS satellites," *Astronomy and Computing*, vol. 2, pp. 11-17, August 2013.

[33] Wie B., *Space Vehicle Dynamics and Control*, Second Edition ed.: AIAA, 2008.

[34] Tewary A., *Atmospheric and Space Flight Dynamics.*: Birkhauser, 2007.

[35] Wiesel W.E., *Spaceflight Dynamics*, Second Edition ed.: Irwin/McGraw-Hil, 1997.

[36] Chudonvsky V., Mukheriee A., Wendlandt J., and Kennedy D., "Modeling Flexible Bodies in SimMechanics," 2006.

[37] Mitiguy P. and Banerjee A.K., "Determination of Spring Constants for Modeling Flexible Beams," 2000.

[38] Automation Creations, "Aluminum 2024-T4," Datasheet.

[39] D. J. Inman, *Engineering Vibration*, Second Edition ed.: Preatice Hall, 2001.

[40] EADS CASA Espacio, "VESPA, Vega Secondary Payload Adaptor," Presentation 2013.

[41] NASA, DAS, Debris Assessment Software, Software.

[42] Earth Observation Portal. (2014, Accessed in January) EOPortal. [Online]. https://directory.eoportal.org

[43] Sanfacon M.M., "Analysis of AlGaAs/GaAs solar cell structures by optical reflectance spectroscopy," *EEE Transactions on Electron Devices*, vol. 37, no. 2, pp. 450 - 454, 2002.

[44] The Engineering ToolBox. (2014, Accessed February 2014) The Engineering Toolbox. [Online]. http://www.engineeringtoolbox.com/

[45] Atzei A. and Lyngvy A., "Margin Philosophy for Science Assessment Studies," ESA, European Space Agency, Technical Note 1997.

[46] Astronautix. (2014, Accessed in January) Astronautix. [Online]. http://www.astronautix.com/

[47] Niehuss K.O., Euler H.C., and Vaughan W.W., "Statistical Technique for Intermediate and Long-Range Estimation of 13-Month Smoothed Solar Flux and Geomagnetic Index," NASA, Technical Memorandum 4759 1996.

[48] Gere J.M. and Timoshenko S.P., *Mechanics of Materials*, Fourth Edition ed. Boston: PWS Publishing Company, 1997.

[49] NASA, "Guidelines and Assessment Procedures for Limiting Orbital Debris," NASA Safety Standard 1995.

[50] Wertz J.R. and Larson W.J., *Space Mission Analysis and Design*, Third Edition ed.: Microcosm Press - Springer, 2010.

Appendix A Simulator Validation and Input

This Appendix presents the validation tests performed to the three developed simulation environments: 3 DoF, 6 DoF (rigid body) and 6 DoF with flexibility. A catalogue of the input information used by each simulator is also provided.

A.1 3 DoF simulator

A.1.1 Simulator validation

The 3 DoF simulator has been compared to result from STK reported on [**19**] for a complete deorbit of an object from an equatorial orbit at 800 km altitude. Unfortunately, not all the used STK settings are explicitly expressed and, for example, it has not been possible to determine what value of nominal solar radiation pressure P STK uses, or how the umbra/penumbra threshold is calculated. STK uses a Runge-Kutta 7-8 ODE solver with a 7^{th} order Lagrangian interpolation scheme, while the implemented orbit propagator uses a simple RungeKutta 4-5 scheme. The 3 DoF settings used for this validation are shown in Table A.1.

Parameter	Setting
Solver	ode45
Solar radiation pressure P	4.563 x 10-6 N/m^2
C_R	1.5
B_C	0.3764 kg/m^2
Solar activity level	Medium (F10.7=130 SFU ; AP=15)
Orbit	h=800 km, e=0, i=0°

Table A.1: 3 DoF input setting for simulator validation

The altitude deorbiting profile is reported in Figure A.1, where the red line refers to the 3 DoF simulator result, while the green one has been produced with STK [**19**]. The deorbiting time obtained with STK is of 328 days, while with the 3 DoF simulator the spacecraft deorbits in 322 days, a difference of roughly 1.9%. Given the uncertainties in how STK actually propagates the orbit in time, this result discrepancy can be considered sufficiently low to assume the 3 DoF simulator successfully validated.

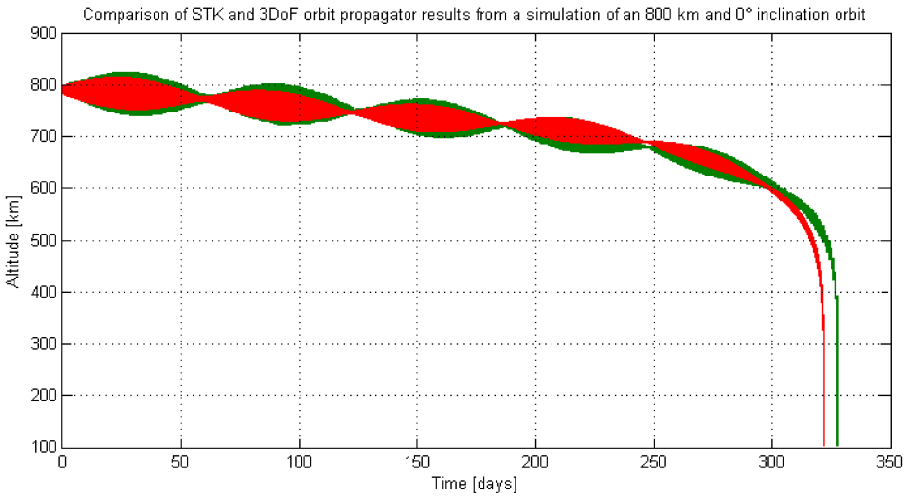

Figure A.1: Comparison between STK and 3 DoF simulator deorbiting results

A.1.2 Simulator input

For convenience of the reader, here a summary of the input of the 3 DoF simulator is presented.

Input	
Orbital parameters	Inclination
	Eccentricity
	RAAN
	Argument of perigee
	True anomaly
	Semimajor axis
Epoch	Year
	Month
	Day
	Hour
	Minute
	Seconds
Solar activity level	
Ballistic coefficient	
Optical proprieties	Coefficient of reflectivity

Table A.2: 3 DoF simulator input

A.2 6 DoF simulator

A.2.1 Simulator validation

To validate the 6 DoF model, a comparison with the altitude and forces profiles obtained studying an equivalent case with the 3 DoF simulator. The modelled system (Figure A.2) has the characteristics presented on Table A.3.

Propriety	Value
Satellite mass	100 kg
Sail mass	1.5 kg
Mast Mass	1.2 kg
Satellite dimensions (l×h×v)	1m×1m×1m
Sail shape	Cone
Sail area	50 m^2
Sail Ω	20°
Mast length	2 m
Satellite optical proprieties	Perfectly absorbent
Satellite aerodynamic proprieties	Normal accommodation
Sail optical proprieties	Perfectly reflective
Sail aerodynamic proprieties	Normal accommodation
Initial Yaw angle	60°

Table A.3: 6 DoF validation initial set of parameters

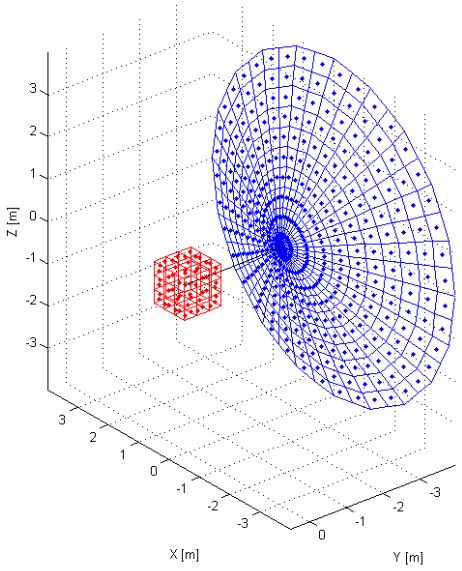

Figure A.2: Model of the spacecraft-sail configuration used.

A complete deorbiting from a 500 km circular, equatorial orbit has been simulated with the 6 DoF and the resulting average drag coefficient has been used to set the ballistic coefficient in the 3 DoF simulator. The C_D profile is reported in Figure A.3 together with the angle of attack time history.

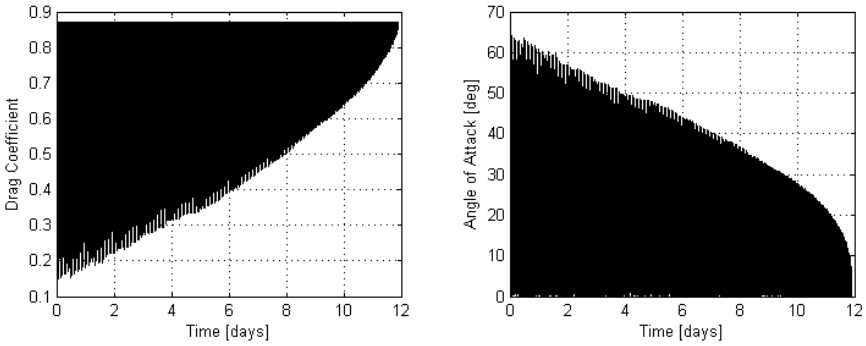

Figure A.3: 6 DoF C_D and AoA profiles with 50 m² sail during a complete deorbiting

Figure A.3 indicates an increasing stabilization of the system which results into an increment of drag coefficient with time. The computed average drag coefficient is $C_D = 0.659$.

Performing the 3 DoF simulation with the equivalent input set of parameters and observing the evolution of the altitude and forces, the following results have been obtained:

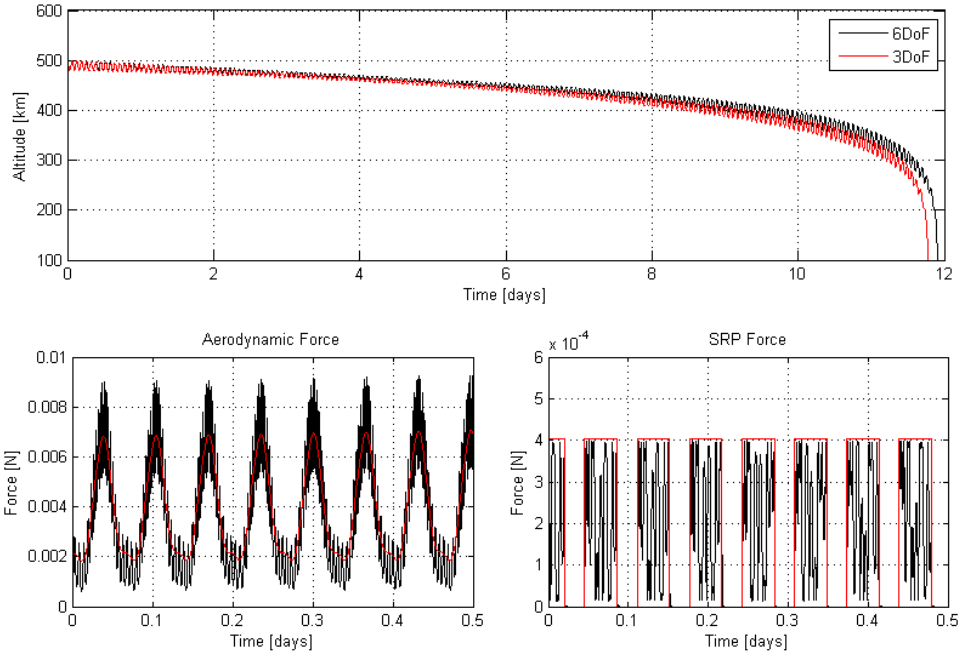

Figure A.4: 6 DoF simulator altitude and forces compared to 3 DoF simulator results

The altitude profiles for the two simulator result to match leading to a time deorbiting of 11.78 days for the 3 DoF and 11.91 days for the 6 DoF simulator, hence, the committed error is of around 1%. Also the comparison between the forces gives a good level of accuracy. Therefore, the 6 DoF simulator can be considered validated.

A.2.2 Simulator input

For convenience of the reader, here a summary of the input of the 6 DoF simulator is presented.

Input	
Orbital parameters	*Inclination*
	Eccentricity
	RAAN
	Argument of perigee
	True anomaly
	Semimajor axis
Epoch	*Year*
	Month
	Day
	Hour
	Minute
	Seconds
Solar activity level	
Satellite geometry	*Shape*
	Dimensions
	Mass
	Mast attachment point
	Number of segments
Sail geometry	*Shape*
	Dimensions
	Mass
	Number of segments
Mast geometry	*Dimensions*
	Mass
Satellite optical proprieties	τ , ϱ_s , ϱ_d , ϱ_a
Sail optical proprieties	τ , ϱ_s , ϱ_d , ϱ_a
Satellite aerodynamic proprieties	σ_n , σ_t , $\frac{v_b}{\lvert \underline{v}_\infty \rvert}$
Sail aerodynamic proprieties	σ_n , σ_t , $\frac{v_b}{\lvert \underline{v}_\infty \rvert}$
Satellite attitude respect to ECI	
Sail attitude respect to Satellite	
Mast attitude respect to Satellite	
Satellite angular velocity	
Inter-shielding function	

Table A.4: 6 DoF simulator input

A.3 6 DoF with flexibility simulator

A.3.1 Simulator validation

To validate the 6 DoF with flexibility simulator, firstly, a comparison between a modelled test case and the relative analytical solution is performed. The selected case represents the computation of the tip displacement a cantilever beam.

Assuming the beam undergoes small deflections, is in the linearly elastic region, and has a uniform cross-section, the following equations can be used

$$\frac{d^2}{dx^2}\left[EI\frac{d^2v}{dx^2}\right] = q \tag{A.1}$$

Which is known as Euler–Bernoulli equation and describes the relationship between the beam's deflection v and the applied distributed load q[**48**]. The product EI is the beam stiffness and it is assumed to be constant for this problem. Solving equation (A.1) for a cantilever beam under concentrated tip load leads to the following tip displacement expression:

$$v_{tip} = \frac{P_{tip}L^3}{3EI} \tag{A.2}$$

Where L is the beam length and P_{tip} is the load applied on the tip.

The difference between the analytical solution and the simulator result is shown in Figure A.5, where an increasing number of GBE has been considered. As expectable, the increment of elements reduces the error of the modelled solution, but it also causes an exponential computational effort increase and, consequently, longer simulations. Therefore, a trade-off between simulation time and results accuracy has to be performed.

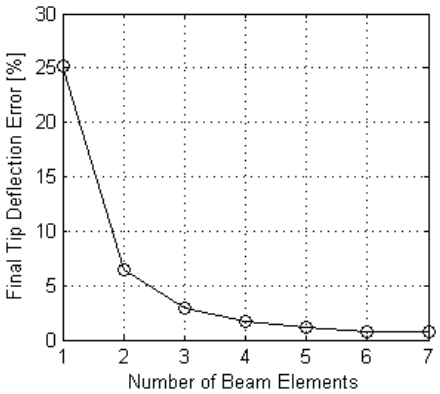

Figure A.5: Tip deflection error obtained as function of the number of masses used

As already considered for the previous cases, a comparison between the 6 DoF with and without flexibility is done in order to verify this simulator.

The modelled system has the following characteristics:

Propriety	Value
Satellite mass	100 kg
Sail mass	1.5 kg
Mast Mass	3.84 kg
Satellite dimensions (l×h×w)	1m×1m×1m
Sail shape	Cone
Sail area	50 m^2
Sail Ω	20°
Mast length	2 m
Mast section shape	Hollow square
Mast section dimensions (h×w×t)	0.06m×0.06m×0.003m
Mast Young's modulus	73.1 GPa
Satellite optical proprieties	Perfectly absorbent
Satellite aerodynamic proprieties	Normal accommodation
Sail optical proprieties	Perfectly reflective
Sail aerodynamic proprieties	Normal accommodation
Initial Yaw angle	60°

Table A.5: 6 DoF with flexibility validation initial set of parameters

The simulation is run for a circular, equatorial orbit for 1000 s, at 300 km altitude to have a highly dynamic test. The selected number of GBE is 4, which allowed a sufficiently fast simulation. The attitude angles profiles obtained with the two simulators are shown in Figure A.6 and they are perfectly superimposed, therefore no relevant difference is introduced by the flexibility in this test.

Figure A.7 (left plot) presents, instead, the transmitted force from the sail to the mast. The greater stress is along y axis but, due to the high axial stiffness of the beam, a minor elongation is produced. However, the force magnitude is very low and, in particular, along x it is comparable to the weight at sea level of a 1 g mass. The resultant tip deflection is expressed in Figure A.7 (right plot) as a percentage of the mast length. As expected, it assumes limited values, in the order of magnitude of tenth of micrometer. The flexibility problem, however, is discussed more in detail in the following chapters.

In the light of these results, the 6 DoF with flexibility simulator can be considered validated.

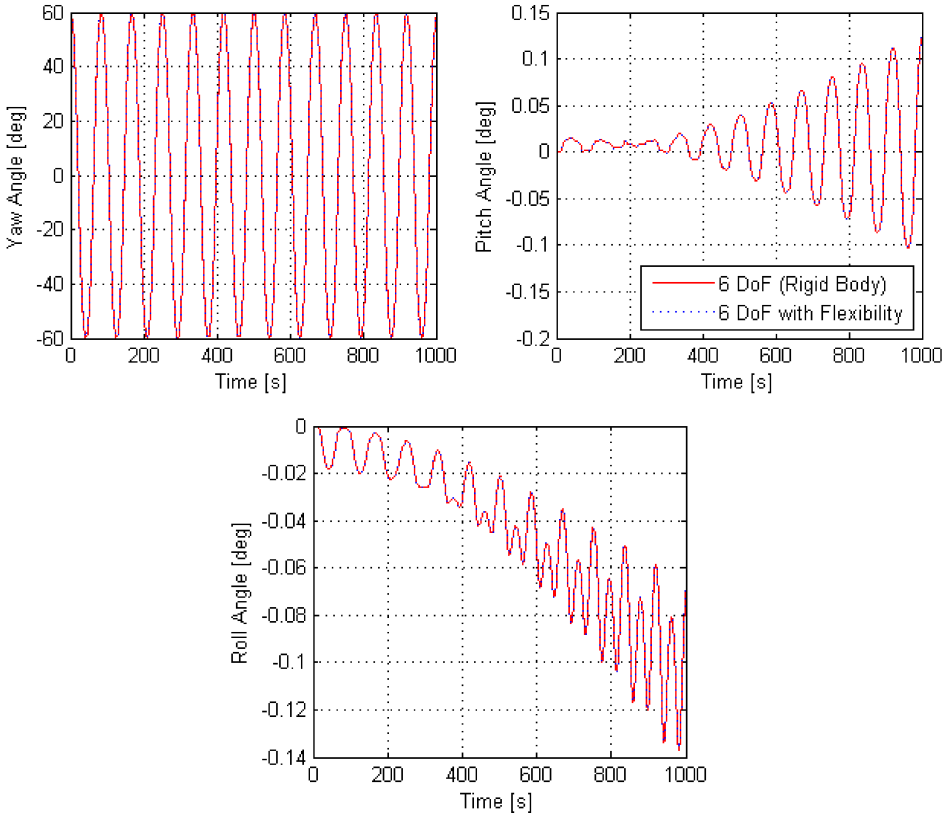

Figure A.6: Attitude angle confrontation between 6DoF simulators (with and without flexibility)

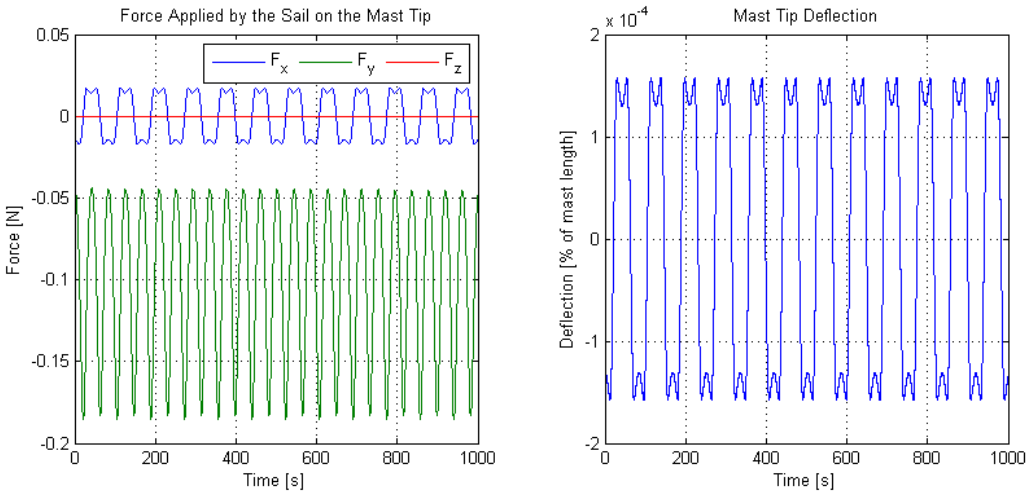

Figure A.7: Force applied on the mast tip (sail end) and mast tip deflection (flexibility simulator)

A.3.2 Simulator input

For convenience of the reader, here a summary of the input of the 6 DoF simulator is presented.

Input	
Orbital parameters	*Inclination*
	Eccentricity
	RAAN
	Argument of perigee
	True anomaly
	Semimajor axis
Epoch	*Year*
	Month
	Day
	Hour
	Minute
	Seconds
Solar activity level	
Satellite geometry	*Shape*
	Dimensions
	Mass
	Mast attachment point
	Number of segments
Sail geometry	*Shape*
	Dimensions
	Mass
	Number of segments
Mast geometry	*Dimensions*
	Mass
	GBE number
Mast material proprieties	*Young's modulus*
	Shear modulus
	Damping factor
Satellite optical proprieties	τ , ϱ_s , ϱ_d , ϱ_a
Sail optical proprieties	τ , ϱ_s , ϱ_d , ϱ_a
Satellite aerodynamic proprieties	σ_n , σ_t , $\frac{v_b}{\lvert v_\infty \rvert}$
Sail aerodynamic proprieties	σ_n , σ_t , $\frac{v_b}{\lvert v_\infty \rvert}$
Satellite attitude respect to ECI	
Sail attitude respect to Satellite	
Mast attitude respect to Satellite	
Satellite angular velocity	
Inter-shielding function	

Table A.6: 6 DoF with flexibility simulator input

Appendix B Damping and Restoring Torque Derivation

As already described in Section 3.3.3, the aerodynamic force acting on an element of area dA can be computed as

$$d\underline{F}_{aero} = \varrho \mid \underline{v}_{element} \mid^2 \; dA \cos\vartheta \left[\sigma_t \, \hat{\underline{v}}_{element} + \left(\sigma_n \left(\frac{v_b}{\mid \underline{v}_\infty \mid} \right) + \left(2 - \sigma_n - \sigma_t \right) \cos\vartheta \right) \underline{n} \right] \tag{B.1}$$

where

$$\underline{v}_{elelement} = \underline{v}_{rel} + \underline{\omega}^I \times \underline{d}_{element} \tag{B.2}$$

The translational and rotational contribution to the velocity generates two different kind of moment: the restoring torque and the damping torque. The deduction of these two contributions is here reported:

Substituting equation (B.2) in equation (B.1) it results:

$$\begin{aligned} d\underline{F}_{aero} = \varrho dA \left[\frac{\left(\underline{v}_{rel} + \underline{v}_\omega \right)}{\left| \underline{v}_{rel} + \underline{v}_\omega \right|} \cdot \underline{n} \right] \left| \underline{v}_{rel} + \underline{v}_\omega \right|^2 \Bigg\{ \sigma_t \, \frac{\left(\underline{v}_{rel} + \underline{v}_\omega \right)}{\left| \underline{v}_{rel} + \underline{v}_\omega \right|} + \sigma_n v_{b\infty} \underline{n} \\ + \left(2 - \sigma_t - \sigma_n \right) \left[\frac{\left(\underline{v}_{rel} + \underline{v}_\omega \right)}{\left| \underline{v}_{rel} + \underline{v}_\omega \right|} \cdot \underline{n} \right] \underline{n} \Bigg\} \end{aligned} \tag{B.3}$$

Where $v_\omega = \underline{\omega}^I \times \underline{d}_{element}$ and $v_{b\infty} = \dfrac{v_b}{\mid \underline{v}_\infty \mid}$

$$\begin{aligned} d\underline{F}_{aero} = \; & \varrho dA \sigma_t \left[\frac{\left(\underline{v}_{rel} + \underline{v}_\omega \right)}{\left| \underline{v}_{rel} + \underline{v}_\omega \right|} \cdot \underline{n} \right] \frac{\left(\underline{v}_{rel} + \underline{v}_\omega \right)}{\left| \underline{v}_{rel} + \underline{v}_\omega \right|} \left| \underline{v}_{rel} + \underline{v}_\omega \right|^2 \\ & + \varrho dA \sigma_n v_{b\infty} \left[\frac{\left(\underline{v}_{rel} + \underline{v}_\omega \right)}{\left| \underline{v}_{rel} + \underline{v}_\omega \right|} \cdot \underline{n} \right] \frac{\left(\underline{v}_{rel} + \underline{v}_\omega \right)}{\left| \underline{v}_{rel} + \underline{v}_\omega \right|} \left| \underline{v}_{rel} + \underline{v}_\omega \right|^2 \underline{n} \\ & + \varrho dA \left(2 - \sigma_t - \sigma_n \right) \left[\frac{\left(\underline{v}_{rel} + \underline{v}_\omega \right)}{\left| \underline{v}_{rel} + \underline{v}_\omega \right|} \cdot \underline{n} \right]^2 \left| \underline{v}_{rel} + \underline{v}_\omega \right|^2 \underline{n} \end{aligned} \tag{B.4}$$

Performing cancellations

$$\begin{aligned} d\underline{F}_{aero} = \; & \varrho dA \sigma_t \left[\left(\underline{v}_{rel} + \underline{v}_\omega \right) \cdot \underline{n} \right] \left(\underline{v}_{rel} + \underline{v}_\omega \right) \\ & + \varrho dA \sigma_n v_{b\infty} \left| \underline{v}_{rel} + \underline{v}_\omega \right| \left[\left(\underline{v}_{rel} + \underline{v}_\omega \right) \cdot \underline{n} \right] \underline{n} \\ & + \varrho dA \left(2 - \sigma_t - \sigma_n \right) \left[\left(\underline{v}_{rel} + \underline{v}_\omega \right) \cdot \underline{n} \right]^2 \underline{n} \end{aligned} \tag{B.5}$$

And approximations for each term

$$\begin{aligned}\left[\left(\underline{v}_{rel}+\underline{v}_{\omega}\right)\cdot\underline{n}\right]\left(\underline{v}_{rel}+\underline{v}_{\omega}\right) = &\left(\underline{v}_{rel}\cdot\underline{n}\right)\underline{v}_{rel}+\left(\underline{v}_{\omega}\cdot\underline{n}\right)\underline{v}_{rel}+\left(\underline{v}_{rel}\cdot\underline{n}\right)\underline{v}_{\omega}+\left(\underline{v}_{\omega}\cdot\underline{n}\right)\underline{v}_{\omega}\\ \approx &\left(\underline{v}_{rel}\cdot\underline{n}\right)\underline{v}_{rel}+\left(\underline{v}_{\omega}\cdot\underline{n}\right)\underline{v}_{rel}+\left(\underline{v}_{rel}\cdot\underline{n}\right)\underline{v}_{\omega}\end{aligned} \tag{B.6}$$

$$\left|\underline{v}_{rel}+\underline{v}_{\omega}\right|\left[\left(\underline{v}_{rel}+\underline{v}_{\omega}\right)\cdot\underline{n}\right]\underline{n}\approx\left|\underline{v}_{rel}\right|\left[\left(\underline{v}_{rel}+\underline{v}_{\omega}\right)\cdot\underline{n}\right]\underline{n}=\left|\underline{v}_{rel}\right|\left(\underline{v}_{rel}\cdot\underline{n}\right)\underline{n}+\left|\underline{v}_{rel}\right|\left(\underline{v}_{\omega}\cdot\underline{n}\right)\underline{n} \tag{B.7}$$

$$\begin{aligned}\left[\left(\underline{v}_{rel}+\underline{v}_{\omega}\right)\cdot\underline{n}\right]^2\underline{n} = &\left[\left(\underline{v}_{rel}\cdot\underline{n}\right)^2+2\left(\underline{v}_{rel}\cdot\underline{n}\right)\left(\underline{v}_{\omega}\cdot\underline{n}\right)+\left(\underline{v}_{\omega}\cdot\underline{n}\right)^2\right]\underline{n}\\ \approx &\left(\underline{v}_{rel}\cdot\underline{n}\right)^2+2\left(\underline{v}_{rel}\cdot\underline{n}\right)\left(\underline{v}_{\omega}\cdot\underline{n}\right)\underline{n}\end{aligned} \tag{B.8}$$

which yields

$$\begin{aligned}d\underline{F}_{aero}\approx\ &\varrho dA\sigma_t\left(\underline{v}_{rel}\cdot\underline{n}\right)\underline{v}_{rel}+\varrho dA\sigma_t\left[\left(\underline{v}_{\omega}\cdot\underline{n}\right)\underline{v}_{rel}+\left(\underline{v}_{rel}\cdot\underline{n}\right)\underline{v}_{\omega}\right]\\ &+\varrho dA\sigma_n v_{b\infty}\left|\underline{v}_{rel}\right|\left(\underline{v}_{rel}\cdot\underline{n}\right)\underline{n}+\varrho dA\sigma_n v_{br}\left|\underline{v}_{rel}\right|\left(\underline{v}_{\omega}\cdot\underline{n}\right)\underline{n}\\ &+\varrho dA\left(2-\sigma_t-\sigma_n\right)\left(\underline{v}_{rel}\cdot\underline{n}\right)^2\underline{n}+\varrho dA\left(2-\sigma_t-\sigma_n\right)2\left(\underline{v}_{rel}\cdot\underline{n}\right)\left(\underline{v}_{\omega}\cdot\underline{n}\right)\underline{n}\end{aligned} \tag{B.9}$$

The red components depend only on $\underline{v}_{rel}$ and the green ones depends also on $\underline{v}_{\omega}$.

The moment contribution of each surface element is given by

$$d\underline{T}_{aero}=d\underline{F}_{aero}\times\underline{r}_{element} \tag{B.10}$$

Hence, the restoring torque will arise from the force terms in red, and the damping torque from the green terms.

$$\begin{aligned}d\underline{T}_{rest}\approx\ &r_{element}\times\left[\varrho dA\sigma_t\left(\underline{v}_{rel}\cdot\underline{n}\right)\underline{v}_{rel}+\varrho dA\sigma_n v_{b\infty}\left|\underline{v}_{rel}\right|\left(\underline{v}_{rel}\cdot\underline{n}\right)\underline{n}\right.\\ &\left.+\varrho dA\left(2-\sigma_t-\sigma_n\right)\left(\underline{v}_{rel}\cdot\underline{n}\right)^2\underline{n}\right]\end{aligned} \tag{B.11}$$

$$\begin{aligned}d\underline{T}_{damp}\approx\ &r_{element}\times\left[\varrho dA\sigma_t\left[\left(\underline{v}_{\omega}\cdot\underline{n}\right)\underline{v}_{rel}+\left(\underline{v}_{rel}\cdot\underline{n}\right)\underline{v}_{\omega}\right]+\varrho dA\sigma_n v_{b\infty}\left|\underline{v}_{rel}\right|\left(\underline{v}_{\omega}\cdot\underline{n}\right)\underline{n}\right.\\ &\left.+\varrho dA\left(2-\sigma_t-\sigma_n\right)2\left(\underline{v}_{rel}\cdot\underline{n}\right)\left(\underline{v}_{\omega}\cdot\underline{n}\right)\underline{n}\right]\end{aligned} \tag{B.12}$$

The total restoring and damping torques are

$$\underline{T}_{rest}=\int_A d\underline{T}_{rest} \tag{B.13}$$

$$\underline{T}_{damp}=\int_A d\underline{T}_{damp} \tag{B.14}$$

Appendix C Debris Impact Probability

The impact with large debris can severely injure the sail device. The probability P of a space system being hit by objects of this size passing through LEO, can be approximated by

$$P = 1 - e^{-FAT} \tag{C.1}$$

where

- F is the cross-sectional area flux for the orbital debris environment, taken from Figure C.1;
- A is the average cross-sectional area for the space system in m^2;
- T is the mission duration or deorbiting time in years.

The orbital debris flux is taken to be 0 for altitudes above 2000 km. The flux for meteoroids 10 cm in diameter or larger is negligible and can be ignored [**49**].

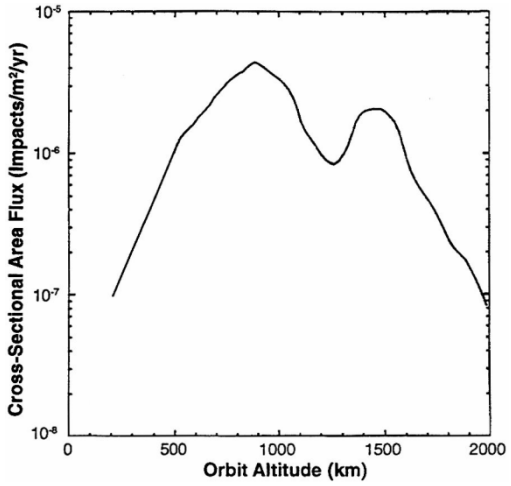

Figure C.1: Cross-sectional area flux of intact space systems and large orbital debris

For the particular case of small drag-sails the impact with debris or meteoroids smaller than 1 cm needs to be taken into account. This analysis should also be contemplated in the scenario of extended rips due to small particle impact, caused by a weak energy absorption skill of the sail material. The procedure to compute the collision probability is here summarized, for a detailed explanation refers to [**49**].

1. Identify the *critical surface,* the area of the components that, when damaged by impact, causes the component to fail;
2. Calculate the at-risk surface area A_i for the critical surface of each critical component;

3. For each at-risk surface element, identify vehicle components and structural material that helps protect that surface;
4. Estimate, for each at-risk surface element, the minimum meteoroid or orbital debris diameter that can cause damage;
5. Determine the expected number of failures h_i for each critical element; It depends from the cross-sectional area flux F, taken from Figure C.2 for the needed altitude and the debris size determined in Step 4; it is also dependant on A_i, the mission duration and a correction factor base on the space-system attitude;
6. Calculate the expected number of failures F_C summing the expected number of failures for each element h_i, as determined in Step 5;
7. Compute the probability of failure P_C of one or more critical elements as [**49**].

$$P_C = 1 - e^{-F_c} \tag{C.2}$$

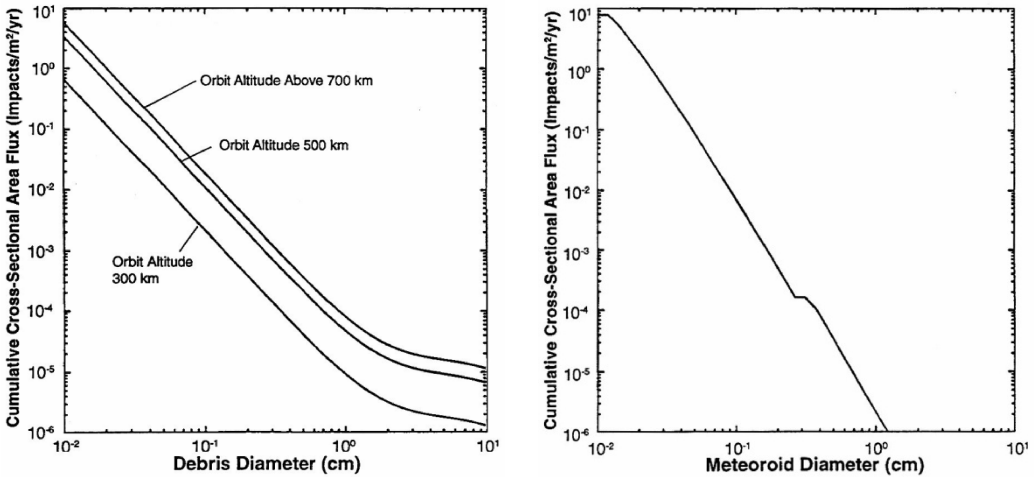

Figure C.2: Cross-sectional area flux from orbital debris (left) and meteoroid (right) as a function of debris diameter for spacecraft in LEO [49**]**

Appendix D Two-Line Elements

A Two-Line elements (TLE) set is a data format commonly used to convey the orbits of Earth-orbiting satellites [**26**]. A TLE consists of two 69-character lines of data which can be used to determine the position and velocity of the associated satellite. It follows an example for a better understanding of this set.

```
PROBA-I
1 26958U 01049B   09330.79739372  .00000355  00000-0  40630-4 0  1998
2 26958 097.6021 027.4760 0081390 187.4704 172.5311 14.89712188440035
```

Title line

Field	Columns	Description	Example
1	01-24	Satellite name	PROBA-I

First line

Field	Columns	Description	Example
1	01	Line Number of Element Data	1
2	03-07	Satellite Number	26958
3	08	Classification	U
4	10-11	International Designator (Last two digits of launch year)	01
5	12-14	International Designator (Launch number of the year)	049
6	15-17	International Designator (Piece of the launch)	B
7	19-20	Epoch Year (Last two digits of year)	09
8	21-32	Epoch (Day of the year and fractional portion of the day)	330.79739372
9	34-43	First Time Derivative of the Mean Motion	.00000355
10	45-52	Second Time Derivative of Mean Motion (decimal point assumed)	00000-0

11	54-61	BSTAR drag term (decimal point assumed)	40630-4
12	63	Ephemeris type	0
13	65-68	Element number	199
14	69	Checksum	8

Second line

Field	**Column**	**Description**	**Example**
1	01	Line Number of Element Data	2
2	03-07	Satellite Number	26958
3	09-16	Inclination [Deg]	097.6021
4	18-25	Right Ascension of the Ascending Node [Deg]	027.4760
5	27-33	Eccentricity (decimal point assumed)	0081390
6	35-42	Argument of Perigee [Deg]	187.4704
7	44-51	Mean Anomaly [Deg]	172.5311
8	53-63	Mean Motion [Revs per day]	14. 89712188
9	64-68	Revolution number at epoch [Revs]	44003
10	69	Checksum (Modulo 10)	5